Vision-based control of unmanned aerial vehicles

Zhiqi Tang

Zhiqi Tang. Vision-based control of unmanned aerial vehicles. Signal and Image processing. Université Côte d'Azur; Instituto superior técnico (Lisbonne), 2021. English. NNT : 2021COAZ4018 . tel-03324830

HAL Id: tel-03324830
https://theses.hal.science/tel-03324830v1

Submitted on 24 Aug 2021

UNIVERSITÉ CÔTE D'AZUR

ÉCOLE DOCTORALE
SCIENCES ET TECHNOLOGIES DE L'INFORMATION ET DE LA COMMUNICATION

TÉCNICO LISBOA

THÈSE DE DOCTORAT

Commande référencée vision de drones aériens

Zhiqi Tang
I3S-CNRS

Présentée en vue de l'obtention
du grade de docteur en Automatique
Traitement du signal et des images
d'Université Côte d'Azur
et de University of Lisbon
Dirigée par : Prof. Tarek Hamel (/ Prof. Carlos Silvestre)
Co-encadrée par : Prof. Rita Cunha
Soutenue le : 30/03/2021

Devant le jury, composé de :
Rapporteur :
Abdelhamid Tayebi, Professor, Lakehead University
Antonio Pedro Aguiar, Associate Professor, University of Porto
Directeur de cette thèse :
Tarek Hamel, Professor, I3S-CNRS, Université Côte d'Azur
Examinateur
Elena Panteley, Directeur de Recherche CNRS, L2S, CentraleSupélec
Joao Pedro Gomes, Associate Professor, Institute Superior Técnico

UNIVERSIDADE DE LISBOA
INSTITUTO SUPERIOR TÉCNICO
UNIVERSITÉ CÔTE D’AZUR

Vision-based Control of Unmanned Aerial Vehicles

Zhiqi Tang

Supervisors: Doctor Carlos Jorge Ferreira Silvestre
Doctor Tarek Hamel
Co-Supervisor: Doctor Rita Maria Mendes de Almeida Correia da Cunha

Thesis approved in public session to obtain the PhD Degree in Electrical and Computer Engineering

Jury final classification: Pass with Distinction and Honour

2021

UNIVERSIDADE DE LISBOA
INSTITUTO SUPERIOR TÉCNICO
UNIVERSITÉ CÔTE D'AZUR

Vision-based Control of Unmanned Aerial Vehicles

Zhiqi Tang

Supervisors: Doctor Carlos Jorge Ferreira Silvestre
Doctor Tarek Hamel
Co-Supervisor: Doctor Rita Maria Mendes de Almeida Correia da Cunha

Thesis approved in public session to obtain the PhD Degree in Electrical and Computer Engineering

Jury final classification: Pass with Distinction and Honour

Jury

Chairperson: Doctor João Manuel Lage de Miranda Lemos
Instituto Superior Técnico, Universidade de Lisboa
Members of the committee:
Doctor Abdelhamid Tayebi
Lakehead University, Canada
Doctor Tarek Hamel
I3S-CNRS, Université Côte d'Azur, France
Doctor Elena Panteley
Laboratoire des Signaux et Systèms L2S, CentraleSupélec, France
Doctor António Pedro Rodrigues Aguiar
Faculdade de Engenharia da Universidade do Porto
Doctor João Pedro Castilho Pereira Santos Gomes
Instituto Superior Técnico, Universidade de Lisboa

Funding Institution:
Fundação para a Ciência e a Tecnologia

2021

"Suffering becomes beautiful when anyone bears great calamities with cheerfulness,
not through insensibility but through greatness of mind."
– Aristotle.

ABSTRACT

This thesis proposes novel vision-based controllers for the guidance of Unmanned Aerial Vehicles (UAVs). It considers scenarios involving both single and multiple vehicles. For the case of a single-vehicle, novel Image-based visual servo control (IBVS) approaches are proposed for both fixed-wing and vertical take-off and landing (VTOL) UAVs operating in urban or congested environments. Navigation tasks in a complex environment with obstacle avoidance capabilities are considered. In particular, the landing of fixed-wing UAVs on an airstrip and the landing of VTOL-UAVs that includes an obstacle avoidance strategy are considered. The originality of the study lies in the direct exploitation of the centroid of the image of the observed pattern together with the optical flow, thereby eliminating the need to estimate the position and the velocity of the UAV. For multiple vehicles, novel bearing formation controllers are designed for formations under both directed and undirected interaction topologies. In order to relax the classical conditions required by bearing rigidity theory and to lift the scale ambiguity caused by bearings, persistence of excitation of the desired bearing reference is explored. The proposed methodology is supported by rigorous mathematical tools (This involves nonlinear dynamical systems and analysis using Lyapunov theory to formally prove the asymptotic (or exponential) stability of the system, guarantee robustness, and finally ensure good performance of the closed-loop system). Further support is provided by real experiments and/or simulation results.

Keywords: Unmanned Aerial vehicles (UAVs); Visual servo control; Nonlinear Systems; formation control; Lyapunov method.

ABSTRACT IN PORTUGUESE

Esta tese propõe um conjunto de novos controladores baseados em visão para a condução de veículos autónomos aéreos (VAAs), considerando cenários que envolvem um ou vários veículos. Para o caso da condução de um veículo único são propostas novas abordagens de servo controlo visual baseado em imagem para VAAs de asa fixa e de descolagem e aterragem vertical (VDAV) operando em ambientes urbanos ou congestionados. São consideradas tarefas de navegação em ambientes complexos que incluem a capacidade de evitar obstáculos. Estas são, em particular, a aterragem de VAAs do tipo asa fixa numa pista de aterragem e a aterragem de VAAs do tipo VDAV com incorporação de uma estratégia de evitar obstáculos. A originalidade do estudo está na exploração direta do centróide da imagem do padrão observado e do fluxo óptico, eliminando assim a necessidade da estimação explícita da posição e da velocidade do VAA. Para o caso do controlo de formações de múltiplos veículos, são propostos novos controladores baseados nas medidas da direção entre os agentes para topologias dos grafos de interação direcionadas e não direcionadas. A fim de relaxar as condições clássicas exigidas pela teoria da rigidez do grafo de interação da formação e para levantar a ambiguidade de escala introduzida pelo uso das direções, é explorada a persistência de excitação da referência de direção desejada. A metodologia proposta é suportada em ferramentas matemáticas rigorosas (envolvendo sistemas dinâmicos não lineares e analisadas com recurso à teoria de Lyapunov para provar formalmente a estabilidade assintótica (ou exponencial) do sistema resultante, de forma a obter a robustez e o desempenho do sistema em malha fechada) e por experiências reais e / ou resultados de simulação.

Palavras Chave: Veículos aéreos autónomos; Controlo baseado em visão; Sistemas não lineares; Controlo de formações; Técnicas de Lyapunov.

ABSTRACT IN FRENCH

Cette thèse propose de nouvelles commandes basées sur un retour visuel pour le guidage de drones. Elle considère à la fois des scénarios impliquant un seul ou plusieurs véhicules. Pour le cas du guidage d'un seul véhicule, de nouvelles approches d'asservissement visuel basées image (IBVS) sont proposées pour les drones de type avion (fixed-wing) et les drones de type VTOL (Vertical Take-Off and Landing) opérant en environnements urbains ou encombrés. Des tâches de navigation dans un environnement complexe avec des capacités d'évitement d'obstacle sont considérées. Il s'agit en particulier de l'atterrissage de drones de type fixed-wing sur une piste d'atterrissage et l'atterrissage de drones de type VTOL-UAV en incluant une stratégie d'évitement d'obstacle. L'originalité de l'étude réside dans l'exploitation directe de la centroïde de l'image du motif observé et du flux optique permettant ainsi d'éliminer la nécessité l'estimation de la position et la vitesse du drone. Pour le cas du contrôle de plusieurs véhicules en formation, de nouveaux contrôleurs à base de la mesure de direction entre véhicules sont également proposés pour des formations ayant une interaction topologique orientées ou non orientées. Afin d'assouplir les conditions classiques requises par la théorie de la rigidité d'une formation à partir de l'information de direction et lever par la même occasion l'ambiguïté du facteur d'échelle causée par les mesures de directions, la notion de la persistance de l'excitation associée à la formation de référence est explorée. La méthodologie proposée est soutenue par des outils mathématiques rigoureux (impliquant des systèmes dynamiques non linéaires et analysés à l'aide de la théorie de Lyapunov afin de prouver formellement la stabilité asymptotique (ou exponentielle) du système, de garantir la robustesse et enfin d'assurer le bon fonctionnement du système en boucle fermée) et par des expériences réelles et/ou des résultats de simulation.

Mots clés: Drones; Robots aériens; Asservissement visuel; Système non linéaire; Contrôle multi-agents; Analyse de Lyapunov.

To my family.

ACKNOWLEDGMENTS

I would like to thank my advisors, Professor Carlos Silvestre, Professor Tarek Hamel and Professor Rita Cunha for their help, support and guidance for my research work during the past few years. I would like also to thank David Cabecinhas and Joel Reis for their help during the experiment, and Hang Yin for his comments about the thesis.

This work was supported by Fundação para a Ciência e a Tecnologia (FCT) through Ph.D. Fellowship PD/BD/114431/2016 under the FCT-IST NetSys Doctoral Program; by the Macao Science and Technology Development Fund under Grant FDCT/0031/2020/AFJ, by the University of Macau, Macao, China, under Project MYRG2018-00198-FST, by the FCT through LARSyS - FCT Project UIDB/50009/2020 and PTDC/EEIAUT/31411/2017, by FCT Scientific Employment Stimulus grant CEECIND/04199/2017 and by FCT projects REPLACE (PTDC/EEI-AUT/32107/2017) and CAPTURE (PTDC/EEI-AUT/1732/2020).

CONTENTS

LIST OF FIGURES

1

INTRODUCTION

1.1 Literature Review and Motivation

The development of Unmanned Aerial Vehicles (UAVs) is an increasingly important area of both robotics and control research due to a large range of applications in both civilian and military scenarios. UAVs have strong commercial potential in remote surveillance applications such as monitoring traffic congestion, regular inspection of infrastructure (such as bridges and power cables), investigation of hazardous and remote environments, etc. High-performance autonomous navigations capabilities are of paramount importance to proficiently perform these missions. Navigation of UAVs can be roughly described as the process of determining a suitable and safe path between a starting and a goal point for a vehicle traveling between them. A complete navigation framework includes mapping, localization, and also control. Traditional navigation methods include satellite navigation, inertial navigation, radar navigation, sonar navigation, etc. However, Global Navigation Satellite System (GNSS) does not work effectively indoors and in urban canyon environments and Inertial Navigation system (INS) suffers from loss of accuracy to some extent due to the propagation of bias error caused by the integral drift problem. Nowadays, reduced-size UAVs are very common but are limited in their payload capabilities, thus, they are not able to carry lasers or certain brands of sonars. With the rapid development of the field of computer vision, vision-based navigation becomes a promising research direction. Visual sensors are able to acquire rich visual information from the surrounding environment, which provides position and velocity cues of the vehicle relative to the target. As inertial measurement units (IMUs) are getting smaller and cheaper, a common sensor suite for vision-based navigation includes an IMU consisting of accelerometers and rate gyros along with a camera, which is passive, lightweight, and efficient.

Vision-based Navigation systems can be roughly divided in two categories: i) previous knowledge of the whole environment is required, and ii) the environment is only perceived as the vehicles navigate through it [BFOO08]. Three main solutions have been proposed for navigation using vision in indoor environments: map-based navigation, map-building-based navigation and map-less navigation[DK02]. The first approach depends on a user-created geometrical model or topology map of the environment (e.g. Perspective-n-Point (PnP)) and the second requires the use of sensors to construct their own geometric or topological models (e.g. simultaneous localization and mapping (SLAM)). Map-less navigation systems mostly include reactive techniques that rely on visual clues derived from the optical flow and distinctive features in the environment. In these systems, the environment is perceived as the system navigates, recognizes objects or tracks landmarks, thus no global representation of the environment exists.

The main vision techniques or types of clues used during the map-less visual navigation process are optical flow, appearance-based matching and feature tracking [DK02]. Appearance-based matching techniques rely on the storage of images in a previous recording phase which are then used as templates, e.g.[BGC16]. The robot self-locates and navigates in the environment by matching the current viewed frame with the stored templates. The main problems with this method consist in finding an appropriate algorithm for the representation of the environment and defining the on-line matching criteria [DK02]. Other approaches use optical flow as a velocity cue, e.g. [MCH08, HHMR12, LBHM+14]. Optical flow, a visual feature inspired from flying insects, is the pattern of apparent motion of objects, surfaces, and edges in a visual scene caused by the relative motion between an observer and a scene[BR78]. It has been experimentally shown that the neural system of the insects reacts to optic flow patterns to produce a large variety of flight capabilities, such as obstacle avoidance, speed maintenance, odometry estimation, wall following and corridor centering, altitude regulation, orientation control and landing [FW15]. Finally, in the category of navigation using feature tracking, the motion of moving elements, including lines, corners, or specific regions in a video sequence are tracked. The trajectory and motion of the robot is determined by tracking and finding relative changes in the position of extracted features.

Visual servo control is an important concept which can be included in the category of map-less navigation techniques based on feature tracking. It refers to the use of visual features to control the motion of a robot. The visual features may be acquired from a camera that is mounted directly on a robot manipulator or on a mobile robot, in which the motion of the robot induces the camera motion, or the camera can be fixed in the workspace so that it can observe the robot motion from a stationary configuration [CHC16]. There are two main approaches for visual servoing systems: pose-based visual servoing (PBVS) and image-based visual servoing (IBVS). PBVS involves reconstruction of the target pose with respect to the robot and leads to a Cartesian motion planning problem, thus the camera intrinsic parameters and 3-D model of the observed object should be known. In IBVS, the control commands are deduced directly from image features. IBVS methods offer advantages in robustness to camera and target calibration errors, a reduced computational complexity, and simple extension to applications involving multiple cameras compared to PBVS methods[HHC96].

However, classical IBVS suffers from three key problems. Firstly, it is necessary to determine the depth of each visual feature used in the image error criterion independently from the control algorithm. Secondly, the rigid-body dynamics of the camera ego-motion are highly coupled when expressed as target motion in the image plane. Thirdly, classical IBVS control design uses a simple linearized control on the image kinematics that leads to complex non-linear dynamical model and is not easily extended to include the dynamics. In order to overcome these problems, the authors in [HM02] propose a novel IBVS algorithm for a class of under-actuated dynamic systems, which relies on passivity-like properties that can be recovered for a centroid image feature as long as a spherical camera geometry is used. The virtual spherical image points can be obtained by transforming the image points on the perspective camera to the view that would be seen by an ideal unified-spherical camera. The proposed algorithm does not require accurate depth information for observed image features and overcomes some of the difficulties associated with the highly couple dynamics of the camera ego-motion in the image dynamics.

In the early development stages of IBVS methods, the translational velocity of the vehicle normally needs to be measured or to be estimated, e.g. [CHC16], [HM02]. Using optical flow as velocity cue and observed feature expressed in terms of an unnormalized spherical centroid, a fully nonlinear adaptive visual servo control design is provided in [MCH08]. Although the height of the camera above the target plane still needs to be estimated and used as a parameter, it is the first time that an IBVS control has been proposed for a dynamics system using vision measurement for both position and velocity. Inspired by [MCH08] and [HHMR12], the work in [SCH$^+$16] proposes an IBVS controller for the landing maneuver of a VTOL vehicle using a new centroid for position-like feedback and translational optical flow, computed from the camera images, for velocity-like feedback. Neither the height above the target nor the relative velocity of the vehicle to the target need to be measured or estimated.

In summary, IBVS methods based on spherical camera geometry together with optical flow are highly preferred due to the following advantages:

i) neither the depth of image features nor the translational velocity vector need to be estimated,

ii) the decoupling problem can be solved thanks to the invariance properties of spherical point model with respect to rotational motion,

iii) simple controllers can be designed for dynamic system models.

The works mentioned above are mainly focused on vision-based navigation for a single UAV. For multiple UAVs, using this inexpensive sensor suite, which includes an IMU and a camera, is also a popular choice. In considering the problem of formation control in the deployment of UAVs, it is highly desirable to limit the transmitted information between the vehicles in the formation, both from mission and cost perspectives. The main categories of solutions of formation control can be classified as follows ([OPA15]): *i)* position-based formation control, [RA07], *ii)* displacement-based formation control, [RBM05], *iii)* distance-based formation control, [ADY07], and more recently, *iv)* bearing-based formation control, [BBJ10]. As mentioned above, cameras can provide accurate direction (bearing) information, but the estimation of distances from cameras is typically noisier and is not possible without a known structure in the environment. Thus, bearing formation control has received growing attention in both the robotics and the control communities due to its minimal requirements on the sensing ability of each agent.

Early works on bearing-based formation control were mainly focused on controlling the subtended bearing angles that are measured in each agent's local coordinate frame, but were limited to the planar formations only [BBJ10, Bis11]. The main body of work, however, builds on concepts of bearing rigidity theory, which investigates the conditions for which a static formation is uniquely determined up to a translation and a scaling given the corresponding constant bearing measurements. Bearing rigidity theory in two-dimensional space (also termed parallel rigidity) is explored in [EWM+03, SW99]. More recently, bearing rigidity theory has been extended to arbitrary dimensions with a bearing-only formation control solution proposed in [ZZ16]. Under the assumption that the desired formation is infinitesimally bearing rigid, the resulting bearing controller guarantees convergence to the target formation up to a scaling factor and a translation vector. Minimal rigidity, which determines whether or not the connections in a graph are minimal in the sense that removing any of these connections will result in loosing rigidity, has been extensively studied in distance rigidity theory [TW85, AYFH08] and also explored in bearing rigidity theory. For an n-agent system, a minimally bearing rigid formation in two dimensional space has $2n-3$ links [EWM+03] and the condition for minimally bearing rigid formations in higher dimensional space is explored in [TVTA19].

In the more challenging context of directed graphs, achieving stabilization of a formation requires not only bearing rigidity, as in the case of undirected graphs, but also constraint consistence, which is the ability to maintain consistence between constraints induced by the desired bearing measurements (termed bearing persistence, in [ZZ15a]). In [Ere12], the conditions for directed bearing rigidity of a digraph in two-dimensional space are stated and a bearing control law for nonholomonic agents is proposed. In [TZS+19], bearing control laws have been proposed that asymptotically stabilize leader-first follower (LFF) formations in arbitrary dimensional space to the desired formations up to a translation (the leader's position) and a scaling factor . Since the bearing rigidity of a static formation is invariant to scaling, the measurement of at least one distance between two agents is required to guarantee the convergence of formations in terms of shape and scale. For instance, [SFZG16] proposes a controller based on bearing rigidity of directed bearing frameworks defined in $\mathbb{R}^3 \times \mathcal{S}^1$ complemented with the measurement of at least one distance between two agents.

Overall, the main body of work on bearing-based formation control, however, only considers static bearings and relies heavily on complex constraints on graph topology, such as bearing rigidity and constraint consistence. It is worth taking time-varying bearing formation into consideration and explore the possibilities of relaxing the bearing rigidity theory in a natural manner.

1.2 Contributions of the Thesis

In this thesis, novel vision-based controllers are designed for the 3-D motion control of both single and multiple vehicles, specifically targeting UAV applications.

For the case of a single vehicle, novel IBVS approaches are proposed for both fixed-wing and vertical take-off and landing (VTOL) UAVs operating especially in urban or congested environments. The originality of the study lies in the direct exploitation of the centroid of the spherical image points of the observed pattern together with the optical flow thereby preventing the need to estimate the position and the velocity of the UAV. For a fixed-wing UAV, a 2D image-based controller is proposed to automatically land the vehicle on an airstrip. The main innovations compared to the previous work [LBHM$^+$14] result in a controller that: i) uses optical flow measurement instead of airspeed measurements for the derivative term, ii) relies on writing the kinematics in terms of the 3D position error instead of the visual error and thus enables an alternative proof of stability and has the advantage of imposing less restrictive conditions on the tunable gains. For the VTOL UAV, we extend the IBVS control solution based on spherical image centroids to a specific problem of steering a vehicle to move from one room to a second one by crossing a window and then land on a planar target placed in the second room. The control law proposed for going through the window is new and for landing is an improvement with respect to [SCH$^+$16], with the centroid vector now directly given by the image centroid, which is highly robust to pixel noise, and easily computed in real-time in the camera frame.

For multiple vehicles, novel bearing formation controllers are designed for formations under both directed and undirected interaction topologies. In order to relax the classical conditions required by bearing rigidity theory and to lift the scale ambiguity caused by bearings, the persistence of excitation (PE) condition of the desired bearing reference is explored. The concept of PE is a well-known concept in adaptive control and identification of linear systems. Firstly, novel bearing control laws are proposed for leader-follower formations, which achieve exponential stabilization of the leader-follower formation in terms of shape and scale as long as the desired formation is bearing PE, thereby relaxing the bearing rigidity requirement.

A coherent generalization to formations under general undirected graph topologies is also provided.

The proposed methodologies are supported by rigorous mathematical tools (involving nonlinear dynamical systems and analysis using Lyapunov theory to formally prove the asymptotic (or exponential) stability of the system, to guarantee the robustness and finally to ensure good performance of the closed-loop system) and by real experiments and/or simulation results. The following subsections summarize the individual contributions of each chapter.

1.2.1 Aircraft landing using dynamic 2D image-based guidance control [TCHS18a]

In Chapter 2, a novel 2D image-based controller is proposed, which automatically steers a fixed-wing Unmanned Aerial Vehicle (UAV) during the first three stages of landing: alignment, glide-slope, and flare. Observable image features of the runway and its textured ground are exploited to derive a feedback controller for the automatic maneuver. The proposed controller ensures the horizontal position alignment and a smooth touchdown of the aircraft without estimating the height above the runway. In addition, the 2D image-based control structure adopted also enforces wind disturbance rejection, without the need for an explicit wind estimator. Simulation results are presented to illustrate the performance of the controller.

1.2.2 Quadrotor going through a window and landing: An image-based visual servo control approach [TCHS18b, TCC+20]

Chapter 3 considers the problem of controlling a quadrotor to go through a window and land on a planar target, the landing pad, using an IBVS controller that relies on sensing information from two on-board cameras and an IMU. The maneuver is divided into two stages: crossing the window and landing on the pad. For the first stage, a control law is proposed that guarantees that the vehicle will not collide with the wall containing the window and will go through the window with non-zero velocity along the direction orthogonal to the window, keeping at all times a safety distance with respect to the window edges. For the landing stage, the proposed control law ensures that the vehicle achieves a smooth touchdown, keeping at all time a positive height above the plane containing the landing pad. For control purposes, the centroid vectors provided by the combination of the spherical image measurements of a collection of landmarks (corners) for both the window and the landing pad are used as position measurement. The translational optical flow relative to the wall, window edges, and landing plane is used as velocity cue. To achieve the proposed objective, no direct measurements nor explicit estimate of position or velocity are required. Simulation and experimental results are provided to illustrate the performance of the presented controller.

1.2.3 Bearing leader-follower formation control under persistence of excitation [TCHS20a, TCHS20c]

Chapter 4 solves the problem of leader-follower formation control in arbitrary dimensional space by exploring persistance of excitation of the desired formation. Using only bearing measurements (also relative velocity for double-integrator dynamics), distributed control laws are derived for a group of agents with single- or double-integrator dynamics. The key contribution is that the (local) exponential stabilization of the actual formation to the desired one is guaranteed as long as the PE conditions on the desired formation are satisfied. The approach generalizes stability results provided in prior work for leader-first follower (LFF) structures which are based on bearing rigidity and constraint consistence of the graph topology to ensure the exponential stabilization of the actual formation to a desired static geometric pattern up to a scale factor. Simulations results are provided to illustrate the performance of the proposed control method.

1.2.4 Relaxed bearing rigidity and bearing formation control under persistence of excitation [TCHS20b, TCHS21]

Chapter 5 extends the bearing formation control law for formations under general undirected graph and propose a general concept, *relaxed bearing rigidity*, which guarantees the uniqueness of a fixed geometric pattern without imposing bearing rigid conditions on the graph topology. By defining a desired formation that is bearing PE, the proposed distributed control laws guarantee exponential stabilization of the desired formation only up to a translation vector without measurement or estimate of any distance between two agents. Simulation results are provided to illustrate the performance of the proposed control method.

1.3 Notations and definitions

$\|\|.\|\|$	the euclidean norm
$\mathbb{S}^{d-1}$	$\{y \in \mathbb{R}^d : \|\|y\|\| = 1\}$
$[\cdot]_\times$	the skew-symmetric matrix associated to its vector argument
$\otimes$	the Kronecker product
$\mathrm{mod}(a, b)$	the remainder of a/b where $a, b \in \mathbb{N}$
$\llcorner r \lrcorner$	the integer part of $r \in \mathbb{R}^+$
$\mathrm{sgn}(.)$	the signum function
$\mathrm{Null}(.)$	the null space a matrix
$\mathrm{tr}\,(.)$	the trace of a matrix

rank(.)	the rank of a matrix
$\lambda_{\max}(.)(\lambda_{\min}(.))$	the maximum (minimum) eigenvalue of its matrix argument
I_d	identity matrix of dimension $d \times d$
$0_d,\ 0_{d\times q}$	zero matrix of dimension $d \times d$ and $d \times q$ $(d \neq q)$, respectively
$\mathbf{1}_n$	$[1,\dots,1]^\top \in \mathbb{R}^n$
$\operatorname{diag}(A_i) \in \mathbb{R}^{nd\times nd}$	the block diagonal matrix with elements given by $A_i \in \mathbb{R}^{d\times d}$ for $i = 1,\dots,n$
$\{\mathcal{I}\}$	the common inertial frame
$\{\mathcal{B}\}$	the body-fixed frame attached to the vehicle's centre of mass
ξ	position vector of the vehicle expressed in $\{\mathcal{I}\}$
ζ	position vector of the vehicle expressed in $\{\mathcal{B}\}$
v	velocity vector of the vehicle expressed in $\{\mathcal{I}\}$
Ω	angular velocity vector of the vehicle expressed in $\{\mathcal{B}\}$
m	vehicle's mass
e_1	$[1\ 0\ 0]^\top$
e_2	$[0\ 1\ 0]^\top$
e_3	$[0\ 0\ 1]^\top$
$\boldsymbol{I}$	the inertia matrix
g	the gravitational acceleration
F_T	the thrust magnitude
π_x	$I - xx^\top \geq 0,\ x \in \mathbb{S}^{d-1}$ $(d \geq 2)$ which is the orthogonal projection operator in $\mathbb{R}^d$ onto the $d-1$-dimensional vector subspace orthogonal to x
ξ_i	position vector of ith agent expressed in $\{\mathcal{I}\}$
v_i	velocity vector of ith agent expressed in $\{\mathcal{I}\}$
$\boldsymbol{\xi}$	stacked position vector of agents expressed in $\{\mathcal{I}\}$
$\boldsymbol{v}$	stacked velocity vector of agents expressed in $\{\mathcal{I}\}$

2

AIRCRAFT LANDING USING DYNAMIC 2D IMAGE-BASED GUIDANCE CONTROL

2.1 Introduction

The landing maneuver is still one of the most critical and dangerous flight phases. Together with the approach phase, it accounts for the majority of airplane accidents, as reported in [FGH03]. The development of reliable autonomous landing systems has been an important research area, which is currently receiving a renewed interest with the advent of unmanned aerial vehicles (UAVs). The key problem of designing an effective autonomous landing system is the difficulty to measure an accurate position of the aircraft with respect to the runway. Most of the airports used for civil aviation are equipped with an instrument landing system (ILS), whereas automatic landing of Unmanned Aerial Vehicles (UAVs) rely on high-precision differential GPS (DGPS) systems combined with tactical grade INS [LH02]. Such systems are expensive and may require a large-scale accurate survey of the airport, making them unsuitable for the large number of smaller recreational airports and for use with small and inexpensive UAVs. In addition, GPS-based navigation systems are vulnerable to disruptions arising from different sources of signal interference both passive and active [Car03]. As described in Chapter 1, cameras are cheap and reliable sensors that can be combined with the outputs of inertial measurement units (IMU) to provide information about the motion of the vehicle relative to the surrounding environment.

In this chapter, we propose a novel approach that we term 2D image-based feedback control and apply it to the problem of automatically steering a fixed-wing UAV during the first three stages of landing: alignment, glide-slope, and flare. These together with taxiing define the standard phases of a complete landing maneuver and can be described as follows [SL03].

1. *Alignment:* The airplane has to align itself with the runway and maintain a fixed desired altitude from the ground.

2. *Glide-Slope:* The airplane follows a straight-line descending path, while keeping the alignment with respect to the runway.

3. *Flare:* When the airplane approaches the runway (at about a 20-m distance for a Jet-sized aircraft), a specific flare maneuver begins to lower the glide-path angle and ensure a touchdown with minimal vertical velocity.

4. *Taxiing:* The last phase of the landing maneuver begins when the airplane touches the runway and acts as a ground vehicle while reducing its velocity.

Although the proposed solution exploits directly visual features in the controller, it differs from classical IBVS schemes in the sense that the derivation of the control law relies on the system dynamics instead of the image features dynamics. It is designed for the guidance dynamics and exploits directly optical flow measurement as a velocity cue along with geometric image features encoding the position with respect to the runway, yielding robustness to camera and target calibration errors. With this approach, we can avoid the main issues encountered in classical IBVS control: 1) requiring estimation of the Jacobian matrix and therefore estimation of the depth of each feature, 2) being specifically designed for kinematic systems.

The use of vision for automatic landing of fixed-wings UAVs has been extensively researched. Noteworthy examples include [VG13, GAR10, BGMB07, TMS+14, KGD10, LKSM13, KKL+13, GBC+15, LBHM+14, SCH+15], to name a few. In [VG13] and [GAR10] classical IBVS controllers are proposed, which explore the image feature dynamics. In [BGMB07] and [TMS+14] optical flow information is used to sense and control the height above the ground, however the height still needs to be estimated. Other solutions, [KGD10, LKSM13, KKL+13, GBC+15], rely on vision to estimate the 3D position and orientation of the aircraft with respect to the runway and then apply a traditional control scheme much in the same way as with an ILS or a DGPS system. To this end, a precise geometric model of the runway is required as well as an extreme care in camera calibration [KGD10, LKSM13, KKL+13].

The proposed work makes some innovations with respect to the prior works [LBHM+14] and [SCH+15] in the guidance control problem. In [LBHM+14] an IBVS control law for the the first two phases of the aircraft landing maneuver (the alignment and the glide-slope) was proposed while in [SCH+15] an IBVS solution for the third phase (flare) of landing is described. The control architecture is however the same and relies on time scale separation between the guidance control (slow dynamics) and the high gain inner-loop flight control (fast dynamics) [19].

The main novelty with respect to [LBHM+14] is the use of optical flow measurements instead of airspeed measurements for the derivative term, which is inspired by the work in [RHMS14]. Using optical flow as a velocity cue eliminates the need for a wind estimator and thus the proposed controller is not augmented with extra estimation states. As a second contribution, the proposed 2D image-based feedback controller relies on writing the kinematics in terms of the 3D position error instead of the visual error and thus enables an alternative proof of stability and has the advantage of imposing less restrictive conditions on the tunable gains. A technical result is also provided, which highlights the fact that the visual error is a passive function of the position error.

For the alignment and glide phases, the position error is encoded in line features, represented by the so-called bi-normalized Plücker coordinates [MH05]. For alignment, these are extracted from images of the side edges of the runway. For the glide phase, virtual line features are derived from the images of the front corners of the runway and the desired glide slope angle. For the flare phase, images of the side edges of the runway are again used but this time in a modified form to provide a direct position error term, simply scaled by the height above the runway. Using the translational optical flow, we obtain a velocity term, which is also scaled by the height above the runway. Compared with [SCH+15], we do not require an explicit separation between the control laws for horizontal alignment and touchdown and estimation of the crosswind is also not required.

This chapter consists of five sections followed by a conclusion. Section 2.2 presents the fundamental equations of motion of the dynamic model considered in this work. Section 2.3 describes the image features that are exploited. Section 2.4 introduces the proposed control strategy and the stability analysis and finally Section 2.5 describes simulations results. The chapter concludes with some final comments in Section 2.6.

2.2 Modeling

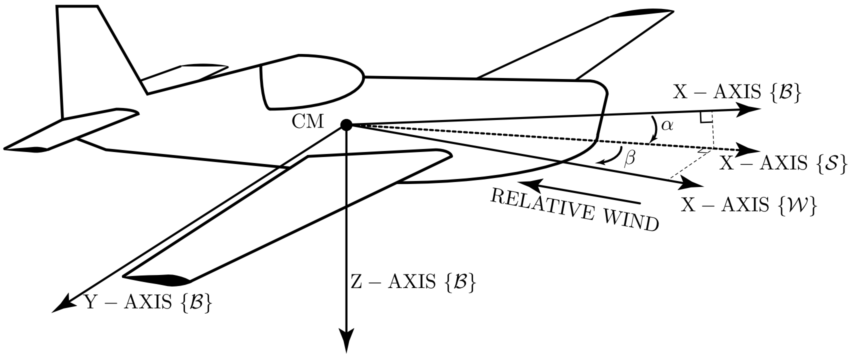

Figure 2.1: Reference frames.

In this section the aircraft dynamic model is briefly described. Let $\{\mathcal{I}\}$ denote the inertial reference frame and $\{\mathcal{B}\}$ denote the body reference frame. Two additional reference frames attached to the vehicle's center of mass are introduced, the stability reference frame $\{\mathcal{S}\}$ and the airspeed reference frame $\{\mathcal{W}\}$, see Fig. 2.1. The angle of attack α defines the orientation of $\{\mathcal{S}\}$ with respect to $\{\mathcal{B}\}$, which is used to analyze the effect of perturbations from steady-state flight.

The airspeed frame $\{\mathcal{W}\}$ is obtained from the stability frame through a rotation about the z-axis by the side-slip angle β. Therefore, the rotation matrices from $\{\mathcal{B}\}$ to $\{\mathcal{W}\}$ is given by

$$ {}^{B}_{W}\mathbf{R} = R_Z(-\beta)R_Y(\alpha) \in SO(3). $$

The flight-path, heading, and bank angles (γ, χ, μ) are the so called wind angles and describe the orientation of the airspeed frame with respect to the inertial frame, such that

$$ {}^{W}_{I}\mathbf{R} = R_Z(\chi)R_Y(\gamma)R_X(\mu) \in SO(3). $$

Assuming the presence of wind with velocity $v_w \in \mathbb{R}^3$ expressed in $\{\mathcal{B}\}$, let $v_a \in \mathbb{R}^3$ denote the velocity of the aircraft relative to the wind expressed in $\{\mathcal{B}\}$ and let ${}^{B}v = v_a + v_w$ denote the aircraft velocity with respect to $\{\mathcal{I}\}$ and expressed in $\{\mathcal{B}\}$. Let $\Omega \in \mathbb{R}^3$ denote the angular velocity expressed in $\{\mathcal{B}\}$, $\xi \in \mathbb{R}^3$ the aircraft position in $\{\mathcal{I}\}$ and $R = {}^{B}_{I}\mathbf{R} \in SO(3)$ the rotation matrix from $\{\mathcal{B}\}$ to $\{\mathcal{I}\}$.

Note that the airplane should not be operated when the wind conditions are higher than a limit identified upon the airplane conception. We also assume that the wind is approximately constant in the inertial frame, yielding the following assumption.

Assumption 2.1. *The wind velocity is constant in the inertial frame. That is:*

$$ \dot{v}_w = -[\Omega]_\times v_w. $$

And there exists $\varepsilon_w \in [0,1)$ such that:

$$ \|v_w\| < \varepsilon_w V, \tag{2.1} $$

where $V = \|v_a\|$.

The standard rigid-body model for a fixed-wing aircraft is given by [Boi98]

$$ \begin{aligned} \dot{\xi} &= R(v_a + v_w) \\ \dot{v}_a &= -[\Omega]_\times v_a + gR^\top e_3 + \frac{F_T}{m}e_1 + {}^{W}_{B}\mathbf{R}F_a(V,\alpha,\beta) \qquad (2.2) \\ \dot{R} &= R[\Omega]_\times \\ \boldsymbol{I}\dot{\Omega} &= -[\Omega]_\times \boldsymbol{I}\Omega + \Gamma_a(V,\Omega,\alpha,\beta,\delta_e,\delta_a,\delta_r), \qquad (2.3) \end{aligned} $$

where g is the gravitational acceleration, m is the mass of the vehicle, $F_T \in \mathbb{R}$ is thrust force magnitude, $F_a \in \mathbb{R}^3$ are the aerodynamic forces expressed in the wind frame, $\boldsymbol{I}$ is the inertia matrix, and $\Gamma_a \in \mathbb{R}^3$ are the aerodynamic moments expressed in the body frame. The force vector F_a can be written as a functions of V, α, and β, whereas Γ_a depends on V, Ω, α, β. The control surfaces deflections δ_e, δ_a, δ_r (elevator, ailerons, and rudder, respectively) and the explicit expressions for F_a and Γ_a can be found in [LBHM+14].

Only partial measurements of the state variables are available. The angular velocity Ω and an estimation of orientation matrix R are provided by the IMU. A set of Pitot tubes provides the measurement of the airspeed v_a in both airspeed magnitude and direction (V, α, β). Combining the measurement of the airspeed direction with R, measurements of (μ, γ, χ) can be obtained. However the position of the aircraft ξ and the wind velocity v_w are unknown.

2.2.1 Control architecture

The aircraft control architecture is designed by resorting to a time scale separation between the guidance control (slow dynamics) and the high gain inner-loop flight control (fast dynamics) [HHMR12]. Let $\zeta \in \mathbb{R}^3$ denote the position of the origin of inertial frame $\{\mathcal{I}\}$, expressed in body frame $\{\mathcal{B}\}$, such that

$$\zeta := -R^\top \xi \tag{2.4}$$

and recall that ${}^B v = v_a + v_w$ denotes the aircraft velocity relative to the inertial frame, expressed in the body frame. Under Assumption 1, the guidance dynamics can be written as

$$\dot{\zeta} = -[\Omega]_\times \zeta - {}^B v \tag{2.5}$$

$${}^B\dot{v} = -[\Omega]_\times {}^B v + F_c, \tag{2.6}$$

where F_c is the sum of total external force defined in (2.2). F_c is used as the control input for the guidance control and its value, which results from the guidance control design, is used to define the references for the high gain flight control system. Following standard procedure, we impose two constraints on the aircraft's motion[LBHM+14]:

1) Constant airspeed: the airspeed magnitude $V = \|v_a\|$ is constant.

2) Bank to turn or slide to turn: the aircraft will bank into any turn to ensure that the slide-slip angle β is zero (typically in the alignment phase) or will slide into any turn to ensure that the bank angle μ is zero (typically in the flare phase).

To enforce the first constraint, it is assumed the aircraft is running any suitable inner-loop control law for the thrust $F_T = F_T^*$ that stabilizes $V = \|v_a\|$ to the desired constant value. Then, (2.6) can be rewritten as

$${}^B\dot{v} = -[\Omega]_\times {}^B v + \pi_{\frac{v_a}{V}} \tau_a(\alpha, \beta, \mu), \tag{2.7}$$

where $\pi_x = I_3 - xx^\top \geq 0,\ \forall x \in \mathbb{S}^2$ is the orthogonal projection operator in R^3 onto the 2-dimensional vector subspace orthogonal to x and $\tau_a \in \mathbb{R}^3$ can be interpreted as a virtual control input. The expression in (2.7) explicitly shows that only the two components of τ_a belonging to the plane orthogonal to v_a are used as input for the guidance system, which follows from the fact that $v_a^T \dot{v}_a = 0$ for constant speeds V. Recalling (2.2) and noting that $R^\top e_3$ can be written in terms of α, β, γ, and μ, one has

$$\tau_a(\alpha, \beta, \mu) = gR^\top e_3 + \frac{F_T^*}{m} e_1 + {}^W_B\mathbf{R} F_a(V, \alpha, \beta),$$

where it is made explicit that τ_a can be written as function of α, β, and μ along with additional known variables V, γ and F_T^*. Enforcing either one of the constraints defined in 2) and provided that the system is within the valid region of operation, we can invert either $\pi_{v_a}\tau_a(\alpha,\beta,0)$ or $\pi_{v_a}\tau_a(\alpha,0,\mu)$ to obtain the desired angles (α^*,β^*,μ^*), which will then be used as references for the inner-loop flight control system. For that purpose, the dynamics of α, β, and μ along with that of Ω given in (2.3) need to be considered, yielding a strongly coupled and highly nonlinear system with inputs given by the deflections of the aircraft control surfaces. A detailed description of the inner-loop flight controller design is beyond the scope of this chapter and can be found in [LBHM+14, section 2]. The approach followed to obtain an inner-loop controller that stabilizes the orientation and regulates (α,β,μ) to the reference angles (α^*,β^*,μ^*) can be summarized as follows: i) consider the system with state given by $\varsigma = [\alpha,\beta,\mu,\Omega^\top]^\top$ and input given by $\delta_s = [\delta_a,\delta_e,\delta_r]^\top$, ii) assuming that V is constant and the reference angles (α^*,β^*,μ^*) are slowly time-varying, linearize the system (with state given by ς and input given by δ_s) about the corresponding equilibrium points, iii) design a controller for the resulting LPV system. The controller obtained ensures that $(\alpha,\beta,\mu) = (\alpha^*,\beta^*,\mu^*)$ is locally exponentially stable, with an adequate choice of high gain.

For the rest of the chapter, it is assumed that the aircraft is running any suitable inner-loop controller stabilizing V at a desired constant value and the angles $(\alpha,\beta,\ \mu)$ at the desired values $(\alpha_1^*,\ 0,\ \mu_1^*)$ or $(\alpha_2^*\ ,\beta_2^*,\ 0)$.

2.3 Image Features

To perform the landing maneuver using an 2D image-based controller, adequate image features need to be defined. The side borders of the runway can be used to provide information for aligning the aircraft with the runway, whereas the ground texture, specially on the sideways of the runway, can be used to obtain information about the velocity relative to the ground and ensure a smooth landing. To address the problem, we consider the following additional assumptions:

Assumption 2.2. *The camera is attached to the center of mass of the aircraft, so that the camera reference frame coincides with the body-fixed reference frame.*

Assumption 2.3. *The runway is placed on a flat, horizontal, and textured surface, which defines the target plane. The normal to the target plane coincides with the gravitational force and its coordinates in $\{\mathcal{B}\}$ denoted by $\eta_A \in \mathbb{S}^2$ are assumed to be known.*

Note that for non-aggressive maneuvers, it is reasonable to assume that the IMU can provide good estimates for η_A. To define an inertial reference frame $\{\mathcal{I}\}$, we introduce a unit vector that coincides with the main axis of the runway and has coordinates $u_A \in \mathbb{S}^2$ expressed in $\{\mathcal{B}\}$. This vector will be extracted from images features, as shown below. The axes of $\{\mathcal{I}\}$ expressed in $\{\mathcal{B}\}$ are then given by (u_A, ρ, η_A), where $\rho = \eta_A \times u_A$. For convenience but without loss of generality, the origin of $\{\mathcal{I}\}$ is placed at the front border of runway, equally distant from the sideways (see Fig. 2.2).

2.3.1 Image features for the alignment phase

As shown in Fig. 2.2, we consider that two parallel straight lines define the edges of the runway along the direction u_A (full length direction). According to the placement of the inertial frame $\{\mathcal{I}\}$, the front corner points of each line expressed in the inertial frame are defined as $\mathring{s}_1 = [0\ -s\ 0]^\top$ and $\mathring{s}_2 = [0\ s\ 0]^\top$.

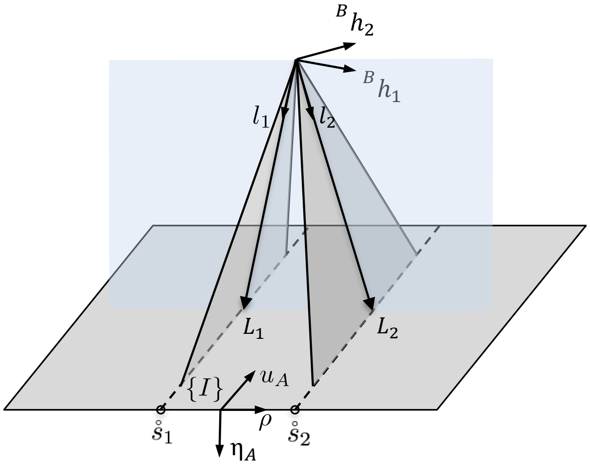

Figure 2.2: Parallel lines and the binormalized Plücker coordinates ${}^Bh_i$.

The unit vector ${}^Bh_i \in \mathbb{S}^2$ normal to the plane defined by the camera/body frame $\{\mathcal{B}\}$ together with ith line of the runway, can be directly obtained from the image of the line as introduces in Section A.3 in the Appendix. If at least two lines are observed, then the direction u_A can be readily obtained from

$$u_A = \frac{{}^Bh_2 \times {}^Bh_1}{\|{}^Bh_2 \times {}^Bh_1\|}.$$

Consider the goal of the alignment phase as that of aligning the aircraft with the center of the runway and maintaining a fixed height above the ground. The visual feature used for control purposes in the alignment phase encodes information about the position of the aircraft relative to the straight lines and is defined as

$$q_A := \frac{1}{2}(l_1 + l_2) \in \mathbb{R}^3,$$

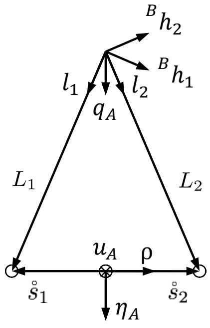

Figure 2.3: Projection on the plane orthogonal to u_A.

where

$$l_i = u_A \times {}^B h_i \in \mathbb{S}^2, \tag{2.8}$$

and q_A can be obtained directly from image measurements only. As shown in Figures 2.2 and 2.3, (2.8) simply amounts to applying a 90 degree rotation about u_A, so that the new unit vectors l_i point from the camera to each line. Figure 2.3 also shows that l_i can be rewritten as

$$l_i = \frac{L_i}{||L_i||},$$

where L_i is the projection on the plane orthogonal to u_A (represented in Fig. 2.2 by the light colored plane) of any vector going from the camera to any point on the line. Recalling (2.4), the vector L_i can be written as

$$L_i = R^\top \mathring{s}_i + \pi_{u_A}\zeta.$$

The desired image feature is defined as

$$q_A^* = \frac{1}{2}(l_1^* + l_2^*) = \frac{1}{2}\left(\frac{L_1^*}{||L_1^*||} + \frac{L_2^*}{||L_2^*||}\right),$$

where $L_i^* = R^\top \mathring{s}_i + \pi_{u_A}\zeta^*$. Then, the control objective can be defined as guaranteeing the convergence of q_A to q_A^* via the asymptotic regulation of $\pi_{u_A}\zeta - \pi_{u_A}\zeta^*$ to zero. Define the height of the aircraft above the runway along the direction η_A as

$$d_A := \eta_A^\top L_i.$$

To align the aircraft with the center of the runway and keep it at constant height d_A^* above the ground, the desired vector $\pi_{u_A}\zeta^*$ is defined as $\pi_{u_A}\zeta^* := d_A^*\eta_A$. By a direct application of Lemma A.1, as long as $d_A > 0$, there is an one-to-one mapping between the image feature q_A and $\pi_{u_A}\zeta$. Hence achieving alignment, $\pi_{u_A}\zeta = \pi_{u_A}\zeta^*$, is equivalent to having $q_A = q_A^*$ and these measurements can be directly obtained from the geometric image features.

2.3.2 Image features for the glide phase

For the glide phase, the aircraft should follow a straight-line descending path, while maintaining the alignment with respect to the runway. To define the visual features for this phase, we propose to use the front corners of the runway along with a prespecified desired descent direction. Let $P_i^{'} = R^\top \mathring{s}_i + \zeta \in \mathbb{R}^3$ denote the coordinates in $\{\mathcal{B}\}$ of the front corner points of the runway. Adopting the same approach as in [LBHM$^+$14], we construct virtual lines starting from the corner points with a pre-specified glide direction $u_G \in \mathbb{S}^2$ expressed in the body frame

$$u_G = \cos\gamma^* u_A + \sin\gamma^* \eta_A,$$

and normal direction $\eta_G \in \mathbb{S}^2$ expressed in the body frame as

$$\eta_G = -\sin\gamma^* u_A + \cos\gamma^* \eta_A,$$

where γ^* is the angle of the desired glide slope with respect to ground (see Fig. 2.4). Notice that $\dot{u}_G = -[\Omega]_\times u_G$ since the angle γ^* is constant along the glide path.

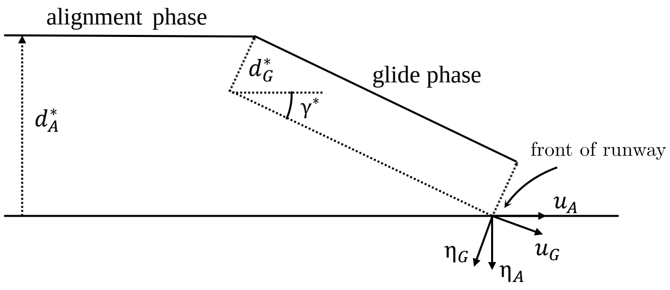

Figure 2.4: Flight phases.

The visual feature used for control purposes in glide phase is defined by

$$q_G := \frac{1}{2}(\mathring{g}_1 + \mathring{g}_2) \in \mathbb{R}^3,$$

where

$$\mathring{g}_i = \frac{\pi_{u_G} p_i^{'}}{\|\pi_{u_G} p_i^{'}\|} \in \mathbb{S}^2,$$

and hence the vector q_G can be directly obtained from u_G and the spherical images of the front corners $p_i^{'} = \frac{P_i^{'}}{\|P_i^{'}\|}$ ($p_i^{'}$ can be obtained using the sequence of 2D pixel locations from the camera as presented in Section A.1). $\mathring{g}_i$ can also be rewritten as $\mathring{g}_i = \frac{G_i}{\|G_i\|}$, where

$$G_i = \pi_{u_G} P_i^{'} = R^\top \mathring{s}_i + \pi_{u_G} \zeta.$$

Define the height of the aircraft above the virtual lines along the direction η_G as

$$d_G := \eta_G^\top G_i.$$

Similarly to the alignment phase, the control objective for the glide phase can be defined as ensuring the convergence of q_G to q_G^* via the asymptotic regulation of the error $\pi_{u_G}\zeta - \pi_{u_G}\zeta^*$ to zero, where $\pi_{u_G}\zeta^* = d_G^*\eta_G$ and d_G^* is the desired value of d_G. Again, by a direct application of Lemma A.1, we can conclude that, for $d_G > 0$, there is an one-to-one mapping between the image feature q_G and $\pi_{u_G}\zeta$.

2.3.3 Image features for the flare phase

The goal of the flare phase is to steer the airplane so that it lands smoothly on the center of the runway and aligned with the direction u_A, while keeping a constant speed along the maneuver. The flare maneuver can be defined as driving $\pi_{u_A}\zeta$ to zero with exponential convergence along the vertical direction η_A to ensure a smooth touchdown. To achieve this goal using a 2D image-based feedback control law, we slightly modify the visual feature that was defined for the alignment phase and consider

$$q_F := \frac{1}{2}\left(\frac{l_1}{\eta_A^\top l_1} + \frac{l_2}{\eta_A^\top l_2}\right) = \frac{1}{2}\left(\frac{L_1}{\eta_A^\top L_1} + \frac{L_2}{\eta_A^\top L_2}\right),$$

recalling that $l_i = \frac{L_i}{\|L_i\|}$ and the height d_A above the ground is given by $d_A = \eta_A^\top L_1 = \eta_A^\top L_2$, one can remark that q_F can also be written as a function of the system state:

$$q_F = \frac{\pi_{u_A}\zeta}{d_A}.$$

2.3.4 Image Kinematics and Translational Optical Flow

To obtain optical flow measurements to be used as velocity cue in the 2D image-based controller, it is assumed that the sideways of the runway are rich in texture. The kinematics of any observed points can be written in the body-fixed frame:

$${}^B\dot{P} = -[\Omega]_\times {}^BP - {}^Bv,$$

where ${}^BP \in \mathbb{R}^3$ denotes a point on the textured ground. Similarly to Section A.4 in the appendix, the translational optical flow with respect to the text ground

$$w(t) = \frac{{}^Bv(t)}{d_A(t)}, \tag{2.9}$$

can be obtained from the integral of the kinematics of the image point ${}^Bp = \frac{{}^BP}{\|{}^BP\|}$:

$${}^B\dot{p} = -[\Omega]_\times {}^Bp - \cos\theta_A \pi_{{}^Bp} \frac{{}^Bv}{d_A}$$

along direction η_A over a solid angle, where $\theta_A = \eta_A^{\top B}p$.

2.4 Vision-based Control

In this section, the three phases of the landing maneuver (alignment, glide and flare) are considered, assuming the presence of a constant wind disturbance. Adopting the guidance dynamics described in Section 2.2, we propose an outer-loop control law that only relies on image measurements to: i) align the aircraft with the center of the runway, ii) perform the glide-slope maneuver, and iii) enforce a smooth landing in the flare phase. For that purpose, the controller must ensure that the height above the ground d_A is positive at all times and $d_A = 0$ is exponentially reached with zero velocity, during the flare phase. The obvious constraint of guaranteeing that d_A remains positive, together with the fact that d_A is unknown, adds complexity to the control problem and requires careful consideration in the stability analysis.

We recall the guidance kinematics and dynamics (2.5) and (2.7) and define the input τ_a as

$$\tau_a = -(v_a)_\times (u_{(.)})_\times \frac{F}{v_a^\top u_{(.)}} = \left(I_3 - \frac{u_{(.)} v_a^T}{u_{(.)}^T v_a} \right) \pi_{u_{(.)}} F, \tag{2.10}$$

where $u_{(.)}$ stands for either u_A or u_G depending on which landing phase (u_A for alignment and flare, u_G for glide-slop) is considered and $F \in \mathbb{R}^3$ is the force applied to the aircraft yet to be defined, which will have different expressions for alignment, glide and flare phases denoted by F_A, F_G and F_F respectively. Note that (2.10) is well-defined provided that

$$u_{(.)}^\top v_a(t) > 0, \text{for all } t \geq 0. \tag{2.11}$$

Rewriting the guidance system (2.5) and (2.7) with τ_a given by (2.10), we obtain

$$\begin{aligned} \dot{\zeta} &= -[\Omega]_\times \zeta - {}^B v \\ {}^B\dot{v} &= -[\Omega]_\times {}^B v - u_{(.)} \frac{v_a^\top \pi_{u_{(.)}} F}{v_a^\top u_{(.)}} + \pi_{u_{(.)}} F, \end{aligned} \tag{2.12}$$

where for convenience the input was decomposed into two terms, one parallel and the other orthogonal to $u_{(.)}$.

In what follows, let $\zeta_{(.)} := \pi_{u_{(.)}} \zeta \in \mathbb{R}^3$ and $v_{(.)} := \pi_{u_{(.)}} {}^B v \in \mathbb{R}^3$ denote the components orthogonal to $u_{(.)}$ and let $\zeta_\rho := \rho^\top \zeta \in \mathbb{R}$, $v_\rho := \rho^{\top B} v \in \mathbb{R}$ denotes the components along ρ. Assuming for now that (2.11) holds, we obtain

$$\begin{cases} \dot{\zeta}_{(.)} = -[\Omega]_\times \zeta_{(.)} - v_{(.)} \\ \dot{v}_{(.)} = -[\Omega]_\times v_{(.)} + \pi_{u_{(.)}} F, \end{cases} \tag{2.13}$$

recalling that $F = F_A$ for the alignment phase, $F = F_G$ for the glide phase, and $F = F_F$ for the flare phase. The control laws are given by

$$F_A = k_1(q_A - q_A^*) - \frac{k_2}{u_A^\top v_a}\pi_{u_A} w \tag{2.14}$$

$$F_G = k_3(q_G - q_G^*) - \frac{k_4}{u_G^\top v_a}\pi_{u_G} w \tag{2.15}$$

$$F_F = k_5 q_F - k_6 \pi_{u_A} w, \tag{2.16}$$

where k_1, k_2, k_5, k_6, k_5, and k_6 are positive gains. Recalling (2.9), equations (2.14), (2.15), and (2.16) can also be written as PD-like control laws

$$\begin{aligned} F_A &= k_1(q_A - q_A^*) - \frac{k_2}{u_A^\top v_a}\frac{v_A}{d_A} \\ F_G &= k_3(q_G - q_G^*) - \frac{k_4}{u_G^\top v_a}\frac{v_G}{d_A} \\ F_F &= k_5 \frac{\zeta_A}{d_A} - k_6 \frac{v_A}{d_A}. \end{aligned}$$

The proportional term in F_A and F_G, given by $q_{(.)} - q_{(.)}^*$, is a nonlinear function of the position error $\tilde{\zeta}_{(.)} = \zeta_{(.)} - \zeta_{(.)}^*$, with $\zeta_A^* = d_A^* \eta_A$ for alignment and $\zeta_G^* = d_G^* \eta_G$ for glide. We note that according to (A.5), $q_{(.)} - q_{(.)}^*$ can be written as

$$q_{(.)} - q_{(.)}^* = \bar{Q}_{(.)} \tilde{\zeta}_{(.)},$$

where $\bar{Q}_{(.)}$ is a positive definite matrix provided that $d_A > 0$ and $d_G > 0$, meaning that

$$(q_{(.)} - q_{(.)}^*)^\top \tilde{\zeta}_{(.)} = \tilde{\zeta}_{(.)}^\top \bar{Q}_{(.)} \tilde{\zeta}_{(.)} > 0,$$

which highlights the fact that the image feature error $q_{(.)} - q_{(.)}^*$ is a strictly passive memoryless function of $\tilde{\zeta}_{(.)}$[Kha92]. The passive property guarantees that $\int_{\zeta_{(.)}^*}^{\zeta_{(.)}} (q_{(.)}(x) - q_{(.)}^*)^\top dx$ is a positive-definite function of $\tilde{\zeta}_{(.)}$, hence one can use this integral as a storage function for stability analysis which will be introduced later.

All other terms are linear with parameter-varying gains that arise from the division by d_A and also by $u_{(.)}^\top v_a$ for the derivative terms in (2.14) and (2.15). The latter is included to provide a high-gain feedback that moves the system away from the condition $u_{(.)}^\top v_a = 0$. To show that $u_{(.)}^\top v_a$ is a parameter-(and not a time)-varying gain, it suffices to recall Assumption 2.1 and rewrite $u_{(.)}^\top v_a$ as follows:

$$u_{(.)}^\top v_a = \sqrt{V^2 - \|v_{(.)} - \pi_{u_{(.)}} v_w\|^2}.$$

The division by d_A arises from the direct use of image features and provides the important property that the distance will remain always positive, while guaranteeing asymptotic stability of the errors for the alignment and glide phases and robust exponential convergence of the errors for the flare phase.

Theorem 2.1. *Consider the system (2.13) in closed-loop with the control law (2.14) for the alignment phase. If there exists a sufficiently small constant* $\epsilon_a > 0$ *such that for any initial condition the following constraints are satisfied:*

$$u_A(t_0)^\top v_a(t_0) \geq \epsilon_a V > 0 \text{ and } d_A(t_0) > 0,$$

then the closed-loop system is well defined for all $t \geq t_0$ *and the following items hold:*
(1) $u_A(t)^\top v_a(t)$ *is bounded and* $u_A(t)^\top v_a(t) \geq \epsilon_a V > 0$*, for all* $t \geq t_0$*;*
(2) the distance $d_A(t)$ *is positive and bounded for all* $t \geq t_0$*;*
(3) the equilibrium point $(\zeta_A, v_A) = (\zeta_A^*, 0)$ *is asymptotically stable.*

Proof. Item (1):

Since it is assumed that $\|v_a\|$ is regulated to the constant V by a fast inner-loop controller, it follows that $|u_A(t)^\top v_a(t)| \leq V$ and thus $u_A(t)^\top v_a(t)$ is bounded for all $t \geq t_0$.

To show $u_A(t)^\top v_a(t) \geq \epsilon_a V > 0$, define a storage function

$$\mathcal{S}(v_a) = V - u_A^\top v_a, \tag{2.17}$$

and note that $\mathcal{S}(v_a) = 0$ when $v_a = V u_A$ and $\mathcal{S}(v_a) = V(1 - \epsilon_a)$ when $u_A^\top v_a = \epsilon_a V$. To show that $u_A^\top v_a(t) \geq \epsilon_a V > 0$ for all $t > t_0$ if $u_A^\top v_a(t_0) \geq \epsilon_a V > 0$, it suffices to show that $\mathcal{S}(v_a) \leq V(1 - \epsilon_a)$ defines a positively invariant set, or equivalently that $\dot{\mathcal{S}}$ is negative definite when $u_A^\top v_a = \epsilon_a V$, with ϵ_a arbitrarily small. Using (2.12) and (2.14), we can write

$$\frac{d_A(u_A^\top v_a)}{dt} = \frac{1}{u_A^\top v_a}[-k_1 v_a^\top (q_A - q_A^*) + \frac{k_2}{u_A^\top v_a} v_a^\top \pi_{u_A} \frac{v_a + v_w}{d_A}],$$

and

$$\dot{\mathcal{S}} = -\frac{k_2}{d_A(u_A^\top v_a)^2}[v_a^\top \pi_{u_A}(v_a + v_w) - \frac{k_1}{k_2} d_A(u_A^\top v_a) v_a^\top (q_A - q_A^*)],$$

so the derivative of $\mathcal{S}$ can be upper bounded by

$$\dot{\mathcal{S}} \leq -\frac{k_2 \|\pi_{u_A} v_a\|}{d_A(u_A^\top v_a)^2}(\|\pi_{u_A} v_a\| - \|v_w\| - \frac{k_1}{k_2} d_A |u_A^\top v_a| \|q_A - q_A^*\|).$$

Using the bounds $\|v_w\| < \varepsilon_w V$ and $\|q_A - q_A^*\| \leq 2$, $\dot{\mathcal{S}}$ can be further upper bounded by

$$\dot{\mathcal{S}} \leq -\frac{k_2 \|\pi_{u_A} v_a\|}{d_A(u_A^\top v_a)^2}(\|\pi_{u_A} v_a\| - \varepsilon_w V - 2\frac{k_1}{k_2} d_A |u_A^\top v_a|),$$

showing that if

$$\|\pi_{u_A} v_a\| > \epsilon_w V + 2\frac{k_1}{k_2} d_A |u_A^\top v_a|, \tag{2.18}$$

then $\dot{\mathcal{S}} < 0$. If $u_A^\top v_a = \epsilon_a V$, $\|\pi_{u_A} v_a\| = V\sqrt{(1 - \epsilon_a^2)}$, and (2.18) becomes

$$\sqrt{1 - \epsilon_a^2} > \epsilon_w + 2\frac{k_1}{k_2} d_A \epsilon_a, \tag{2.19}$$

leading that $0 < \epsilon_a < \frac{-2\frac{k_1}{k_2}\epsilon_w d_A + \sqrt{4\frac{k_1^2}{k_2^2}d_A^2 + 1 - \epsilon_w^2}}{4\frac{k_1^2}{k_2^2}d_A^2 + 1} < 1$, as long as d_A is bounded (which will be shown further ahead in the proof), condition (2.19) will always be satisfied for ϵ_a sufficiently small, meaning that v_a will not cross the boundary $u_A^\top v_a = \epsilon_a V$.

Proof of item (2):

The proof follows similar arguments to those presented [RHMS14]. Considering the error states $\tilde{\zeta}_A = \zeta_A - \zeta_A^*$ and v_A, we start by defining a positive definite storage function $\mathcal{L}_2(\tilde{\zeta}_A, v_A)$, and showing that if $d(t)$ remains positive, $\dot{\mathcal{L}}_2$ is negative semi-definite, meaning that the states $\zeta_A = \tilde{\zeta}_A + \zeta_A^*$ and v_A remain bounded. Define $\mathcal{L}_2$ as

$$\mathcal{L}_2(\tilde{\zeta}_A, v_A) = k_1 \mathcal{L}_1(\tilde{\zeta}_A) + \frac{1}{2}\|v_A\|^2,$$

where $\mathcal{L}_1$ is the line integral given by

$$\mathcal{L}_1(\tilde{\zeta}_A) = \int_{\zeta_A^*}^{\zeta_A} (q_A(x) - q_A^*)^\top dx,$$

and the integration can be taken over any path from ζ_A^* to ζ_A. The proof that $\mathcal{L}_1$ is a positive definite function of $\tilde{\zeta}_A$ is given in Lemma A.2 in the appendix.

Taking the time derivative of $\mathcal{L}_2$ and using (2.14), we can conclude that

$$\begin{aligned}\dot{\mathcal{L}}_2 &= -k_1(q_A - q_A^*)^\top v_A + v_A^\top F_A \\ &= -\frac{k_2}{d u_A^\top v_a}\|v_A\|^2 \leq 0,\end{aligned}$$

which guarantees that ζ_A and v_A are bounded, provided that d_A remains positive.

To show that d_A remains positive, we note that $d_A = \eta_A^\top \zeta$ with dynamics given by

$$\ddot{d}_A = -k_1 \eta_A^\top (q_A - q_A^*) - \frac{k_2}{u_A^\top v_a}\frac{\dot{d}_A}{d_A}. \tag{2.20}$$

Using arguments similar to those in [RHMS14], we can rearrange the terms in (2.20) and integrate them to obtain

$$k_2(\log d_A(t) - \log d_A(t_0)) = -\int_{t_0}^{t} (u_A^\top v_a)(k_1 \eta_A^\top (q_A - q_A^*) + \ddot{d}_A) d\tau, \tag{2.21}$$

where the dependence on τ is omitted to simplify the notation. By showing that, for finite t, the integral term in (2.21) is bounded, we can conclude that $\log d_A(t)$ does not go to $-\infty$ in finite time and thus $d_A(t)$ cannot reach zero in finite time and remains positive for all time. The first term $\int_{t_0}^{t} (u_A^\top v_a) k_1 \eta_A^\top (q_A - q_A^*) d\tau$ is bounded because all terms inside the integral are bounded. To show that $\int_{t_0}^{t} (u_A^\top v_a) \ddot{d}_A \, d\tau$ is bounded, we use the fact that $\epsilon_a V \leq u_A^\top v_a \leq V$, implying that

$$\left| \int_{t_0}^{t} (u_A^\top v_a) \ddot{d}_A \, d\tau \right| \leq V \int_{t_0}^{t} \left| \ddot{d}_A \right| d\tau,$$

which can be solved by splitting the time interval $[t_0, t]$ into smaller intervals, such that inside those intervals the sign of $\ddot{d}_A$ does not change. For each of these intervals of integration, $\int_{t_i}^{t_j} \left|\ddot{d}_A\right| d\tau$ is either given by $\dot{d}_A(t_i) - \dot{d}_A(t_j)$ or its symmetric, and since $\dot{d}_A$ is bounded as shown previously, we can conclude that $\int_{t_0}^{t} \left|\ddot{d}_A\right| d\tau$ is bounded for finite t, the right-hand side of (2.21) is bounded, and thus d_A remains positive for all time.
Proof of item (3):

Using the storage function $\mathcal{L}_2$ defined in proof of item *(2)*, define the set $E := \{(\zeta_A, v_A) : \dot{L}_2(\zeta_A, v_A) = 0\} = \{(\zeta_A, v_A) : v_A = 0\}$. Since $v_A \equiv 0$ implies that $\dot{v}_A \equiv 0$ and these two conditions imply that $\zeta_A \equiv \zeta_A^*$, it follows that the largest invariant set in E includes only the trivial solution $v_A \equiv 0$ and $\zeta_A \equiv \zeta_A^*$. Using the fact that f or any $x \in \mathbb{R}^3$, $[\Omega]_\times x$ is a passive term (i.e. $x^\top [\Omega]_\times x = 0$, see Remark 2.1), one can apply LaSalle's invariance principle from which one concludes that $(\zeta_A, v_A) = (\zeta_A^*, 0)$ is asymptotically stable. □

Remark 2.1. Notice that although the guidance dynamics is expressed in the body frame where the angular velocity Ω appears in the state dynamics (2.13), applying LaSalle's principal here for the stability proof is relevant and appropriate. The stability issues considered in this chapter concern only the guidance part of the problem (a subsystem of the full dynamics of the airplane). One could think that expressing the guidance dynamics in the body-fixed frame introduces, due to the presence Ω, dynamic coupling that seems problematic. Clearly, if one represents the guidance dynamics in the inertial frame, Ω does not appear into the subsystem dynamics. The difference between the two representations is simply a change of coordinates and does not change the structural properties of the subsystem since this change of variable is passive with respect to change of reference frame. That is the energy due to $[\Omega]_\times \zeta_A$ (respectively $[\Omega]_\times v_A$) is zero because $[\Omega]_\times \zeta_A$ is orthogonal to ζ_A (respectively $[\Omega]_\times v_A$ is orthogonal to v_A).

Proposition 2.1. *Consider the system (2.13) in closed-loop with the control law* (2.15) *for the glide phase. If there exists a sufficiently small constant $\epsilon_a > 0$ such that for any initial condition the following constraints are satisfied:*

$$u_G(t_1)^\top v_a(t_1) \geq \epsilon_a V > 0, d(t_1) > 0,$$

and

$$\mathcal{L}_4(\tilde{\zeta}_G(t_1), v_G(t_1)) < s(1 - \frac{s}{\sqrt{s^2 + d_G^{*2}}}) \tag{2.22}$$

with the function

$$\mathcal{L}_4(\tilde{\zeta}_G(t), v_G(t)) = \int_{\zeta_G^*}^{\zeta_G(t)} (q_G(x) - q_G^*)^\top dx + \frac{1}{2}\|v_G(t)\|^2,$$

then the closed-loop system is well defined for all $t \geq t_1$ and the following items hold:
(1) $u_G(t)^\top v_a(t)$ is bounded and $u_G(t)^\top v_a(t) \geq \epsilon_a V > 0$, for all $t \geq t_1$;

(2) the distance $d_A(t)$ is positive and bounded for all $t \geq t_1$;

(3) the equilibrium point $(\zeta_G, v_G) = (\zeta_G^*, 0)$ is asymptotically stable;

(4) $d_G(t)$ is positive and $\mathring{g}_i(\zeta_G(t))$ is well defined for all $t \geq t_1$.

Proof. The proof of the first three items is identical to that of Theorem 2.1.

Proof of Item (4):

Using arguments similar to those in Lemma A.2 in the Appendix, one can show that $\mathcal{L}_3 = \int_{\zeta_G^*}^{\zeta_G} (q_G(x) - q_G^*)^\top dx$ is a positive definite function and its explicit form is

$$\mathcal{L}_3(\tilde{\zeta}_G) = \|G_1\|(1 - \mathring{g}_1^\top \mathring{g}_1^*) + \|G_2\|(1 - \mathring{g}_2^\top \mathring{g}_2^*). \tag{2.23}$$

Using (2.23), one can show that $\mathcal{L}_3(\tilde{\zeta}_G(t)) < s(1 - \frac{s}{\sqrt{s^2+d_G^{*2}}})$ is a sufficient condition to guarantee that $d_G(t) > 0$. Then since $\dot{\mathcal{L}}_4$ is negative semi-definite (similarly to $\dot{\mathcal{L}}_2$ in Proof of Theorem 2.1), $\mathcal{L}_4$ is non-increasing and for any initial condition such that (2.22) is satisfied,

$$\mathcal{L}_3(\tilde{\zeta}_G(t)) \leq \mathcal{L}_4(\tilde{\zeta}_G(t), v_G(t)) < s(1 - \frac{s}{\sqrt{s^2 + d_G^{*2}}}),$$

for all $t \geq t_1$, which implies that $d_G(t)$ is positive and $\mathring{g}_i(\zeta_G(t))$ is well defined for all $t \geq t_1$. ☐

Theorem 2.2. *Consider the system (2.13) along with the control law (2.16) for the flare phase. If there exists a sufficiently small constant $\epsilon_a > 0$ such that for any initial condition the following constraints are satisfied:*

$$u_A(t_2)^\top v_a(t_2) \geq \epsilon_a V > 0, \; d_A(t_2) > 0,$$

and

$$\sqrt{\mathcal{L}(t_2)} \leq \frac{k_6}{k_5} \min\{k_6, V(\sqrt{1-\epsilon_a^2}) - \epsilon_w\} \tag{2.24}$$

with the function

$$\mathcal{L}(t) = \frac{1}{2}\zeta_\rho^2(t) + \frac{k_6^2}{2k_5^2}(v_\rho(t) - \frac{k_5}{k_6}\zeta_\rho(t))^2 + \max\{d_A(t)\exp\{\frac{\dot{d}_A(t)}{k_6}\}, d_A(t)\}^2, \tag{2.25}$$

then closed-loop system is well-defined for all $t \geq t_2$ and the following items hold:

(1) the state (ζ_A, v_A) is bounded for all $t \geq t_2$ and converges asymptotically to zero;

(2) the distance $d_A(t)$ is positive and bounded for all $t \geq t_2$ and converges exponentially to zero;

(3) $u_A(t)^\top v_a(t)$ is bounded and $u_A(t)^\top v_a(t) \geq \epsilon_a V > 0$, for all $t \geq t_2$.

Before proceeding to the proof of Theorem 2.2, we note that the closed-loop system for the flare phase can be written as

$$\left\{\begin{aligned} \dot{\zeta}_A &= -[\Omega]_\times \zeta_A - v_A \\ \dot{v}_A &= -[\Omega]_\times v_A + k_5\frac{\zeta_A}{d_A} - k_6\frac{v_A}{d_A} \\ \frac{d(u_A^\top v_a)}{dt} &= -\frac{1}{d_A(u_A^\top v_a)} v_a^\top (k_5\zeta_A - k_6\pi_{u_A}(v_a + v_w)), \end{aligned}\right. \tag{2.26}$$

where we recall that ${}^{B}v = v_a + v_w$. Then, the first step to show that (ζ_A, v_A) converges to zero and $u_A^\top v_a$ remains positive is to determine whether or not $u_A^\top v_a$ is positive when $(\zeta_A, v_A) \to (0,0)$. Recalling that $\|v_a\| = V$, it follows that when $v_A = \pi_{u_A}(v_a + v_w) \to 0$, $u_A^\top v_a$ converges to either $\sqrt{V^2 - \|\pi_{u_A} v_w\|^2}$ or $-\sqrt{V^2 - \|\pi_{u_A} v_w\|^2}$. Then, the desired equilibrium for $u_A^\top v_a$ is $\sqrt{V^2 - \|\pi_{u_A} v_w\|^2}$, which is lower bounded by $V\sqrt{1-\epsilon_w^2} > 0$, provided that the wind velocity satisfies Assumption 2.1.

Proof. item (1):
By noting that $(d_A, \dot{d}_A) = (\eta_A^\top \zeta, -\eta_A^\top v)$ and considering the closed-loop system formed by (2.13) and (2.16), the dynamics of d_A can be written as

$$\ddot{d}_A = -k_6\Big(\frac{\dot{d}_A}{d_A} + w_d\Big),$$

where $w_d = \frac{k_5}{k_6}$.

According to the proof of Theorem 5.1 in [HHMR12], we can define the auxiliary variable

$$\lambda(t) = d_A(t)\exp\{\frac{\dot{d}_A}{k_6}\}, \tag{2.27}$$

and considering the change of variables from $(d_A, \dot{d}_A)$ to (d_A, λ), obtain a new description for the system given by

$$\begin{aligned} \dot{d}_A(t) &= -k_6\Big(\log d_A(t) - \log \lambda(t)\Big) \\ \dot{\lambda}(t) &= -w_d \lambda(t), \end{aligned} \tag{2.28}$$

which is well-defined for $d_A(t) > 0$ and $\lambda(t) > 0$. From (2.28), it follows that $\lambda(t) = \lambda(t_2)\exp(-w_d t)$, which is positive for all $t \geq t_2$, provided that $\lambda(t_2) > 0$ or equivalently $d_A(t_2) > 0$. If $d_A(t_2) < \lambda(t_2)$, then $\dot{d}_A(t_2) > 0$ and $d_A(t)$ increases while $\lambda(t)$ is decreasing to zero, meaning that there exists a time $T_1 \geq 0$ such that $d_A(T_1) = \lambda(T_1)$ and $d_A(t)$ cannot grow unbounded. After crossing the line $d_A = \lambda$ at $t = T_1$, $\dot{d}_A(t)$ becomes negative and $d_A(t)$ starts decreasing together with $\lambda(t)$ and both converge monotonically to zero, without crossing either the line $d_A = \lambda$ or the line $d_A = 0$, as shown in Fig. 2.5.

To show that $\dot{d}_A(t)$ also converges to zero, consider the storage function

$$\mathcal{L}_5 = \frac{1}{2}\dot{d}_A^2$$

with time derivative given by

$$\dot{\mathcal{L}}_5 = -k_6\frac{\dot{d}_A}{d_A}(\dot{d}_A + w_d d_A). \tag{2.29}$$

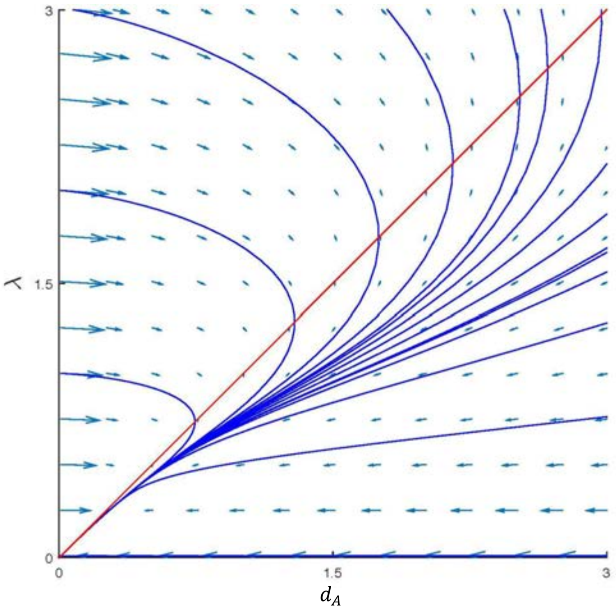

Figure 2.5: Phase portrait of the evolution of the state (d_A,λ).

Then, the function $\mathcal{L}_5$ is decreasing as long as $|\dot{d}_A(t)| > w_d d_A(t)$. Since $d_A(t)$ is positive and converging to zero, we can conclude that $|\dot{d}_A(t)|$ is bounded and converging to zero. Finally, to show that $d_A(t)$ and $\dot{d}_A(t)$ are bounded by exponentially decaying functions, we can write the solution of (2.28) as a function of $d_A(t)$ and $\dot{d}_A(t)$ to obtain

$$0 < \sigma_1 d_A(t_2)\,\exp\{-w_d t\} \leq d_A(t) \leq \sigma_2 d_A(t_2)\,\exp\{-w_d t\},$$

where $\sigma_1 = \exp\left\{\frac{1}{k_6}(\dot{d}_A(t_2) - \max\{\dot{d}_A(t)\})\right\}$ and $\sigma_2 = \exp\left\{\frac{1}{k_6}(\dot{d}_A(t_2) - \min\{\dot{d}_A(t)\})\right\}$, showing that $d_A(t)$ converges exponentially to zero and by (2.29) so does $\dot{d}_A(t)$.

Proof of Item (2):

We have shown that $(d_A, \dot{d}_A) = (\eta_A^\top \zeta, -\eta_A^\top v)$ converges exponentially to zero. It remains to be proven that $(\zeta_\rho, v_\rho) = (\rho^\top \zeta, \rho^\top v)$ also converges to zero. From (2.26), it follows that

$$\begin{cases} \dot{\zeta}_\rho = -v_\rho \\ \dot{v}_\rho = -\dfrac{k_6}{d_A}(v_\rho - w_d \zeta_\rho). \end{cases}$$

Define a new state as $\delta = v_\rho - w_d \zeta_\rho$ and apply a coordinate transformation to obtain

$$\begin{cases} \dot{\zeta}_\rho = -w_d \zeta_\rho - \delta \\ \dot{\delta} = -(\dfrac{k_6}{d_A} - w_d)\delta + w_d^2 \zeta_\rho. \end{cases}$$

Then, consider a Lyapunov function

$$\mathcal{L}_6 = \frac{1}{2}\zeta_\rho^2 + \frac{1}{2w_d^2}\delta^2 \tag{2.30}$$

with time derivative given by

$$\dot{\mathcal{L}}_6 = -w_d\zeta_\rho^2 - \frac{1}{w_d^2}(\frac{k_6}{d_A} - w_d)\delta^2.$$

It follows that $\dot{\mathcal{L}}_6$ is negative definite, provided that $k_6 > w_d d_A(t) > 0$, which is equivalent to $0 < d_A(t) < \frac{k_6^2}{k_5}$. Since $d_A(t)$ is converging to zero from above, the condition will be satisfied after some finite time $T > 0$.

Given the division by d_A in the expression for $\dot{v}_\rho$, it is also important to show that it does not grow unbounded. This is equivalent to showing that $\frac{\delta}{d_A}$ is bounded. Let

$$\mathcal{L}_7 = \frac{1}{2}\left(\frac{\delta}{d_A}\right)^2$$

be a Lyapunov candidate, with time derivative

$$\dot{\mathcal{L}}_7 = -\frac{k_6 - w_d d_A + \dot{d}_A}{d_A}\left(\frac{\delta}{d_A}\right)^2 + w_d^2\frac{\delta}{d_A}\frac{\zeta_\rho}{d_A}.$$

Then, $\dot{\mathcal{L}}_7 < 0$ for

$$\left|\frac{\delta}{d_A}\right| > \frac{w_d}{k_6 - w_d d_A + \dot{d}_A}|\zeta_\rho|,$$

showing that $\left|\frac{\delta}{d_A}\right|$ cannot grow unbounded, given that the right-hand side of the condition is bounded.

Proof of item (3): This part of the proof is analogous to that of item *(1)* of the Theorem 2.1. Using the storage function defined in (2.17), it suffices to show that $\mathcal{S}(v_a) \leq V(1-\epsilon_a)$, with ϵ_a arbitrarily small, defines a positively invariant set.

The time derivative of $\mathcal{S}$ satisfies

$$\begin{aligned}\dot{\mathcal{S}} &= -\frac{k_6}{d_A(u_A^\top v_a)}(\|\pi_{u_A}v_a\|^2 - k_5 v_a^\top\pi_{u_A}v_w + \frac{k_5}{k_6}v_a^\top\pi_{u_A}\zeta_A)\\ &\leq -\frac{k_6\|\pi_{u_A}v_a\|}{d_A(u_A^\top v_a)}(\|\pi_{u_A}v_a\| - \varepsilon_w V - \frac{k_5}{k_6}\|\zeta_A\|).\end{aligned}$$

For the level set where $\mathcal{S} = V(1-\epsilon_a)$, we have $u_A^\top v_a = \epsilon_a V$ and $\|\pi_{u_A}v_a\| = V\sqrt{1-\epsilon_a^2}$. Then,

$$\dot{\mathcal{S}} \leq -\frac{k_6}{d_A\epsilon_a V}(V\sqrt{1-\epsilon_a^2} - \varepsilon_w V - \frac{k_5}{k_6}\|\zeta_A\|)$$

meaning that $u_A^\top v_a(t)$ will remain positive if the condition

$$\|\zeta_A(t)\| \leq \frac{k_6}{k_5}V(\sqrt{1-\epsilon_a^2} - \epsilon_w) \tag{2.31}$$

is satisfied. Next, we will show that (2.31) is satisfied under the initial conditions mentioned in Theorem 2.2. Recalling equations (2.27) and (2.30), equation (2.25) can be rewritten as

$$\mathcal{L}(t) = \mathcal{L}_6(t) + \max\{\lambda(t), d_A(t)\}^2.$$

Since $\dot{\mathcal{L}}_6$ is negative definite provided $0 < d_A < \frac{k_6^2}{k_5}$, as long as the initial condition (2.24) is satisfied, $\mathcal{L}(t)$ is decreasing, yielding

$$||\zeta_A(t)|| \le \sqrt{\mathcal{L}(t)} \le \min\{\frac{k_6^2}{k_5}, \frac{k_6}{k_5} V(\sqrt{1-\epsilon_a^2} - \epsilon_w)\}, \forall t \ge t_2.$$

□

2.5 Simulation Results

In this section, simulation results are shown to illustrate the behavior of the closed-loop system, using the landing controller on top of the high-gain inner-loop controller described in [SCH+15]. A fixed-wing aircraft (1/4 scale Extra-330) is considered ($m = 12$kg, $I = \text{diag}(1.4759, 2.8563, 4.119)$, $g = 10$ m/s^2). The gains of the proposed controllers have been chosen as follows: $k_1 = 15$, $k_2 = 30$ for the alignment phase, $k_3 = 30$, $k_4 = 60$ for the glide phase, and $k_5 = 25$, $k_6 = 35$ for the flare phase. The desired glide slope has been set to $\gamma^* = 6^o$ and the airspeed to $V = 15.5$ m/s. We use the pin-hole camera model with a focal length $f = 2.4$ mm. The initial conditions were set as follows $\zeta(0) = [0,\ 3,\ -18]$ m, ${}^Bv(0) = [15.3,\ 4,\ -1.2]$ m/s, $\beta(0) = 0$, $\alpha(0) = 0.1732$, $\mu(0) = 0$, $\gamma(0) = 0$, $\chi(0) = 0$, leading to an initial wind of $R(0)v_w(0) = [0,\ 4,\ 1.5]$ m/s, and finally $\Omega(0) = [0,\ 0,\ 0]$ s^{-1}.

In order to test robustness of the proposed control approach, the camera is set below the center of mass with an offset of 0.1m ($p_c = 0.1e_3$ m, in body-fixed frame) and a time varying wind velocity is introduced $R(t)v_w(t) = [0,\ 4,\ 1] + 0.5[0,\ \sin 0.2t,\ \cos 0.2t]$ m/s. It is straightforward to verify that ϵ_w in equation (2.1) can be fixed to 0.35.

Fig. 2.6 and Fig. 2.7 show that the aircraft lands smoothly on the center of runway and has a rate of descent sufficiently high to touchdown within the bounds of a 70 meter length runway. Figures 2.8 and 2.9 show the time evolution of aircraft's position and velocity, with the first, second, and third segments indicating the alignment, glide and flare phases, respectively. From Fig. 2.8, we can see that the aircraft converges to the desired path, even with the presence of unmodelled dynamic perturbations and camera offset. Fig. 2.10 shows the virtual force input generated by the proposed outer-loop control law, which defines the reference for the inner-loop controller.

The states controlled by the inner-loop controller are shown in Figs. 2.11 and 2.12. The time evolution of the side-slip angle β, angle of attack α, and bank angle μ during the three phases is presented in Fig. 2.11, whereas Fig. 2.12 shows the time evolution of Euler angles. Figures 2.11 and 2.12 indicate a good compromise in terms of time-scale separation between the outer-loop and inner-loop controllers, showing that the inner-loop controller is sufficiently fast to track the outer-loop references, including during the transitions between stages.

The effective simulation results show that as long as some care is taken in choosing the guidance control gains to ensure that the desired orientation set point is small enough, the robustness of the proposed algorithm leads to an effective closed-loop performance even in the presence of unmodelled dynamic perturbations and camera offset.

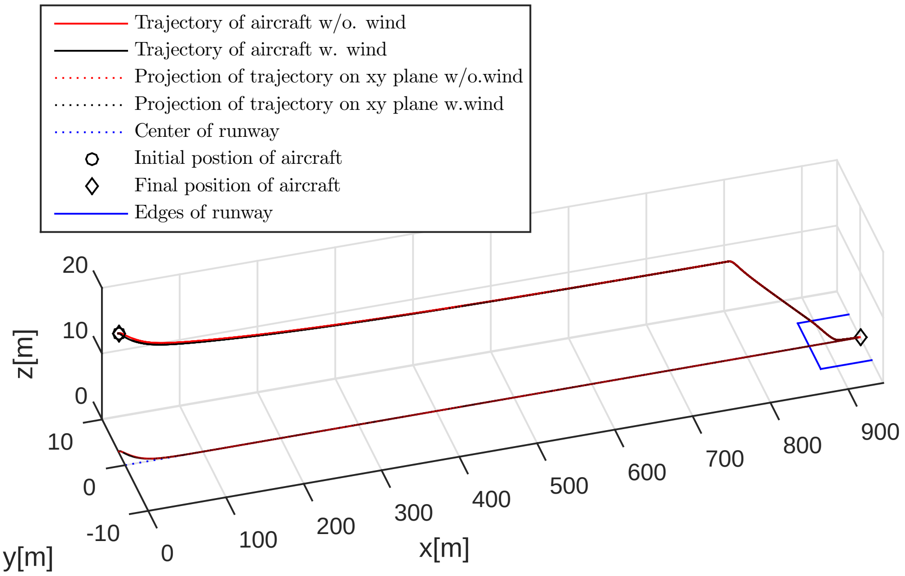

Figure 2.6: 3-D plot of the aircraft trajectory.

2.6 Conclusion

This chapter proposed a 2D image-based controller to steer a fixed-wing UAV during the first three stages of landing. The image features of the runway are exploited to achieve horizontal alignment and smooth touchdown of the aircraft on the runway during alignment, glide-slope, and flare phases. Using optical flow for the velocity-like term eliminates the need for including a crosswind estimator and considerably simplifies the control laws. A formal proof of convergence of the separate control scheme is provided and the simulation results show the effectiveness of the proposed control algorithm.

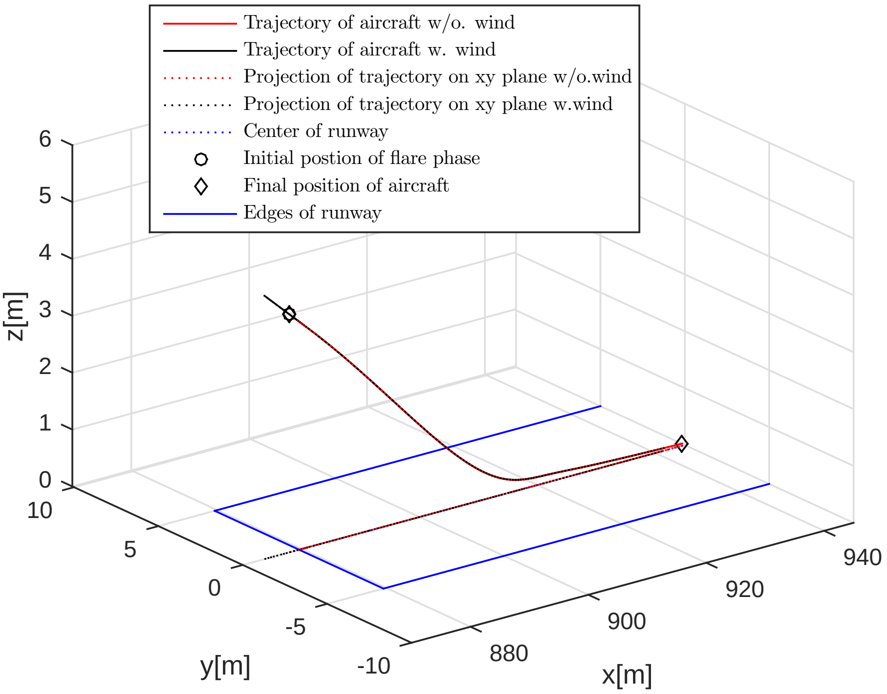

Figure 2.7: 3-D plot of flare phase.

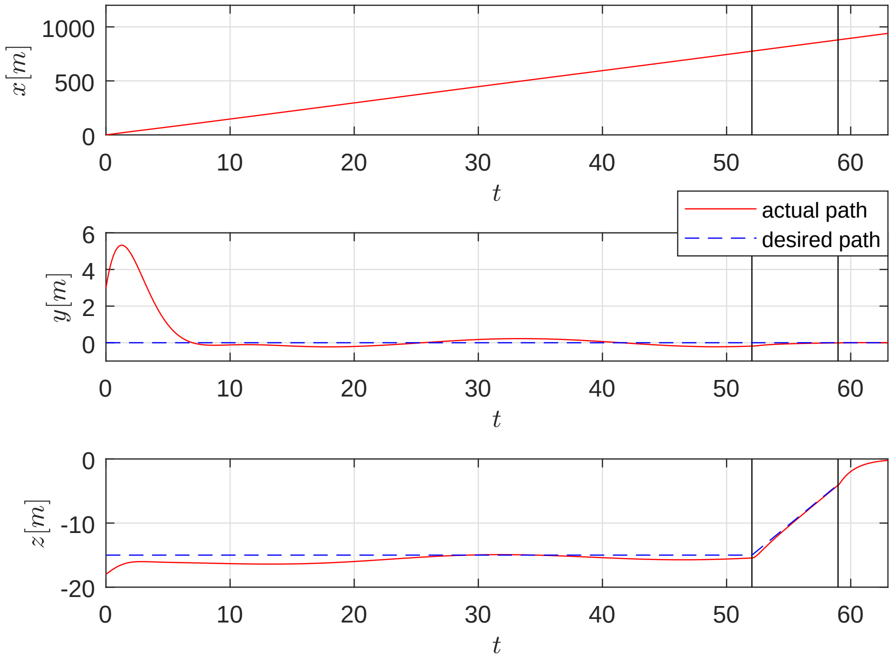

Figure 2.8: Aircraft position.

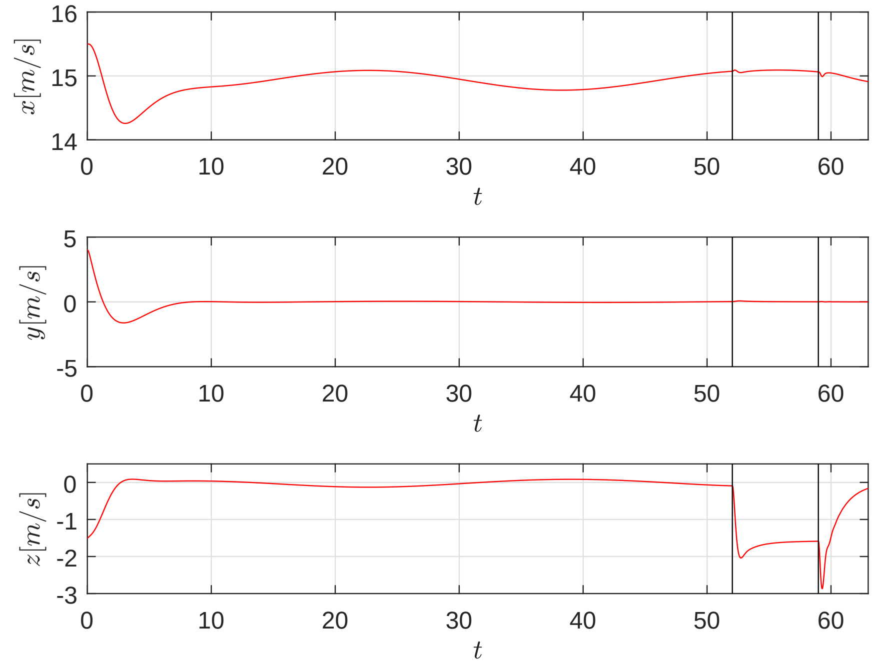

Figure 2.9: Aircraft velocity.

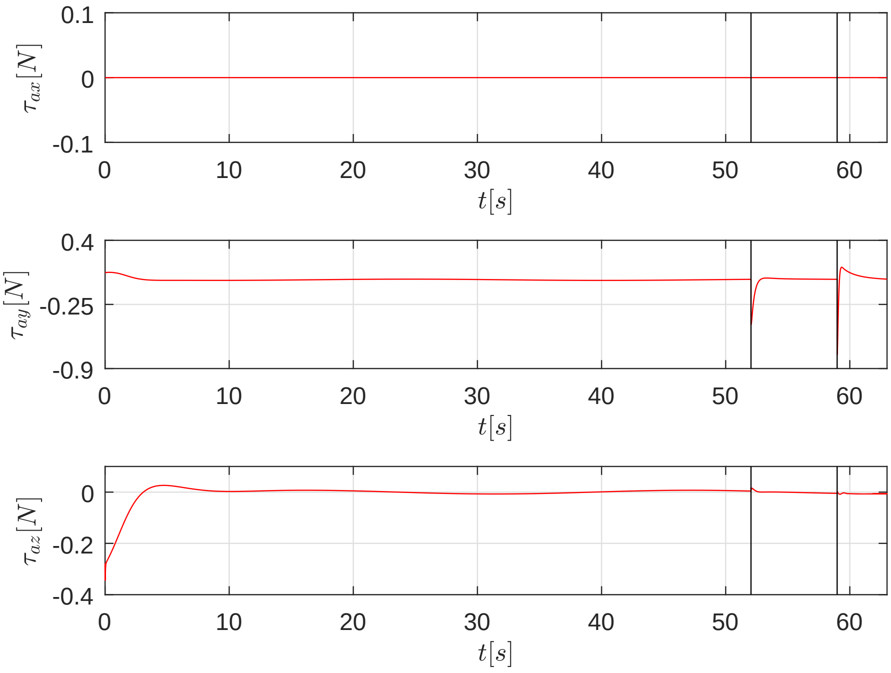

Figure 2.10: Virtual force input τ_a expressed in $\{\mathcal{I}\}$.

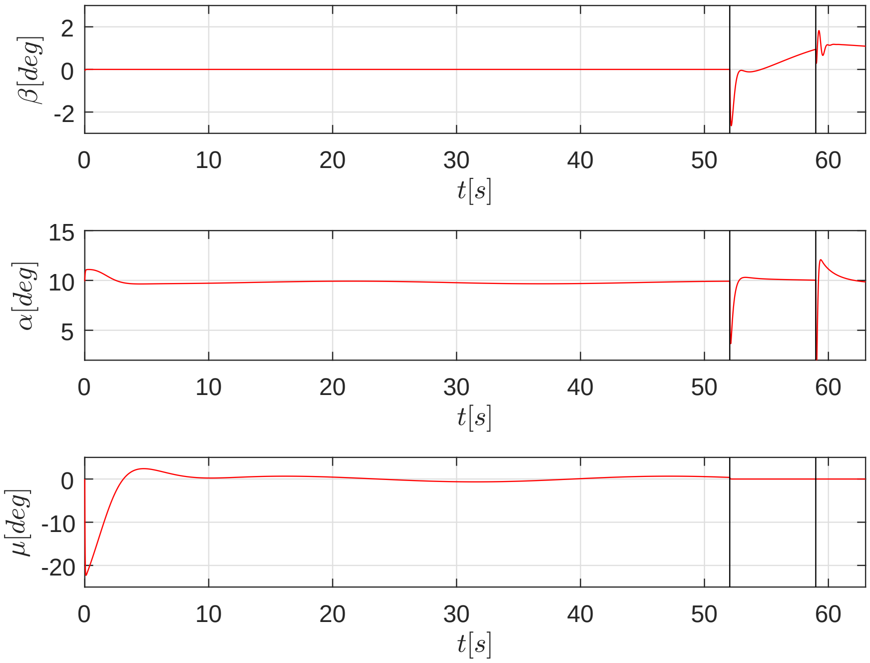

Figure 2.11: Angle of attack α, side-slip β and bank angle μ.

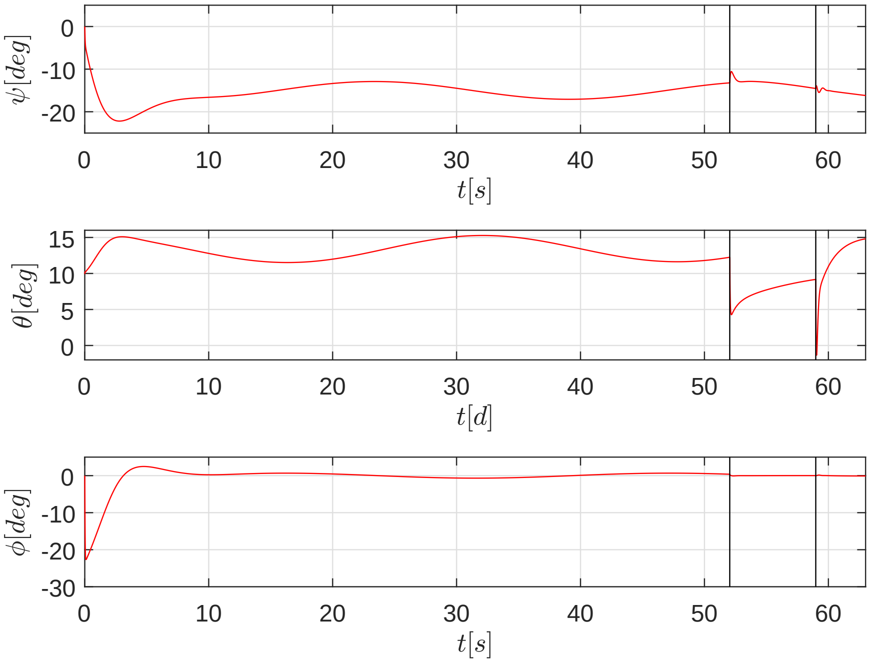

Figure 2.12: Euler angles: yaw ψ, pitch θ, and roll ϕ.

3

QUADROTOR GOING THROUGH A WINDOW AND LANDING: AN IMAGE-BASED VISUAL SERVO CONTROL APPROACH

3.1 Introduction

In this chapter, we extend the IBVS control solution based on spherical image centroids to a specific problem of steering a quadrotor to move from one room to a second one by crossing a window and then land on a planar target placed in the second room (see Fig. 3.1). This application has significant practical interest since many tasks (i.e. search and rescue in an earthquake-damaged building [MSM+12], package delivery using UAVs) require UAVs to land on a final destination or to perform intermediate landings for battery recharge or exchange, or refueling (for larger UAVs) during long missions. The quadrotor is assumed to be equipped with an IMU and two on-board cameras: one forward-looking and another downward-looking. Neither the translational velocity and position of the vehicle nor the location of the target (window and landing pad) are known. In the proposed IBVS control laws, the centroid vectors provided by the combination of the spherical image measurements of a collection of landmarks (corners) from both the window and the landing pad are used as position cue and the translational optical flow relative to the plane containing window and landing pad is used as velocity cue.

The control law proposed for going through the window draws inspiration from [SCH+16], but considers a different objective. Instead of landing and ensuring an always positive height, the control law ensures that no collision with the wall or windows edges will occur and the vehicle will align with the center line orthogonal to the window, crossing it with non-zero velocity. The control law for landing on the target is an improvement with respect to the one used in [SCH+16], with the centroid vector now directly given by the image centroid, which is highly robust to pixel noise, and easily computed in real-time in the camera frame and then derotated.

This chapter presents the following novel contributions: 1) bounded disturbances (i.e. due

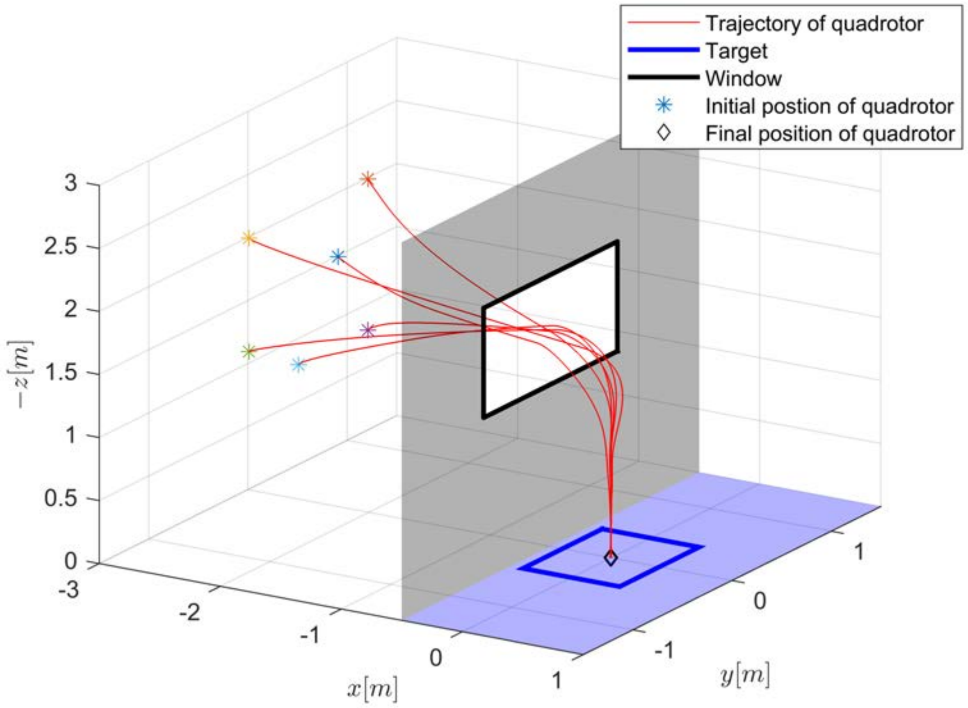

Figure 3.1: 3-D plot of the quadrotor trajectory.

to wind, and unmodeled dynamics) are included in the dynamics of the system; 2) a complete stability analysis shows that convergence to the desired zero-height equilibrium is guaranteed in all cases and ultimate boundedness of the horizontal position error is guaranteed when landing in the presence of horizontal disturbances; 3) experimental results are provided where the controllers run on an onboard computer together with the image processing for the detection of window and landing pad and for the computation of the translational optical flow.

The chapter consists of seven parts. Section 3.2 presents the dynamic model and the fundamental equations of motion. Section 3.3 introduces the environment and presents the image features that are used in the control law. Section 3.4 proposes two control laws: one for the landing task in obstacle-free environments and the other for flying through the window. A combination of these two control laws in the practical case is also presented in this section. Section 3.5 shows simulation results obtained with the proposed controller. Section 3.6 presents and analyzes the experimental results which validate the proposed controllers. The chapter concludes with some final comments in Section 3.7.

3.1.1 Related work

There are several examples in the literature of recent work dedicated to the problem of flying autonomous vehicles in complex environment using vision systems. In [LBMK17, FMFS17, GL20], the authors specifically address the problem of going through a window using only a single camera and an IMU. However, estimation of vehicle's position and velocity is required in [LBMK17, FMFS17]. Besides, the pose of the window is assumed to be known in [LBMK17]. Although the work in [GL20] directly uses image feature as position cue, estimates of the image depth are still required and the velocity vector is assumed to be known. In general, state estimation adds computational complexity, and the output is often sensitive to image noise and camera calibration errors. The limited work on image-based control approach can be explained by the complexity involved in obtaining sound proofs of convergence and stability.

Landing in complex environments calls for obstacle avoidance capabilities, which are naturally provided by the use of optical flow, a visual feature that draws inspiration from flying insects. Based on [MCH08] and using optical flow, the authors proposed IBVS controllers for landing a quadrotor [HHMR12, SCH⁺16] and landing a fixed-wing aircraft [LBHM⁺14, SCH⁺15] eliminating the need to estimate the height of the vehicle above the ground . Using a distinct paradigm, a novel setup of self-supervised learning based on optical flow was introduced in [HDWRDC18]. Using optical flow, the proposed method learns the visual appearance of obstacles in order to search for a landing spot for micro aerial vehicles.

When compared to related work, this chapter proposes simple IBVS controllers applied in sequence to first go through a window and then land on a planar target, using only vision measurements and requiring no estimation of position, velocity, image depth, nor height above the target. The present work also provides rigorous mathematical proofs for stability and robustness in the presence of disturbances, complemented by experimental validation of the proposed controllers.

3.2 Quadrotor modeling and control architecture

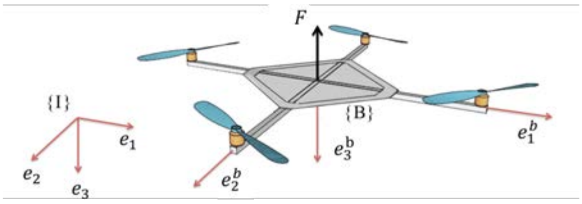

Figure 3.2: Target plane and window plane.

Consider a quadrotor UAV equipped with an IMU and two cameras. To describe the motion of the quadrotor, two reference frames are introduced: an inertial reference frame $\{I\}$ fixed to the earth surface and a body-fixed frame $\{B\}$ attached to the quadrotor's centre of mass (see Fig. 3.2). Let $R = {}^{B}_{I}\mathbf{R} \in SO(3)$ denote the orientation of the frame $\{B\}$ with respect to $\{I\}$ and let $\xi \in \mathbb{R}^3$ be the position of the origin of the frame $\{B\}$ with respect to $\{I\}$. Let $v \in \mathbb{R}^3$ denote the translational velocity expressed in $\{I\}$ and $\Omega \in \mathbb{R}^3$ the orientation velocity expressed in $\{B\}$. The

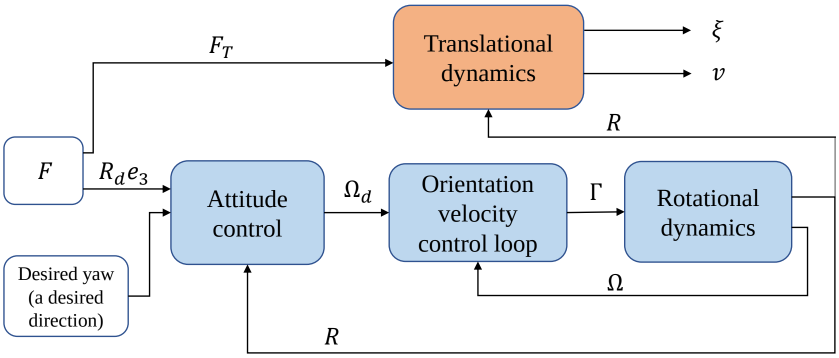

Figure 3.3: A hierarchical control design strategy.

kinematics and dynamics of the quadrotor vehicle are then described as

$$\begin{cases} \dot{\xi} = v \\ m\dot{v} = -F + mge_3 + \triangle \end{cases} \tag{3.1}$$

$$\begin{cases} \dot{R} = RS(\Omega) \\ \boldsymbol{I}\dot{\Omega} = -\Omega_{\times}\boldsymbol{I}\Omega + \Gamma \end{cases} \tag{3.2}$$

The vector $F \in \mathbb{R}^3$ expressed in $\{I\}$ combines the principal non-conservative forces applied to the quadrotor and generated by the four rotors. In quasi-hover conditions one can reasonably assume that this aerodynamic force is always in the direction e_3^b in $\{B\}$, since all the four thrusters are aligned with e_3^b and their contribution predominates over other components. Thus the F in the direction of e_3^b expressed in the inertial frame can be described as follows:

$$F = F_T R e_3 \tag{3.3}$$

where the scalar F_T represents the total thrust magnitude generated by the four motors. It also represents the unique control input for the translational dynamics.

The term $\triangle$ combines the modelling errors and aerodynamic effects due to the interaction of the rotors wake with the environment causing random wind and dynamic inflow effects [PH88].

The vector $\Gamma \in \mathbb{R}^3$ expressed in $\{B\}$ is the torque control for the attitude dynamics. It is obtained via the combination of the contributions of four rotors. The invertible linear map between $[F_T \in \mathbb{R}^+, \Gamma \in \mathbb{R}^3]$ and the collection of individual thrusters $[F_{T_1}, F_{T_2}, F_{T_3}, F_{T_4}]$ can be found in [HMLO02].

3.2.1 Control architecture

A hierarchical control design strategy is adopted in this chapter (see Fig. 3.3). This choice is motivated by the natural structure of the system dynamics and its practical implementation [BGH+11, HHMR12]. For the translational dynamics of the quadrotor (3.1), the force F (3.3)

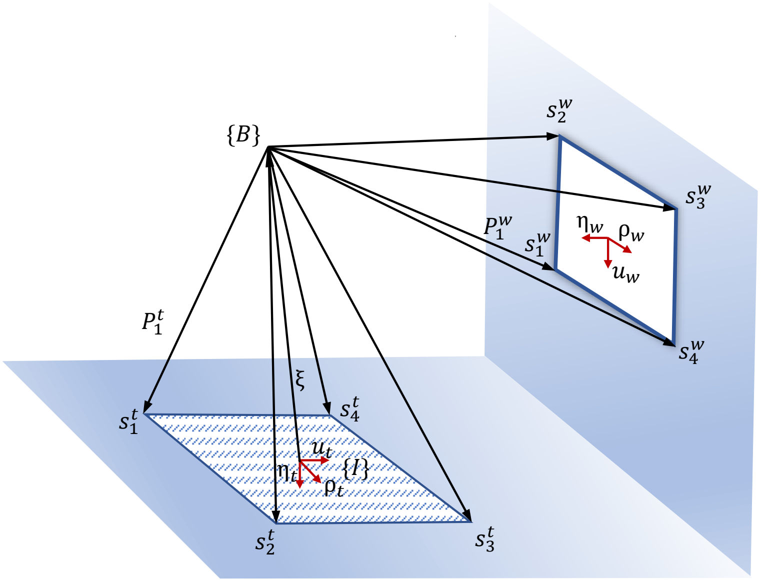

Figure 3.4: Target plane and window plane.

is used as control input by means of its thrust direction and its magnitude. This constitutes a high-level outer loop for the control design. The thrust F_T is directly the magnitude of the designed force ($F_T = ||F||$) and the desired attitude R_d (partly obtained by the desired direction $R_d e_3 = \frac{F}{||F||}$ complemented by a desired yaw) can then be reached by considering the body's angular velocity Ω as an intermediary control input, which constitutes again a desired angular velocity for the fully actuated orientation dynamics (3.2) via the high gain control torque Γ. The stabilisation of the orientation dynamics is not the subject of this paper and we assume that a suitable low level robust stabilising control is implemented, that satisfactorily regulates the attitude error with a fast dynamics.

3.3 Environment and Image Features

In this section adequate image features in relation to the considered tasks are derived and all required assumptions regarding the environment and the setup are established.

Assumption 3.1. *A downward -looking camera and a forward-looking camera are attached to the center of mass of the vehicle. The downward-looking camera reference frame coincides with the body-fixed frame {B}. The rotation matrix from the forward-looking camera reference frame to the body frame* ${}^{B}_{c}\mathbf{R} \in SO(3)$ *is known.*

Assumption 3.2. *The angular velocity* Ω *is measured and the orientation matrix* R *of* {B} *with respect to* {I} *is obtained by external observer-based IMU measurements. This allows to represent all image information and the system dynamics in the inertial frame.*

Assumption 3.3. *The landing target lies on a textured plane which is called target plane. Its normal direction* $\eta_t \in \mathbb{S}^2$ *in the inertial frame is known (typically* $\eta_t \approx e_3$*).*

Assumption 3.4. *The target window has a rectangle shape and lies on a textured wall which is called window plane. Its width* r_w *is known and but its normal direction* $\eta_w \in \mathbb{S}^2$ *is unknown.*

Both landing plane and window plane are placed in the environment, as shown in Figure 3.4. It assumed that the vehicle is able to recognize the landing pad and the window from landmarks on the pad and from corners and edges of the window respectively. The background texture on both landing plane and window plane are also exploited to obtain information about the vehicle's velocity with respect to the planes and also to avoid collisions with the wall and the window's edges.

For any initial position (along with any initial velocity) outside the room containing the landing pad, the main objective is to design a feedback controller resorting only to image features that can ensure automatic landing of the vehicle without any collision.

3.3.1 Image features on the landing plane

The target on the landing plane is depicted in Figure 3.4. The axes of $\{\mathcal{I}\}$ are given by (u_t, ρ_t, η_t), where $\rho_t = \eta_t \times u_t$, and the origin of $\{\mathcal{I}\}$ is placed at the center of the landing pad. As shown in Figure 3.4, $s_i^t \in \mathbb{R}^3$ denotes the position of ith marker (or a corner) of the landing pad relative to the inertial frame expressed in $\{\mathcal{I}\}$. Note that $\eta_t^\top s_i^t = 0$. Define the position vector of ith marker of the target relative to $\{B\}$ as

$$P_i^t = s_i^t - \xi.$$

The position of the vehicle relative to the center of the landing pad is defined as

$$\xi_t = -\frac{1}{n_t}\sum_{i=1}^{n_t} P_i^t = \xi - \frac{1}{n_t}\sum_{i=1}^{n_t} s_i^t$$

where n_t is the number of observed markers on the landing pad and $\frac{1}{n_t}\sum_{i=1}^{n_t} s_i^t$ is a constant vector. This sum is zero when all markers are in the camera field of view.

Using the spherical projection model for a calibrated camera, the spherical image points of landing pad's markers can be expressed as

$$p_i^t = \frac{P_i^t}{||P_i^t||} = \frac{s_i^t - \xi}{||s_i^t - \xi||}$$

which can be obtained from the 2D pixel locations of the camera image as stated in Section A.1 in the appendix.

The visual feature used for the landing task is the the centroid of the observed visual feature

$$q_t := -\frac{1}{n_t}\sum_{i=1}^{n_t} p_i^t,$$

whose properties of can be found in Section A.2 in the appendix.

3.3.2 Image features on the window plane

As shown in the Figure 3.4, a rectangular window is placed on a textured wall. Its corners and edges are assumed to be recognised in camera images. Both information are combined together to extract the normal direction η_w and provide the feedback information used in the controller.

Consider first the the windows corners and let $s_i^w \in \mathbb{R}^3$ denote the position of ith corner of the window expressed in $\{\mathcal{I}\}$. Define the position vector of ith corner of the window relative to $\{B\}$ as

$$P_i^w = s_i^w - \xi. \tag{3.4}$$

From there, one can deduce the position of the vehicle with respect to the window's center:

$$\xi_w = -\frac{1}{n_w}\sum_{i=1}^{n_w} P_i^w = \xi - \frac{1}{n_w}\sum_{i=1}^{n_w} s_i^w,$$

with n_w (typically $n_w = 4$) number of the window's corners and $\frac{1}{n_w}\sum_{i=1}^{n_w} s_i^w$ constant vector.

Similarly to Section 3.3.1, the spherical image points of the corners of the window are exploited:

$$p_i^w = \frac{P_i^w}{\|P_i^w\|}$$

leading the following centroid:

$$q_w(t) := -\frac{1}{n_w}\sum_{i=1}^{n_w} p_i^w(t). \tag{3.5}$$

Now, to extract the normal direction η_w, recall that the axes representing the window are given by (η_w, ρ_w, u_w), with $\rho_w = u_w \times \eta_w$ (see Figure 3.5). Using the image of ith line and exploiting the fact that the window has a rectangular shape, it is straightforward to get the directions u_w and ρ_w and consequently η_w. Using the result from Section A.3 and the fact that lines 1 and 3 (resp. lines 2 and 4) are parallel in the inertial frame, one deduces the measure of the direction u_w (resp. ρ_w) from the following relationships:

$$\begin{aligned}\rho_w &= \pm\frac{h_1 \times h_3}{\|h_1 \times h_3\|}\\ u_w &= \pm\frac{h_2 \times h_4}{\|h_2 \times h_4\|}.\end{aligned}$$

where h_i is normal to the plane defined by the origin of the camera/body-fixed frame and the ith line. Then the normal vector to the window plane is directly obtained by

$$\eta_w = \pm\frac{u_w \times \rho_w}{\|u_w \times \rho_w\|} \tag{3.6}$$

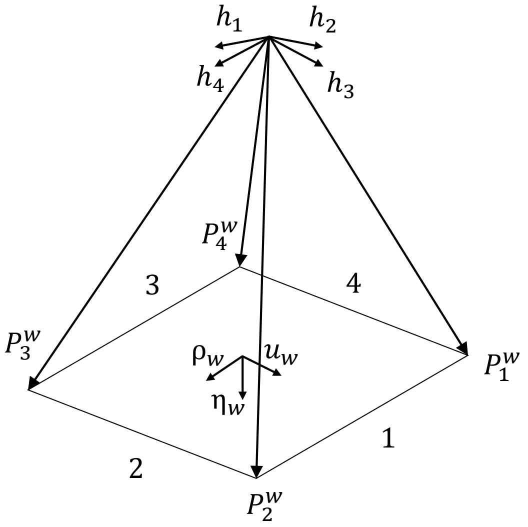

Figure 3.5: Window plane and unit directions h_i normal to the planes defined by the origin of camera frame and the ith window edges .

and the sign of equation (3.6) is chosen such that the condition $\eta_w^\top q_w(0) < 0$, with $q_w(t)$ the image centroid of window's corners (3.5).

To exploit the image of window's edges, we define the vector from the vehicle to the closest point on window's edges as $L^e \in \mathbb{R}^3$, its direction $l^e = \frac{L^e}{\|L^e\|}$ can be obtained from the camera

$$l^e = \{l_i^e : \max\{|\eta_w^\top l_i^e|\}, i = \{1,2,3,4\}\}$$

where

$$l_i^e = \pm(h_i \times \rho_w), i = \{1,3\}, \;\; l_i^e = \pm(h_i \times u_w), i = \{2,4\}$$

are the directions from the vehicle to the nearest point on each edge i.

Form now on, we are able to derive the required information achieving the double goal of going through the window in the meanwhile avoiding collision with the window edges and wall. We first define the safety region $\mathcal{M}$ such that

$$\mathcal{M} := \{\xi_w : \|q_w(\xi_w)\| \leq \epsilon\},$$

where $\epsilon > 0$ is chosen such that $\forall \xi_w \in \mathcal{M}$, the condition $\|\xi_w\| < \frac{r_w}{2} - \epsilon$ also holds, implying that the region $\mathcal{M}$ does not contain the window edges (see Fig. 3.6). From there, the chosen visual feature that encodes all required information about the position of the vehicle with respect to the window is:

$$\bar{q}_w := -\frac{1}{n_w}\sum_{i=1}^{n_w} p_i^w \left[\alpha_w(t)\frac{1}{\eta_w^\top p_i^w} + (1-\alpha_w(t))\frac{\eta_w^\top l_e}{\eta_w^\top p_i^w}\right], \tag{3.7}$$

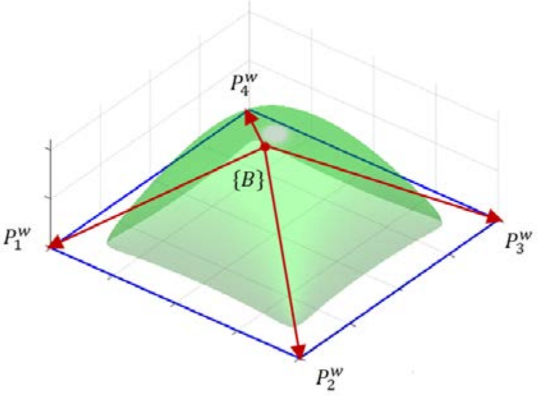

Figure 3.6: The green volume represents the region $\mathcal{M}$ which excludes the window edges.

where $\alpha_w(\|q_w(\xi_w)\|)$ is a weight function ensuring the continuity of $\bar{q}_w$. It is defined as follows:

$$\alpha_w(\|q_w(\xi_w)\|) = \begin{cases} 0 & \text{, if } \|q_w\| \leq \epsilon \ (\xi_w \in \mathcal{M}) \\ \frac{1}{\delta}(\|q_w\| - \epsilon), & \text{, if } \epsilon < \|q_w\| < \epsilon + \delta \\ 1 & \text{, if } \|q_w\| \geq \epsilon + \delta, \end{cases} \tag{3.8}$$

with δ an arbitrary small positive constant. Since $\eta_w^\top l^e = \frac{\eta_w^\top L^e}{\|L^e\|} = \frac{\eta_w^\top P_i^w}{\|L^e\|}$, $\bar{q}_w$ can be expressed in terms of the unknown distance d_o and d_e:

$$\bar{q}_w(t) = \alpha_w(t)\frac{\xi_w(t)}{d_o(t)} + (1 - \alpha_w(t))\frac{\xi_w(t)}{d_e(t)} \tag{3.9}$$

where $d_o := \eta_w^\top P_i^w = -\eta_w^\top \xi_w$ is the distance from the camera to the wall and $d_e := \|L^e\| = \sqrt{d_o^2 + \|\pi_{\eta_w} L^e\|^2}$ represents the distance from the camera to the closest window's edge.

3.3.3 Image Kinematics and Translational Optical Flow

The kinematics of any observed points on the landing plane (including markers of the the landing pad) can be written as:

$$\dot{P}^t = -\dot{\xi} = -v$$

where P^t expressed in $\{\mathcal{I}\}$ denotes any point on the textured ground of the landing plane. So the kinematics of the corresponding image point $p^t = \frac{P^t}{\|P^t\|}$ can be expressed as

$$\dot{p}^t = -\pi_{p^t}\frac{v}{\|P^t\|}. \tag{3.10}$$

Let d_t be the height of the vehicle above the landing plane:

$$d_t := \eta_t^\top P^t = \eta_t^\top P_i^t = -\eta_t^\top \xi_t,$$

then equation (3.10) can be rewritten as

$$\dot{p}^t = -\cos\theta^t \pi_{p^t} W_t(t)$$

where $\cos\theta^t = \frac{d_t}{\|P^t\|} = \eta_t^\top p^t$ and W_t is the translational optical flow:

$$W_t(t) = \frac{v(t)}{d_t(t)}.$$

It is the ideal image velocity cue that can be complemented with the centroid information for designing a pure IBVS controller to perform the landing task. According to Section A.4, W_t can be obtained from the integral of $\dot{p}^t$ along direction η_t over a solid angle.

Similarly, the kinematics of any observed points on the window plane can be written in the inertial frame as

$$\dot{P}^w = -v$$

where P^w expressed in $\{\mathcal{I}\}$ denotes the position of a point on the textured wall of the window plane with respect to $\{B\}$ expressed in $\{I\}$, not to be confused with P_i^w (3.4), which is the position of the ith corner of the window with respect to $\{B\}$ and also expressed in $\{I\}$. So the kinematics of the corresponding image point $p^w = \frac{P^w}{\|P^w\|}$ can be written as

$$\dot{p}^w = -\cos\theta^w \pi_{p^w} \frac{v}{d_o}$$

with $\cos\theta^w = \frac{d_o}{\|P^w\|} = \eta_w^\top p^w$. Analogously to the previous case, the translational optical flow with respect to the textured wall, $\frac{v}{d_o}$, can be obtained from the integral of $\dot{p}^w$ along the direction η_w over a solid angle.

Now, to achieve the goal that the vehicle is going through the window smoothly, the translational optical flow with respect to the closest window's edge is also used. The kinematics of any observed points on the closest window's edge is

$$\dot{P}^e = -v$$

where P^e denotes the position of a point on the the closest edge from the window. The kinematics of the corresponding image point $p^e = \frac{P^e}{\|P^e\|}$ can be written as

$$\dot{p}^e = -\cos\theta^e \pi_{l^e} \frac{v}{d_e}$$

with $\cos\theta^e = \frac{d_e}{\|P^e\|} = l^{e\top} p^e$. The translational optical flow with respect to the closest window edge, $\frac{v}{d_e}$, can be obtained from the integral of $\dot{p}^e$ along the direction l^e over a solid angle.

Analogously to (3.7), the translational optical flow used for going through the window is the convex combination of the translational optical flow with respect to the textured wall and to the closest window edge, respectively:

$$W_w = \alpha_w(t)\frac{v(t)}{d_o(t)} + (1-\alpha_w(t))\frac{v(t)}{d_e(t)} \tag{3.11}$$

with $\alpha_w(t)$ defined already by (3.8).

3.4 Controller design

3.4.1 Landing in obstacle free environment

Theorem 3.1. *Consider the system (3.1) in the nominal case ($\triangle \equiv 0$) subjected to the following feedback control:*

$$F_t = K_p^t q_t + K_d^t W_t + mge_3. \tag{3.12}$$

with $K_p^t = k_{p_{1,2}}^t \pi_{\eta_t} + k_{p_3}^t \eta_t \eta_t^\top$ and $K_d^t = k_{d_{1,2}}^t \pi_{\eta_t} + k_{d_3}^t \eta_t \eta_t^\top$ two constant positive definite matrices. If for any initial condition such that $d_t(0) = -\eta_t^\top \xi_t(0) \in \mathbb{R}^+$, then the following assertions hold $\forall t \geq 0$:
1) the height $d_t(t) = -\eta_t^\top \xi_t(t) \in \mathbb{R}^+$ and its derivative $\dot{d}_t(t) \in \mathbb{R}$ are well defined and uniformly bounded $\forall t$ and converge to zero asymptotically,
2) the acceleration $\dot{v}(t)$ and the states $(\xi_t(t), v(t))$ are bounded and converge asymptotically to zero.

Proof. The proof follows a reasoning very similar to that of Theorem 1 in [RHMS14]. Recalling (3.1) and applying the control input (3.12), we can write the closed-loop system as

$$\begin{cases} \dot{\xi}_t = v \\ \dot{v} = -K_p^t q_t(\xi_t) - K_d^t \dfrac{v}{d_t}. \end{cases} \tag{3.13}$$

Before proceeding with the proof of item 1), we define a positive definite storage function $\mathcal{L}_2(\xi_t, v)$ and show that if $d_t(t)$ remains positive, $\dot{\mathcal{L}}_2$ is negative semi-definite, which implies that the solutions remain bounded for all $t \geq 0$. Define $\mathcal{L}_2$ as

$$\mathcal{L}_2(\xi_t, v) = \mathcal{L}_1(\xi_t) + \frac{1}{2} v^\top K_p^{t^{-1}} v$$

where $\mathcal{L}_1(\xi_t)$ is the radially unbounded function given by

$$\mathcal{L}_1(\xi_t) = \frac{1}{n_t} \sum_{i=1}^{n_t} (\|P_i^t(\xi_t)\| - \|P_i^t(0)\|).$$

By a direct application of Lemma A.2 in the appendix, we conclude that $\mathcal{L}_1(\xi_t)$ is a positive definite function with

$$\frac{\partial \mathcal{L}_1}{\partial \xi_t} = q_t^\top$$
$$\frac{\partial^2 \mathcal{L}_1}{\partial \xi_t^2} = Q$$

where $Q = \frac{1}{n_t} \sum_{i=1}^{n_t} \frac{1}{\|P_i^t\|} \pi_{p_i^t}$ is positive definite, as long as at least two of the vectors p_i^t are non-collinear. Noting that,

$$\dot{\mathcal{L}}_1 = q_t^\top v, \tag{3.14}$$

it follows that

$$\dot{\mathcal{L}}_2 = -\frac{1}{d_t} v^\top K_p^{t^{-1}} K_d^t v \tag{3.15}$$

which is negative semi-definite as long as d_t remains positive and implies that the states $\xi_t(t)$ and $v(t)$ remain bounded for all $t \geq 0$. The next steps of the proof consist in proving first Item (1) and then the uniform continuity of (3.15) along every system's solution in order to deduce, by application of Barbalat's Lemma, the asymptotic convergence of v to zero and from there we deduce the asymptotic convergence of $\dot{v}$ and then ξ_t to zero (Item 2).

Proof of Item 1: Using (3.13) and the fact that $d_t(t) = -\eta_t^\top \xi_t$ and $\dot{d}_t = -\eta_t{}^\top v$ yields

$$\ddot{d}_t = -k_{d_3}^t \frac{\dot{d}_t}{d_t} - k_{p_3}^t \beta_t \tag{3.16}$$

with

$$\beta_t(t) = -\eta_t^\top q_t = \tfrac{1}{n_t} \textstyle\sum_{i=1}^{n_t} \tfrac{d_t}{\|P_t^i\|} > 0, \ \forall t. \tag{3.17}$$

This relation is of course valid as long as $d_t(t) > 0$. From there, direct application of [RHMS14, Th. 1-(2)] shows that if $d_t(0) \in \mathbb{R}^+$, the solution $(d_t, \dot{d}_t) \in (\mathbb{R}^+, \mathbb{R})$ exists and uniformly bounded $\forall t$ and converges asymptotically to $(0, 0)$.

Proof of Item 2: To show that

$$\ddot{\mathcal{L}}_2 = -\frac{2}{d_t} v^\top K_p^{t^{-1}} K_d^t \dot{v} + \frac{\dot{d}_t}{d_t}\frac{1}{d_t} v^\top K_p^{t^{-1}} K_d^t v$$

is bounded and hence $\dot{\mathcal{L}}_2$ (3.15) is uniformly continuous, it suffices to show that $\frac{\|v\|}{d_t}$ is bounded (so is $\frac{\dot{d}_t}{d_t}$). For that purposes, consider the dynamics of $\frac{v}{d_t}$:

$$\frac{d}{dt}\left(\frac{v}{d_t}\right) = -\frac{1}{d_t}\left((K_d^t + \dot{d}_t I_3)\frac{v}{d_t} + K_p^t q_t\right). \tag{3.18}$$

Since $\dot{d}_t$ converges asymptotically to zero and q_t is bounded then, by direct application of [RHMS14, Lemma 4] one ensures that $\frac{v}{d_t}$ is bounded. From there one concludes that $\dot{\mathcal{L}}_2$ is uniformly continuous and hence v converges asymptotically to zero.

To prove that $q_t(t)$ (or equivalently ξ_t) is asymptotically converging to zero we have to show first $\dot{v}$ is converging to zero. From (3.13), one can verify that:

$$\ddot{v} = -\frac{K_d^t}{d_t}\dot{v} + \delta_{\dot{v}}^0, \tag{3.19}$$

with $\delta_{\dot{v}}^0 = K_d^t \frac{\dot{d}_t}{d_t}\frac{v}{d_t} - K_p^t \dot{q}_t$. Since $\frac{v}{d_t}$ (and hence $\frac{\dot{d}_t}{d_t}$) is bounded and

$$\dot{q}_t = Qv = Q_0 \frac{v}{d_t}, \text{ with } Q_0 = \frac{1}{n_t}\sum_{i=1}^{n_t} \frac{d_t}{\|P_i^t\|}\pi_{p_i^t} < I_3,$$

is also a bounded vector, one ensures that $\delta_{\dot{v}}^{0}$ is bounded. Therefore, direct application of [RHMS14, Lem. 3] concludes boundedness and the asymptotic convergence of $\dot{v}$ to zero and hence one has:

$$\frac{v}{d_t} = -{K_d^{t}}^{-1} K_p^t q_t + o(t)$$

with $o(t)$ a asymptotically vanishing term.

By multiplying both sides of the above equation by the bounded vector $q_t^\top$ (the gradient of $\mathcal{L}_1$) and using the fact that $\dot{\mathcal{L}}_1 = q_t^\top v$ (3.14), one obtains:

$$\dot{\mathcal{L}}_1 = -d_t q_t^\top {K_d^{t}}^{-1} K_p^t q_t + d_t q_t^\top o(t). \tag{3.20}$$

Since $d_t(t)$ converges asymptotically to zero, then by taking the integral of (3.16)

$$\dot{d}_t(t) - \dot{d}_t(0) = -k_{d3}^t \log(\frac{d_t(t)}{d_t(0)}) - k_{p3}^t \int_0^t \beta_t(\tau) d\tau,$$

one concludes that

$$\lim_{t \to \infty} \int_0^t \beta_t(\tau) d\tau = +\infty. \tag{3.21}$$

Combining equation (3.21) with the fact that $d(t) \geq \beta_t(t)$ (from (3.17)) and replacing the time index t of equation (3.20) by the new time-scale index $s(t) := \int_0^t d_t(\tau) d\tau$ (s tends to infinity if and only if t tends to infinity), one has:

$$\frac{d}{ds}\mathcal{L}_1 = -q_t^\top {K_d^{t}}^{-1} K_p^t q_t + q_t^\top o(t),$$

from which we conclude that q_t (and ξ_t) is asymptotically converging to zero. □

Proposition 3.1. *Consider the system (3.1) in which $\triangle$ and $\dot{\triangle}$ are bounded.*
1) If the perturbation $\triangle$ is such that:

$$\triangle = \pi_{\eta_t} \triangle, \text{ or equivalently } \eta_t^\top \triangle(t) = 0, \ \forall t \geq 0,$$

then, for any initial condition such that $d_t(0) = -\eta_t^\top \xi_t(0) \in \mathbb{R}^+$, direct application of the feedback control (3.12), ensures that: i) Item 1 of Theorem 3.1 holds, ii) $\dot{v}(t)$ and $v(t)$ are bounded and converging asymptotically to zero, and finally iii) $\|\pi_{\eta_t} \xi_t\|$ is ultimately bounded by Δ_ξ, solution of $\|\pi_{\eta_t} q_t\| = \frac{\|\triangle\|_{\max}}{k_{d_{1,2}}^t}$.
2) If $\eta_t^\top \triangle(t) \neq 0$, then, for any initial condition such that $d_t(0) = -\eta_t^\top \xi_t(0) \in \mathbb{R}^+$, the following slightly modified feedback control:

$$F_t = K_p^t q_t + K_d^t (W_t - \eta_t W_t^*) + mge_3 \tag{3.22}$$

with $W_t^* \geq \frac{1}{k_{d_3}^t} |\eta_t \triangle(t)|_{\max}$, ensures that the above i) and ii) assertions hold and guarantees that ξ_t is bounded.

Proof. The proof follows and exploits the same technical steps of the proof of Theorem 1. Since assertions made are almost the same using either (3.22) or (3.12) (equivalently (3.22) with $W_t^* = 0$) except for the last item iii), we will do the proof using (3.22) as feedback control and specify differences when necessaries.

When $\triangle \neq 0$ and $W_t^* \neq 0$, it is straightforward to verify that (3.15) becomes:

$$\dot{\mathcal{L}}_2 = -\frac{1}{d_t} v^\top {K_p^t}^{-1} K_d^t v + v^\top {K_p^t}^{-1} (\triangle + K_d^t W_t^* \eta_t)$$

Recall now the dynamics of $\dot{d}_t$ (3.16), $\frac{v}{d_t}$ (3.18), and of $\ddot{v}$ (3.19) in case where $\triangle \neq 0$ and $W_t^* \neq 0$.

$$\begin{aligned} \ddot{d}_t &= -k_{d_3}^t \frac{\dot{d}_t}{d_t} - k_{p_3}^t \beta_t^\triangle \\ \frac{d}{dt}(\frac{v}{d_t}) &= -\frac{1}{d_t}((K_d^t + \dot{d}_t I_3)\frac{v}{d_t} + \delta_v^\triangle) \\ \ddot{v} &= -\frac{K_d^t}{d_t}\dot{v} + \delta_{\dot{v}}^\triangle, \end{aligned} \tag{3.23}$$

with

$$\begin{aligned} \beta_t^\triangle(t) &= \frac{1}{k_{p_3}^t}(k_{d_3}^t W_t^* + \eta_t^\top \triangle) - \eta_t^\top q_t \\ \delta_v^\triangle &= K_p^t q_t - \triangle - K_d^t \eta_t W_t^* \\ \delta_{\dot{v}}^\triangle &= K_d \frac{\dot{d}_t}{d_t}\frac{v}{d_t} - K_p^t \dot{q}_t + \dot{\triangle}. \end{aligned}$$

Now since $\beta_t^\triangle(t) > 0, \forall t$ independently from the value chosen for W_t^*, direct application of [RHMS14, Th. 1-(2)] shows that the solution $(d_t, \dot{d}_t) \in (\mathbb{R}^+, \mathbb{R})$ exists and uniformly bounded $\forall t$ and converges (at least) asymptotically to $(0, 0)$.

By combining this with the fact that all terms involved in $\delta_v^\triangle$ (q_t, $\triangle$ and W_t^*) are bounded, direct application of [RHMS14, Lem. 4] concludes the boundedness of $\frac{v}{d_t}$. Since d_t is converging to zero, one concludes that v is converging to zero by a direct application of [RHMS14, Lem. 3]. Using the fact that $\dot{\triangle}$ is bounded by assumption, the proof of boundedness $\ddot{v}$ (3.23) and its convergence to zero is directly deduced from to proof the unperturbed case (3.19). From there and analogously to the unperturbed case (Theorem 1- proof of Item 2), one gets:

$$\frac{v}{d_t} = -{K_d^t}^{-1} K_p^t q_t + {K_d^t}^{-1} \triangle + \eta_t W_t^* + o(t) \tag{3.24}$$

with $o(t)$ an asymptotically vanishing term.

By multiplying both sides of (3.24) by $q_t^\top$ and using the fact that $\dot{\mathcal{L}}_1 = q_t^\top v$ (3.14), one obtains:

$$\frac{\dot{\mathcal{L}}_1}{d_t} = -q_t^\top {K_d^t}^{-1} K_p^t q_t + q_t^\top ({K_d^t}^{-1} \triangle + \eta_t W_t^* + o(t)).$$

From there one distinguishes between the two issues stated in the proposition:

1) $\eta_t^\top \triangle(t) = 0, \forall t$ and $W_t^* = 0$ (F_t given by (3.12))

By changing the time scale index and similarly to argument used at the end of the proof of Theorem 3.1, one concludes that $\|q_t\|$ is ultimately bounded by $\frac{\|\triangle\|_{\max}}{k^t_{p_{1,2}}}$. Since $d_t = \eta_t^\top \xi_t$ converges to zero, one concludes that $\|\pi_{\eta_t} \xi_t\|$ is ultimately bounded by Δ_ξ which is the solution of $\|\pi_{\eta_t} q_t\| = \frac{\|\triangle\|_{\max}}{k^t_{d_{1,2}}}$.

2) $\eta_t^\top \triangle(t) \neq 0$, and $W_t^* \neq 0$ (F_t given by (3.22))

In that case one concludes that the storage function $\mathcal{L}_1$ is decreasing as long as the right hand side of the above equation is negative and $d_t > 0$ and hence ξ_t is bounded. The argument of changing the time index is not valid in this case. $\square$

Remark 3.1. The focus of the above proposition is on robustness and adaptation of the controller with respect to the bounded perturbation $\triangle$. It is introduced particularly to show robustness of the proposed control law with respect to bounded perturbations in the plane orthogonal to η_t and, in the interest of a less complicated presentation, a slightly modified version of the control law (3.12) is introduced in (3.22) to be able to analyse the robustness of the closed loop system with respect to any bounded disturbance.

3.4.2 Going through the center of the window

To accomplish the goal of going through the window, while avoiding the wall and window edges, we propose to use the following control law

$$F_w = \sigma(q_w)(k_p^w \pi_{\eta_w} \bar{q}_w + k_d^w \pi_{\eta_w} W_w + k_\phi^w \eta_w ({\eta_w}^\top W_w - W_w^*) + mge_3), \tag{3.25}$$

with k_p^w, k_d^w and k_ϕ^w positive gains, $W_w^* > 0$ and

$$\sigma(q_w) = \begin{cases} 0 & \text{, if } \eta_w^\top q_w \geq 0 \\ 1 & \text{, if } \eta_w^\top q_w < 0, \end{cases} \tag{3.26}$$

which indicates that when the vehicle already crossed the window ($d_o \leq 0$), $F_w = 0$. Note that when $\eta_w^\top q_w < 0$, the resulting closed-loop system can be written as

$$\begin{cases} \dot{\xi}_w = v \\ \dot{v} = -k_p^w \pi_{\eta_w} \dfrac{\xi_w}{d_w} - k_d^w \pi_{\eta_w} \dfrac{v}{d_w} - k_\phi^w \eta_w ({\eta_w}^\top \dfrac{v}{d_w} - W_w^*) + \triangle, \end{cases} \tag{3.27}$$

The unknown term d_w is a convex combination of the unknown distances d_o and d_e:

$$\frac{1}{d_w} = (\alpha_w \frac{1}{d_o} + (1 - \alpha_w)\frac{1}{d_e})$$

which is deduced from (3.9) and (3.11) according to the definition of α_w (3.8):

$$d_w = \begin{cases} d_e, & \text{if } \|q_w\| \leq \epsilon \ (\xi_w \in \mathcal{M}) \\ \frac{d_o d_e}{\alpha_w d_e + (1-\alpha_w) d_o}, & \text{if } \epsilon < \|q_w\| < \epsilon + \delta \\ d_o. & \text{if } \|q_w\| \geq \epsilon + \delta \end{cases}$$

Remark 3.2. Note that the unknown time varying distance d_w involved in the closed-loop system is due to the use of feedback information $\bar{q}_w = \frac{\xi_w}{d_w}$ and $W_w = \frac{v}{d_w}$ in the control law. It is the key feature to achieve the double goal of avoiding collision with the wall and window edges as well, while ensuring the main task of going through the center of the window. When the vehicle approaches the wall or window edges outside the region $\mathcal{M}$, $d_w = d_o$ approaches zero. This leads to a high gain in the feedback control that allows avoiding the collision. When the vehicle is inside the region $\mathcal{M}$, $d_w = d_e$. This later is lower bounded by a positive constant so that the vehicle is able to go through the center of the window with a non-zero velocity. More details of analysis will be shown below.

Proposition 3.2. *Consider the system (3.1) with the control input given by (3.25). If the positive gains k_p^w, k_d^w and k_ϕ^w are such that $\frac{k_d^{w2}}{k_p^w} > \frac{r_w}{2}$ and for any arbitrary small $\epsilon > 0$, the chosen W_w^* satisfies:*

$$W_w^* > \frac{|\eta_w^\top \triangle(t)|_{\max}}{k_\phi^w} + \epsilon, \ \forall t \geq 0,$$

then for any initial condition satisfying $d_w(0) > 0$, the following assertions hold $\forall t \geq 0$:
1) there exists a finite time $t_w \geq 0$ at which the vehicle enters the region $\mathcal{M}$ ($\|q_w(t_w)\| \leq \epsilon$), and remains there as long as $\sigma(q_w) = 1$,
2) there exists a finite time $t_{\lim} > t_w$ at which the vehicle crosses the window $d_o(t_{\lim}) = 0$, with strictly negative velocity $\dot{d}_o(t_{\lim})$ such that the vehicle is inside the region $\mathcal{M}$ ($\|q_w(t)\| \leq \epsilon$ and $\sigma(q_w) = 1$) for all $t \in [t_w, t_{\lim})$.

Proof. We will consider hereafter only the case where $\sigma(q_w) = 1$ (or equivalently when $\eta_w^\top q_w < 0$). That is the situation in which the vehicle is going through the window while avoiding collision with the wall and the window edges.

From the dynamics of the closed-loop system (3.27), we focus first on the evolution of d_w. That is the evolution of the system in the direction η_w.

When $\|q_w(t)\| \geq \epsilon + \delta$, one has $d_w = d_o = -\eta_w^T \xi_w$ and hence:

$$\begin{aligned} \dot{d}_o &= -\eta_w^\top v \\ \ddot{d}_o &= -k_\phi^w \frac{\dot{d}_o}{d_o} - k_\phi^w \beta_w \end{aligned} \tag{3.28}$$

with $\beta_w = W_w^* + \frac{\eta_w^\top \triangle}{k_\phi^w} \geq \epsilon$.

When $\epsilon < \|q_w(t)\| < \epsilon + \delta$, one has $d_w = \frac{d_o d_e}{\alpha_w d_e + (1-\alpha_w) d_o}$ with α_w (defined by (3.8)) a uniformly continuous and bounded valued function on $[0, 1]$, and hence one verifies that:

$$\ddot{d}_o(t) = -k_\phi^w b(t) \frac{\dot{d}_o(t)}{d_o(t)} - k_\phi^w \beta_w \tag{3.29}$$

with $b(t) = \frac{(1-\alpha_w(t)) d_o(t) + \alpha_w(t) d_e(t)}{d_e(t)}$ a positive uniformly continuous and bounded function as long as $\epsilon < \|q_w(t)\| < \epsilon + \delta$ and $d_o(0) \in \mathbb{R}^+$. direct application of [HHMR12, Th. 5.1] to both equation (3.28) and (3.29), one can conclude that as long as $d_o(0) \in \mathbb{R}^+$ and $\|q_w(t)\| > \epsilon$ (or equivalently $\xi_w \notin \mathcal{M}$), $d_o(t) \in \mathbb{R}^+, \forall t \geq 0$ and $d_o(t)$ converges to zero exponentially (the exponential convergence of $d_o(t)$ is granted due to the fact that $\beta_w \geq \epsilon$) but never crosses zero and hence the vehicle will never touch the wall in a finite time. Additionally, one also proves, from [HHMR12, Th. 5.1], that there exists a finite time $t_1 \geq 0$ such that $\dot{d}_o(t) < 0$, $\forall t \geq t_1$ and hence d_o and d_w are decreasing after t_1.

When $\|q_w(t)\| \leq \epsilon$ (the situation when $\xi_w \in \mathcal{M}$), one has $d_w = d_e > d_o$. In this case one can easily verify that (3.28) can be rewritten as:

$$\ddot{d}_o = -k(t)\dot{d}_o - k_\phi^w \beta_w$$

with $k(t) = \frac{k_\phi^w}{d_e}$ a upper bounded positive gain as long as $d_e(t)$ is positive. Due to the fact that $\beta_w \geq \epsilon$, $\dot{d}_o$ is ultimately bounded by $-\frac{k_\phi^w \beta_w}{k(t)} \leq -\frac{k_\phi^w \epsilon}{k(t)}$ and hence one immediately ensures that there exists a finite time $t_2 \geq 0$ from which $\dot{d}_o(t) < 0, \forall t \geq t_2$. This implies that when $\|q_w(t)\| \leq \epsilon$ ($\xi_w \in \mathcal{M}$), d_o is decreasing $\forall t \geq t_2$ and hence d_o crosses zero in a finite time $\bar{t} > t_2$. Note that at $t = \bar{t}$, one has $\sigma(q_w(\bar{t})) = 0$ according to (3.26).

Consider now the the dynamics of the closed-loop system (3.27) in the plane π_{η_w}. That is the dynamics of $\xi_\perp := \pi_{\eta_w}\xi_w$. By defining $v_\perp := \pi_{\eta_w} v$ and $\triangle_\perp := \pi_{\eta_w}\triangle$, one gets:

$$\begin{aligned} \dot{\xi}_\perp &= v_\perp \\ \dot{v}_\perp &= -\frac{k_d^w}{d_w}\left(v_\perp + \frac{k_p^w}{k_d^w}\xi_\perp\right) + \triangle_\perp. \end{aligned}$$

Define a new state

$$z = v_\perp + \frac{k_p^w}{k_d^w}\xi_\perp, \tag{3.30}$$

and the following positive definite storage function:

$$\mathcal{L}_3 = \frac{1}{2}\|z\|^2 + \frac{1}{2}\left(\frac{k_p^w}{k_d^w}\right)^2\|\xi_\perp\|^2,$$

with time derivative

$$\begin{aligned} \dot{\mathcal{L}}_3 &= -\left(\frac{k_p^w}{k_d^w}\right)^3\|\xi_\perp\|^2 - \left(\frac{k_d^w}{d_w} - \frac{k_p^w}{k_d^w}\right)\|z\|^2 + z^\top \triangle_\perp \\ &\leq -\left(\frac{k_p^w}{k_d^w}\right)^3\|\xi_\perp\|^2 - \frac{\|z\|}{k_d^w}\left(\left(\frac{k_d^{w2}}{d_w} - k_p^w\right)\|z\| - k_d^w\|\triangle_\perp\|\right), \end{aligned} \tag{3.31}$$

which is negative-definite provided that $0 < d_w < \frac{k_d^{w2}}{k_p^w}$ and $\|z\| \geq \frac{d_w k_d^w \|\triangle_\perp\|_{\max}}{k_d^{w2} - d_w k_p^w}$.

Proof of Item 1:

To show there exists a finite time $t_w \geq 0$ at which the vehicle enters the region $\mathcal{M}$ and remains there as long as $\sigma(q_w) = 1$, we proceed using a proof by contradiction in two steps.

In the first step, we assume that ξ_w is not converging to $\mathcal{M}$ in a finite time t_w and hence $\|q_w(t)\| > \epsilon$, $\forall t$. In the second one, we assume that ξ_w is switching indefinitely between the two regions.

i) Consider the situation for which the initial condition is such that $\|q_w(0)\| > \epsilon$ (outside the region $\mathcal{M}$). Using the fact that there exists a finite time instant t_1 from which d_w is decreasing and converging to zero but never crosses zero in finite time (see the above discussion), one concludes that z (3.30) is exponentially converging to zero and hence:

$$v_\perp = \dot{\xi}_\perp = -\frac{k_p^w}{k_d^w}\xi_\perp + o(t),$$

with $o(t)$ an exponential vanishing term. This in turn implies that $\xi_\perp$ (resp. $v_\perp$) is converging to zero exponentially. Combining this with the fact that $d_w(t)$ (resp. $d_o(t)$) is converging to zero, one concludes that there exists a finite time t_w at which $\|q_w(t_w)\| < \epsilon$ ($\xi_w(t_w) \in \mathcal{M}$), which contradicts the first part of the assumption.

ii) Consider the situation for which the vehicle is switching indefinitely between the two regions. Since $d_o(t)$ (respectively d_w) is decreasing $\forall t \geq \max\{t_1, t_2\}$ for both cases of $\|q_w\| > \epsilon$ and $\|q_w\| \leq \epsilon$ with the fact that $(\xi_\perp, v_\perp)$ converges exponentially to $(0,0)$ (proof of the step (i)), one concludes that there exists a finite time $t_w \geq 0$ at which the vehicle enters the region $\mathcal{M}$ ($\|q_w(t_w)\| \leq \epsilon$), and remains there as long as $\sigma(q_w) = 1$, which contradicts the assumption.

Proof of Item 2:

When ξ_w is inside the region ($\|q_w\| \leq \epsilon$), one guarantees that $\mathcal{L}_3$ (3.31) is decreasing as long as $0 < d_w < \frac{k_d^{w2}}{k_p^w}$ and $\|z\| \geq \frac{d_w k_d^w \|\Delta_\perp\|_{\max}}{k_d^{w2} - d_w k_p^w}$. Now since there exists a time $\bar{t} > t_w$ such that $d_o(\bar{t}) = 0$, one concludes that $t_{\lim}$ exists and it is equal to $\bar{t}$. □

3.4.3 Application Scenario

The double goal of crossing the window and landing on the landing pad can be achieved by simply applying the control laws F_w and F_t in sequence, with an adequate trigger to switch from F_w to F_t. Taking the limitation of the cameras' field of view into the consideration, there will be four different modes during the full process of going through a window and landing on the pad. When $t \in [T_1, T_2)$, $mode = 1$ and F_w (3.25) is active. When the vehicle approaches to the center of the window, the on-board camera loses the full image of the window and *mode* changes to 2. When $t \in [T_2, T_3)$, *mode* 2 is active and the open-loop control $\eta_w|\eta_w^\top F_w(T_2^-)|$ is applied, where T_2^- is the last time instance before the camera loses the image of the window. At the time instance $t = T_3$, when the downward-looking camera detects the landing pad, the *mode* changes to 3 and the control law F_t (3.12) is applied when $t \in [T_3, T_4)$. At time instance $t = T_4$, the vehicle is already close to the center of the landing target and it is safe to slowly shutdown the quadrotor motors. In order to avoid inadequate behaviors, the switch from *mode* 2 to 3 is only triggered once. Moreover, in practice, due to the limitation of camera's field of view, the initial errors should not be large and should converge to zero fast enough, thereby allowing the vehicle to almost align with the center of the window before switching to *mode* 2. Additionally, the position of the landing target should be close enough to the window so that the quadrotor is able to timely detect the landing target after it goes through the window. The switching between different modes is based on the combination of selected frames from both the ground and horizontal on-board cameras obtained in the experiments. The detail on the adopted procedure is described in Section 3.6.

3.5 Simulation Results

In this section, simulation results are presented to illustrate the behavior of the closed-loop system using the proposed controller. A high-gain inner-loop controller is used to control the attitude dynamics [TLS+15]. It generates the torque inputs in order to stabilize the orientation of the vehicle to a desired one defined by the desired thrust direction $R_d e_3$, which is provided by the outer-loop image-based controller, and the desired yaw chosen to align the forward-looking camera with direction orthogonal to the wall. In the simulation, the position of the center of the window is $[-0.5\ 0\ -1.72]^\top$ and the position of the center of the target is $[0\ 0\ 0]^\top$. The control algorithm is tested with different initial conditions, always starting from a position outside the room containing the target (see Fig. 3.1). The initial velocity of the quadrotor is $v(0) = [0\ 0\ 0]^\top$, and the gains are chosen as $K_p^t = \text{diag}[4\ 4\ 1.75]$, $K_d^t = 4I_3$, $k_d^w = 0.8$, $k_p^w = 1$, $k_\phi^w = 1$ and $W_w^* = 0.3$

As shown in Fig. 3.1, with different initial positions the quadrotor successfully avoids the wall and window, goes through the center of the window, and then lands on the center of the landing target. Figures 3.7-3.15 show in detail the time evolution of quadrotor's state variables, virtual input, and image features for the initial position $\xi(0) = [-2\ 0.1\ -1.82]^\top$. The time evolution of the active mode is also specified. In mode 1, the quadrotor is approaching the window; in mode 2, it is crossing the window with no image cues; in mode 3, it starts detecting the landing pad and transitions to the landing maneuver; and finally in mode 4, the motors are shutdown.

Figure 3.7 shows the time evolution of the vehicle's position and the dashed lines are the coordinates of window's center. From Figure 3.7, we can see the quadrotor first converges to the center line of the window and then converges to the center point of the target. Fig. 3.8 shows the time evolution of the vehicle's velocity. The virtual control input F is shown in Fig. 3.9. The angular velocity of the quadrotor is depicted in Fig. 3.10 and Fig. 3.11 depicts the time evolution

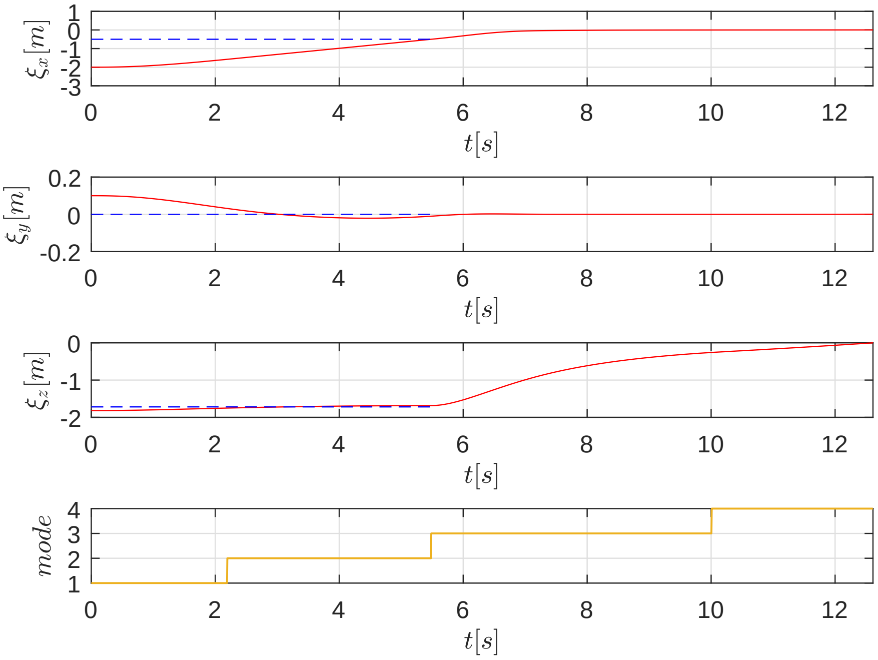

Figure 3.7: Quadrotor's position

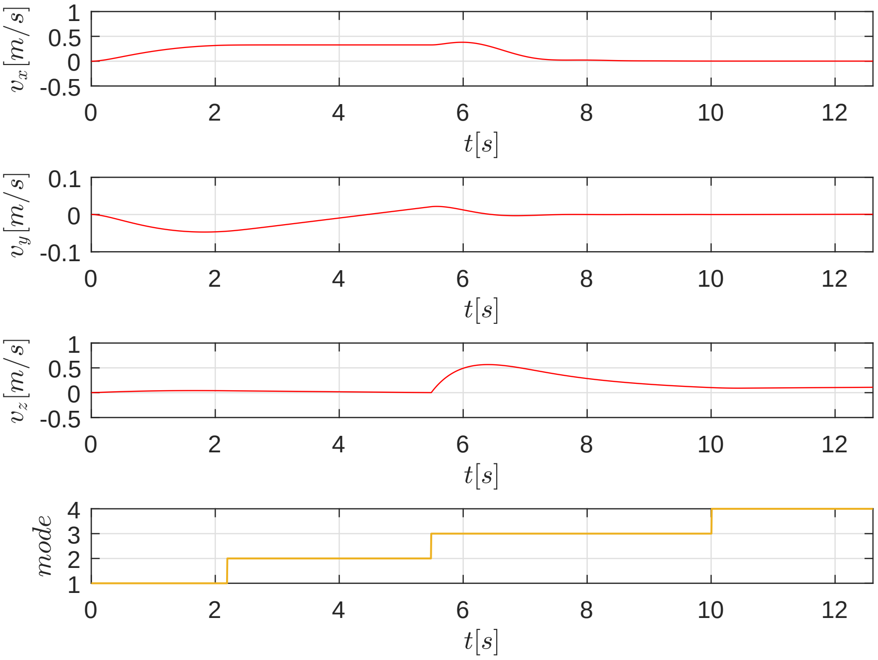

Figure 3.8: Quadrotor's velocity

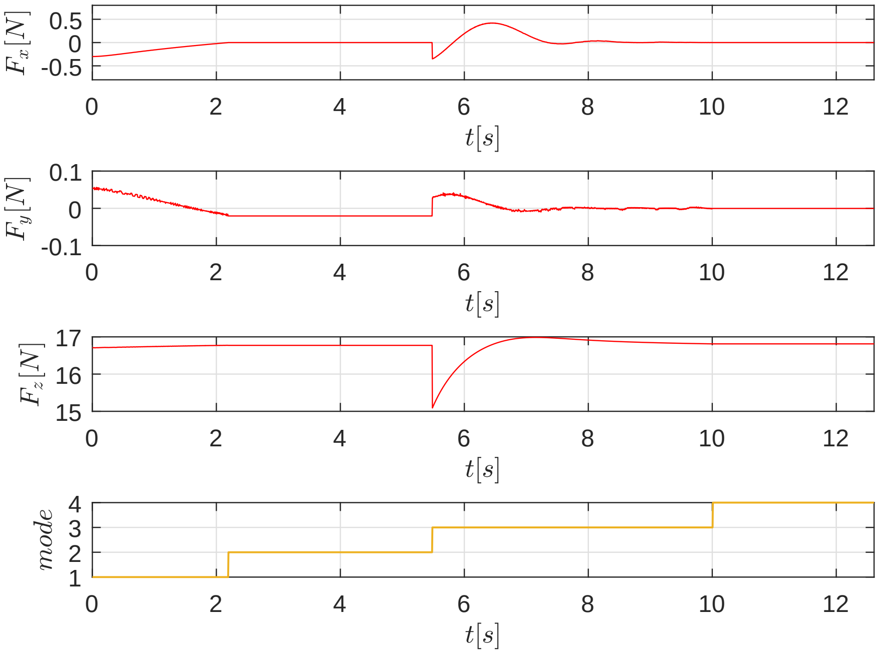

Figure 3.9: Virtual control input F

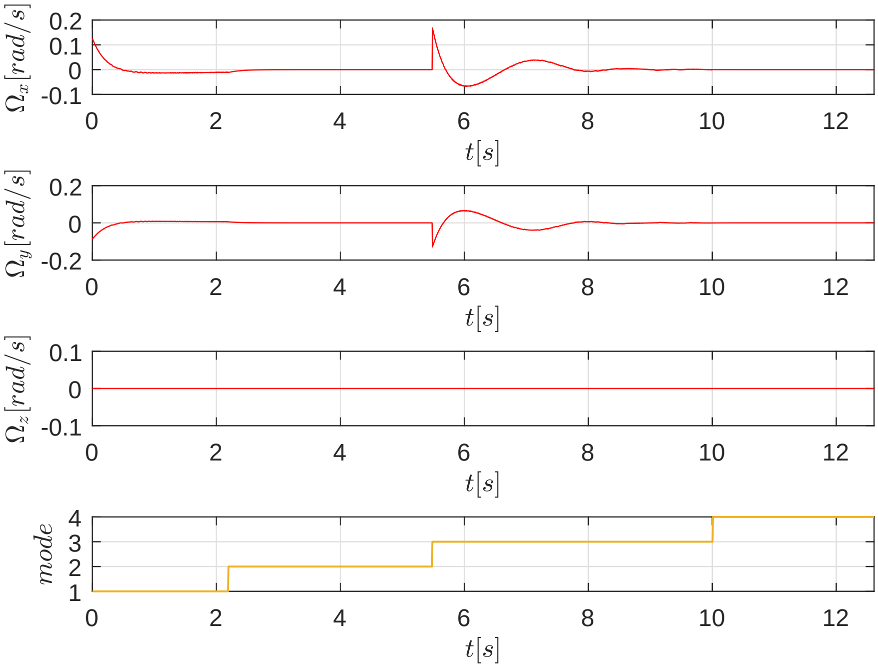

Figure 3.10: Evolution of angular velocity Ω

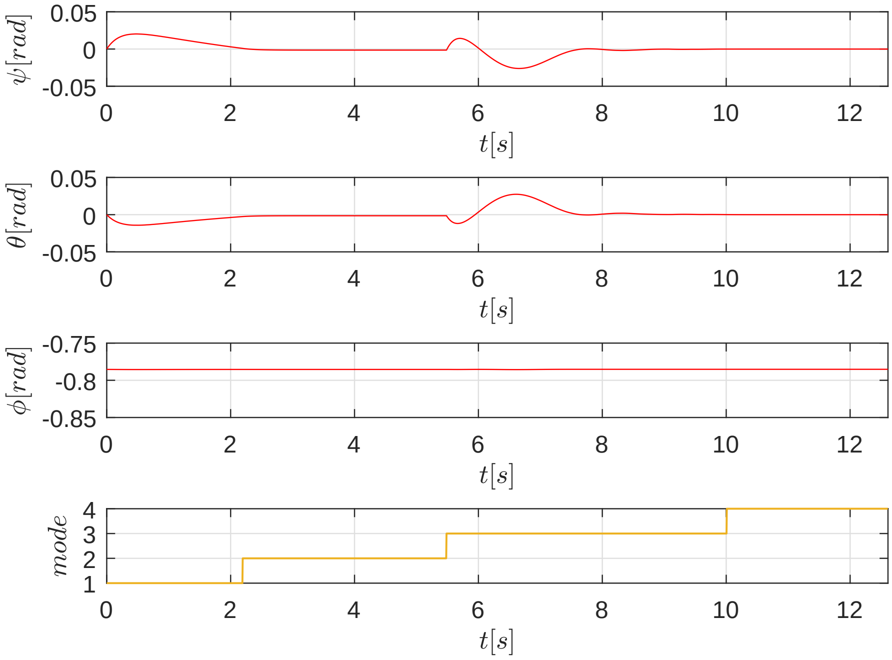

Figure 3.11: Evolution of Euler angles

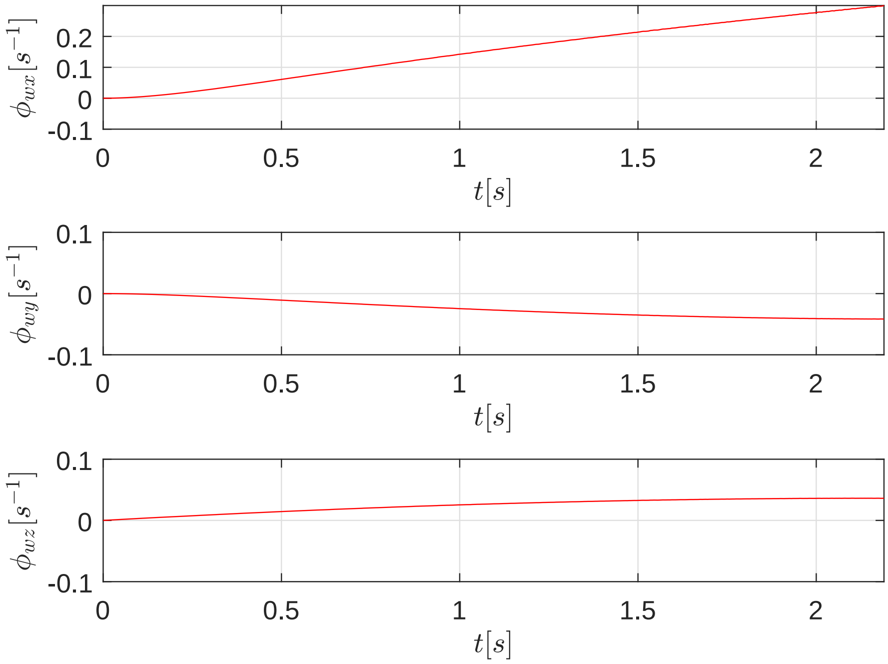

Figure 3.12: Translational optical flow using for going through the window during mode 1.

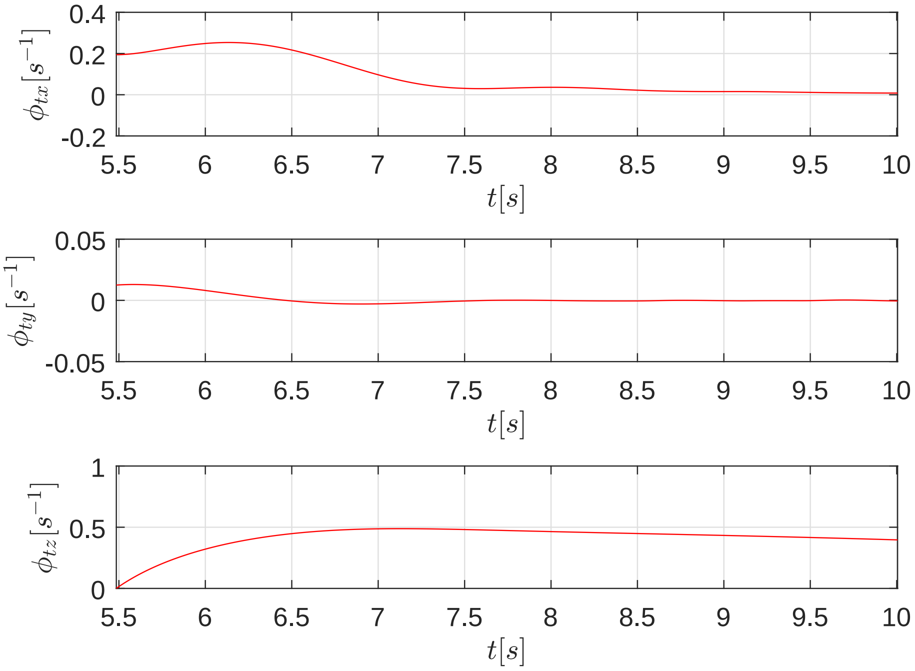

Figure 3.13: Translational optical flow using for landing during mode 3.

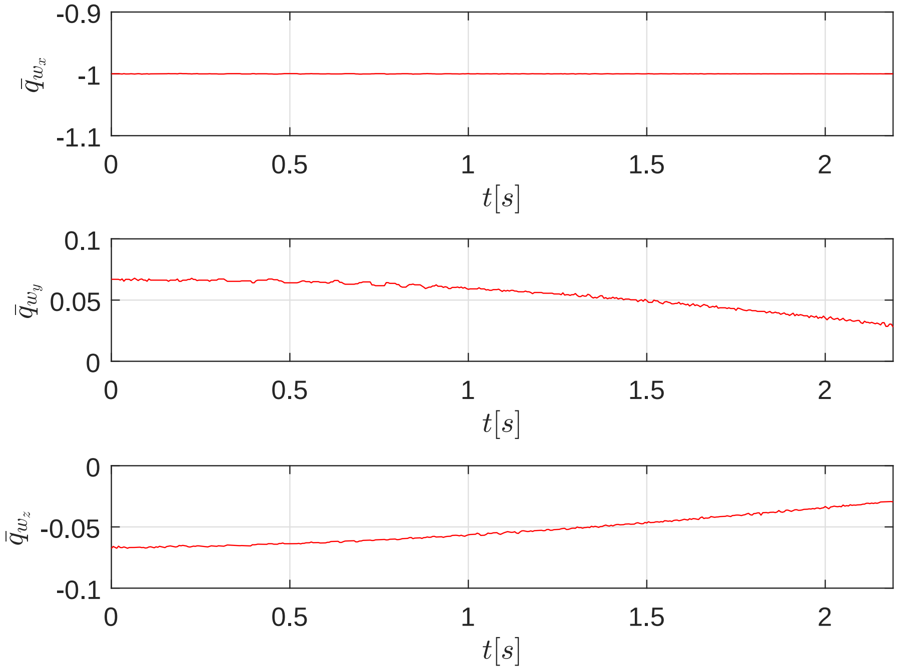

Figure 3.14: Image feature $\bar{q}_w$ during mode 1.

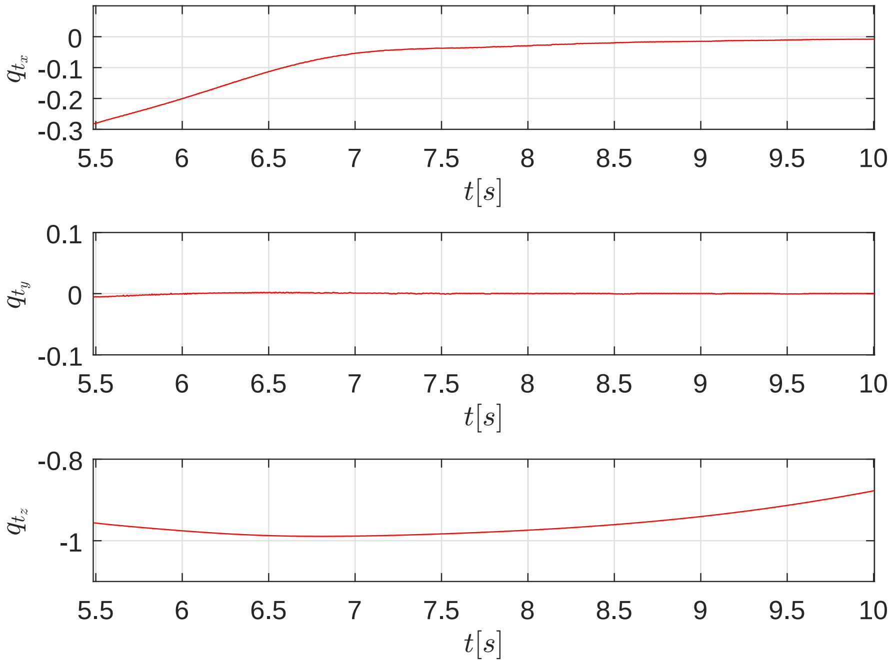

Figure 3.15: Image feature q_t during mode 3.

of Euler angles, which indicates a good compromise in terms of time-scale separation between the outer-loop and inner-loop controller. Figures 3.12 and 3.13 show the translational optical flow used for going through the window in mode 1 and for landing in mode 3, respectively. The evolution of image features of $\bar{q}_w$ and q_t are depicted in Figures 3.14 and 3.15, respectively. We can see that the image features $\bar{q}_w$ and q_t approach to the desired values $[-1\ 0\ 0]^\top$ and $[0\ 0\ 0]^\top$, respectively, before the on-board cameras lose the image information.

3.6 Experiments

3.6.1 Experimental setup

In order to set up the experiment, a movable wall was used to divide the testing space into two smaller compartments and a landing pad was placed on the ground of the second one. The partition wall contains a rectangular window and is textured as a brick wall to provide the background optical flow, as shown in Fig. 3.18. The vehicle used for the experiments is an Asctec Pelican quadrotor (Fig. 3.16) with weight 1676g and the arm length from the center of mass to each motor is 20cm. The available commands are thrust force and attitude which are derived from the force F provided by the outer-loop controller (3.12) (respectively (3.25)) and the desired yaw angle. The quadrotor is equipped with two wide-angle cameras, one pointing towards the ground and another is facing the forward direction, pointing at the wall. Recalling

Assumption 3.1, the downward-looking camera reference frame coincides with the vehicle's body fixed frame and the rotation matrix from the forward-looking camera reference frame to the body frame is ${}^{B}_{c}\mathbf{R} = R_Z(-\frac{\pi}{4})R_X(\frac{\pi}{2})$. These two cameras are uEye UI-122ILE models featuring a 1/2-in sensor with global shutter which operate at a resolution of 752×480 pixel at 50 frames per second and are provisioned with 2.2-mm lenses.

Figure 3.16: Asctec Pelican quadrotor.

In the experiments, we used a rapid prototyping and testing architecture using a MATLAB/Simulink environment to integrate the sensors and the cameras, the control algorithm and the communication with the vehicle. The controller is developed and tuned on a MATLAB/Simulink environment and C code is generated and compiled to run onboard the vehicle as a final step. The onboard computer (a 4-core Intel i7-3612QE at 2.1GHz, named AscTec Mastermind) is responsible for running in Linux three major software components that provide:

1. interface with the camera hardware, image acquisition, feature detection and optical flow computation;
2. computation of the vehicle force references from the image features, translational optical flow, and angular velocity and rotation matrix estimates provided by the IMU;
3. interface with microprocessor, receiving IMU data and sending force references to the inner-loop controller.

A Python program running on the onboard computer performs detection of the window, detection of landing target, and optical flow computation using the OpenCV library. ARUCO markers, for which built-in detection functions exist in the OpenCV library, are used to define the landmarks on the landing pad. In order to fit the camera's field of view during the full process of landing, the landmarks are composed by 4 groups of ARUCO markers and in each group there are 4 ARUCO markers with same border size but different identifier (id) as shown in Fig. 3.17. When the camera is far away from the markers, the group of larger markers can be seen and when the camera is near the ground, only the smaller group of the landmarks will be shown in the field of view. The rectangular window shape is detected using the library code originally developed for ARUCO marker's border detection. The detected window frame (in green) and the window's coordinate system overlayed on the image are show in Fig. 3.18 (1), (2), and (3). The translational optical flow is also computed onboard. The computation is based on the conventional image plane optical flow field provided by a pyramidal implementation of the Lucas-Kanade algorithm. The detailed description of the computation can be found in [SCH+16]. The small vectors represented in Fig. 3.19 represent the translational optical flow of the image pixels. In order to provide ground truth measurements and evaluate the performance of the proposed controller, a VICON motion capture system[VIC14] which comprises 12 cameras is used together with markers attached to the quadrotor, window, and landing target. The motion

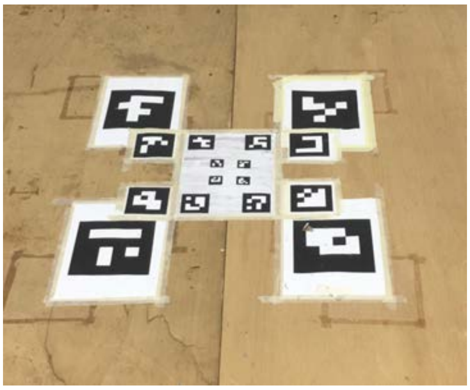

Figure 3.17: ARUCO markers on the landing pad.

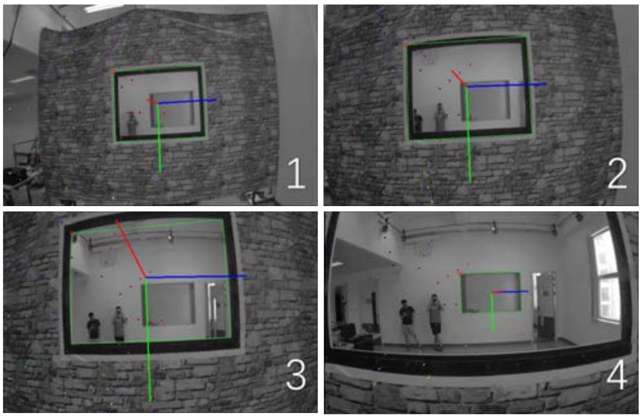

Figure 3.18: Selected frames from the forward-looking camera.

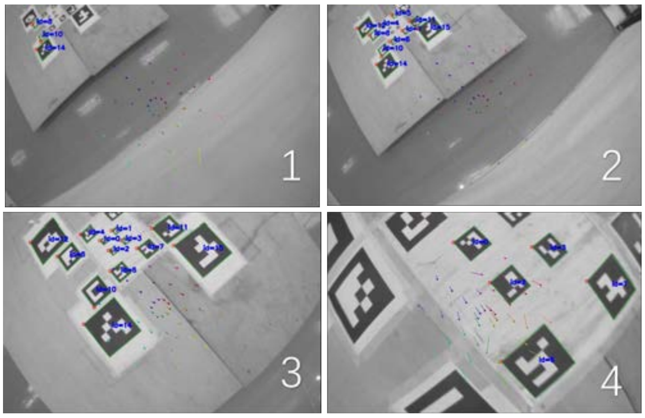

Figure 3.19: Selected frames from the downward-looking camera.

capture system is able to accurately locate the position of the markers, from which ground truth position and orientation measurements are gathered. Note that, none of the measurements from the motion capture system are used in the proposed controller.

3.6.2 Experimental results

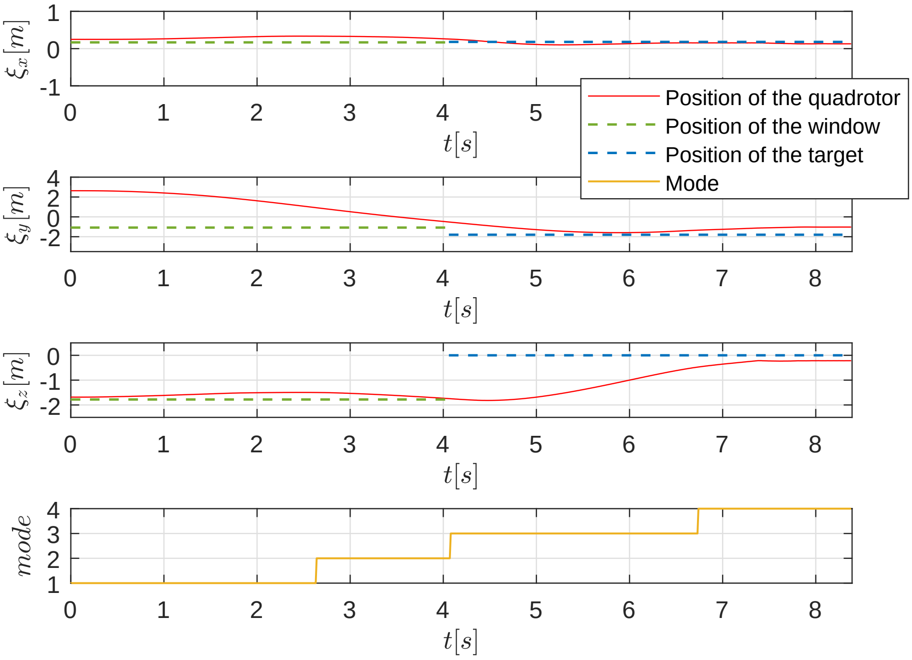

Figure 3.20: Quadrotor's trajectory and mode

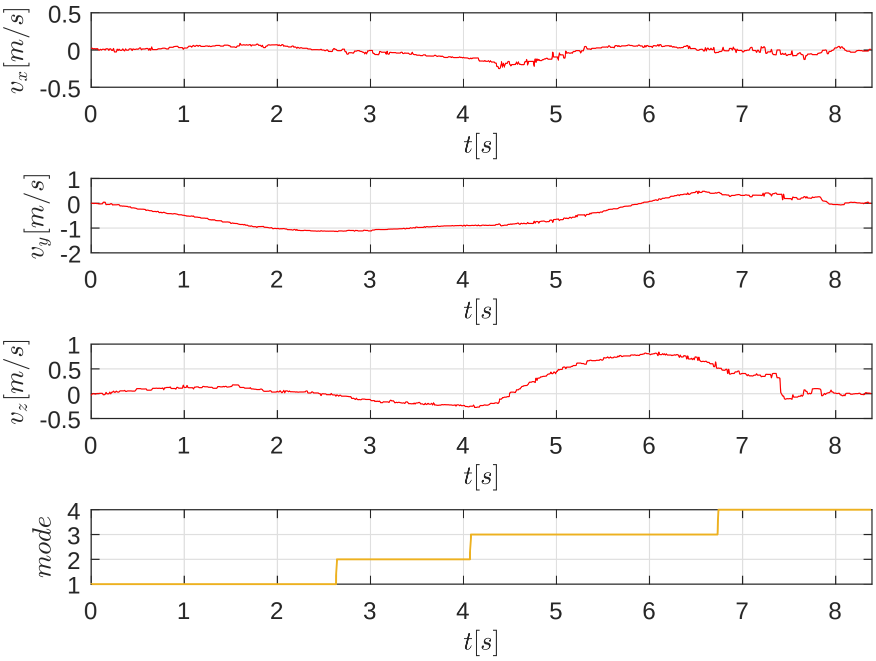

Figure 3.21: Quadrotor's velocity

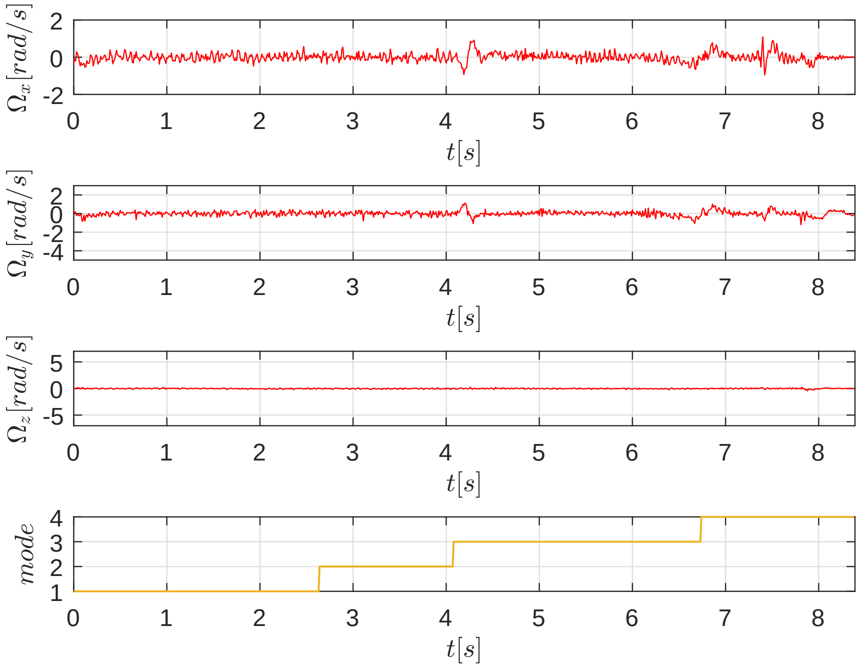

Figure 3.22: Evolution of angular velocity

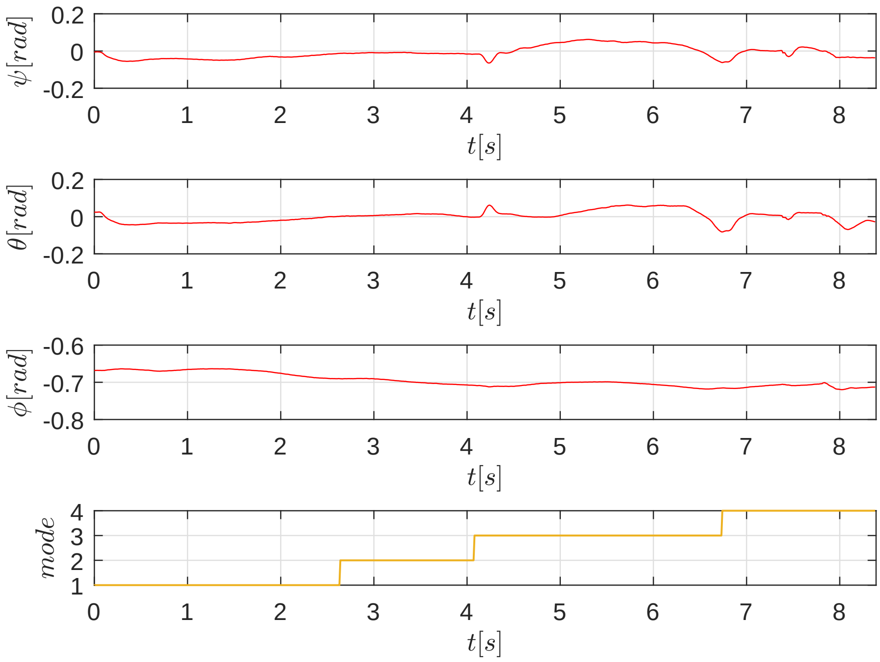

Figure 3.23: Evolution of euler angel

The experiments were conducted with the same control gains as the simulations. Before the proposed controller is triggered, the vehicle is hovering at position $\xi = [0.15, 1.79, -1.76]$ m, which is outside the space containing the landing pad. As mentioned in Section 3.4.2, there are four different modes during the full process of going through a window and landing on the target due to the limitation of the field of view of the on-board cameras. Fig. 3.18 shows the selected frames in a timed sequence from the forward-looking camera. These four frames are a fixed time step apart and were taken during a *mode* 1 to *mode* 2 transition. In Fig. 3.18 (1), (2), and (3), *mode* 1 is active, and we can see that the window frame is well detected. In Fig. 3.18 (1), $t = T_1$ and the controller F_w is triggered. In Fig. 3.18 (2) and (3), the vehicle is still in *mode* 1 and approaches the center of the window. As the vehicle approaches the window, the window frame disappears from the field of view of the camera and at time $t = T_2$ the *mode* commutes to 2, as shown in Fig. 3.18 (4). Note that during transition from *mode* 1 to 2, instead of losing the window frame, the camera may detect rectangles other then the target window, as depicted in Fig. 3.18 (4). In order to avoid this situation, the *mode* changes from 1 to 2 if the pixel coordinates change instantaneously in a way that is incompatible with smooth tracking of the same window object. Fig. 3.19 shows the selected frames in a timed sequence from the downward-looking camera. These four frames were taken at fixed time steps during a transition from *mode* 2 to 3 to 4. As shown in Fig. 3.19 (1), the vehicle has already crossed the window but the landing pad is not fully detected thus the *mode* is still 2. At time instance $t = T_3$, as shown in Fig. 3.19 (2), the downward-looking camera detects successfully the landing pad, the *mode* is switched to 3 and F_t is applied as control input. Recall that the switching from *mode* 2 to *mode* 3 is only triggered once in order to avoid inadequate behavior. In Fig. 3.19 (3), the vehicle approaches the target and the *mode* is still 3. At the time instance $t = T_4$, when the quadrotor has almost reached the target position (see Fig. 3.19 (4)), the *mode* changes to 4 and it is safe to slowly shutdown the motors. Figures 3.20 and 3.21 show the position and velocity coordinates of the vehicle

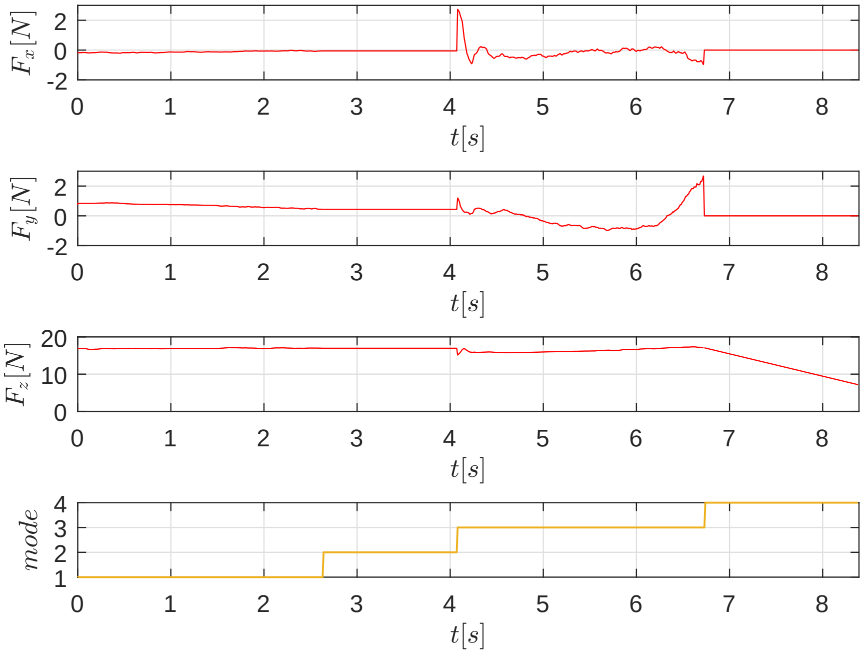

Figure 3.24: Controller output F

provided by VICON, respectively. We can see that the vehicle goes through the center of the window at the end of *mode* 2 and finally lands on the target. Fig. 3.22 shows the evolution of the

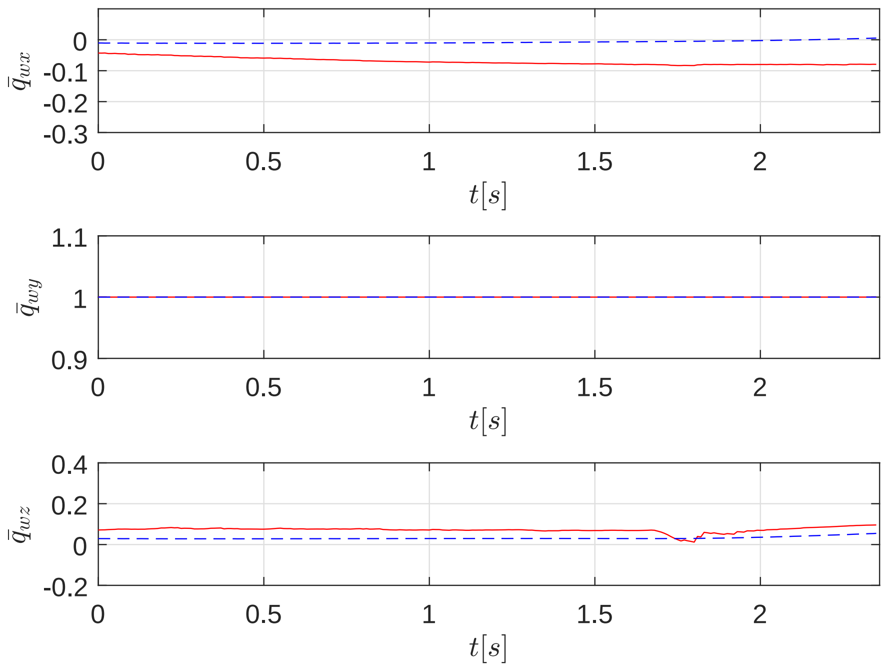

Figure 3.25: Image features $\bar{q}_w$ during mode 1. Solid line represents $\bar{q}_w$ computed from the image sequence. Dashed line represents $\bar{q}_w$ provided by the VICON system.

angular velocity and Fig. 3.23 show the evolution of the Euler angles. From Fig. 3.23, we can see that a good compromise in terms of time-scale separation between the outer-loop and inner-loop controllers is attained, which indicates that the inner-loop controller is sufficiently fast to track the outer-loop references, including during the transitions between different modes. Figure 3.25 shows the image feature $\bar{q}_w$ used for going through the window. The solid line represents $\bar{q}_w$ computed from the image sequence and the dashed line represents $\bar{q}_w$ provided by the VICON system. There are slight differences between these two computations due to the fact that rotation matrix R provided by the IMU is affected by the surrounding magnetic field generated by the fast rotating motors. Figures 3.27 and 3.26 show the translational optical flow used for going through the window and for landing respectively. The solid red lines represent the translational optical flow computed from the image sequence and the dashed line represents the translational optical flow derived from VICON measurements. The video of the experimental results can be found in `https://youtu.be/DbpeGfJMHk0`.

3.7 Conclusion

This chapter considers the problem of controlling a quadrotor to go through a window and land on planar target, using an Image-Based Visual Servo (IBVS) controller that relies on optical

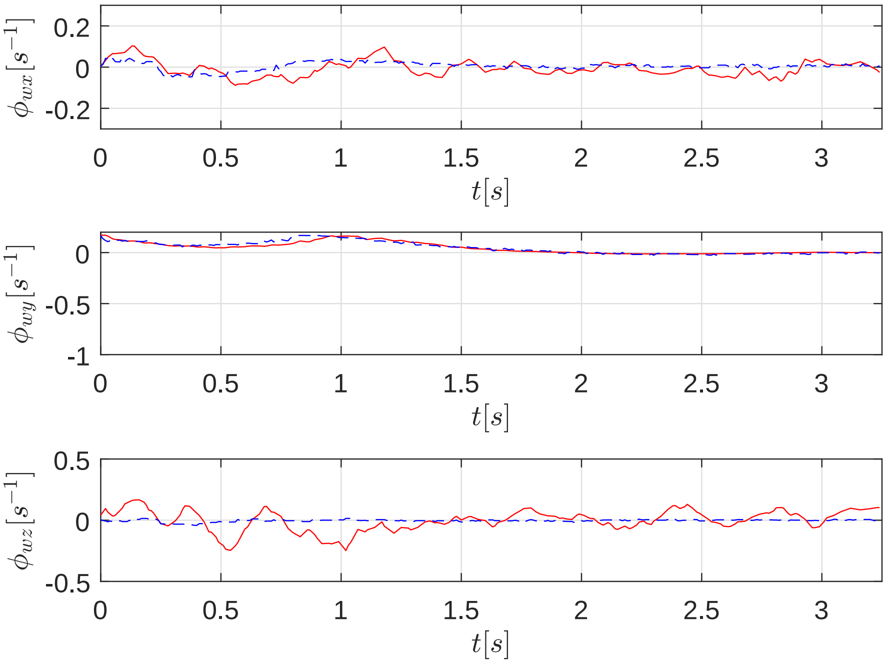

Figure 3.26: Translational optical flow using for going through the window during mode 1. Solid line represents the translational optical flow computed from the image sequence. Dashed line represents the translational optical flow provided by the VICON system.

flow measurements. For control purposes, the centroids vectors provided by the combination of the corresponding spherical image measurements of landmarks (corners) for both the window and the target are used as position feedback. The translational optical flow relative to the wall, window edges, and target plane is used as velocity measurement. With the initial position outside the room containing the target, the proposed control law guarantees that the quadrotor aligns itself with the center line orthogonal to the window, crosses it with non-zero velocity and finally lands on the planar target successfully without colliding the wall or the edges of the window. Rigourous proofs of convergence and/or piratical stability of closed-loop system are provided when the system is subjected to unknown bounded disturbances. Simulation and experimental results show the effectiveness of the overall proposed control scheme.

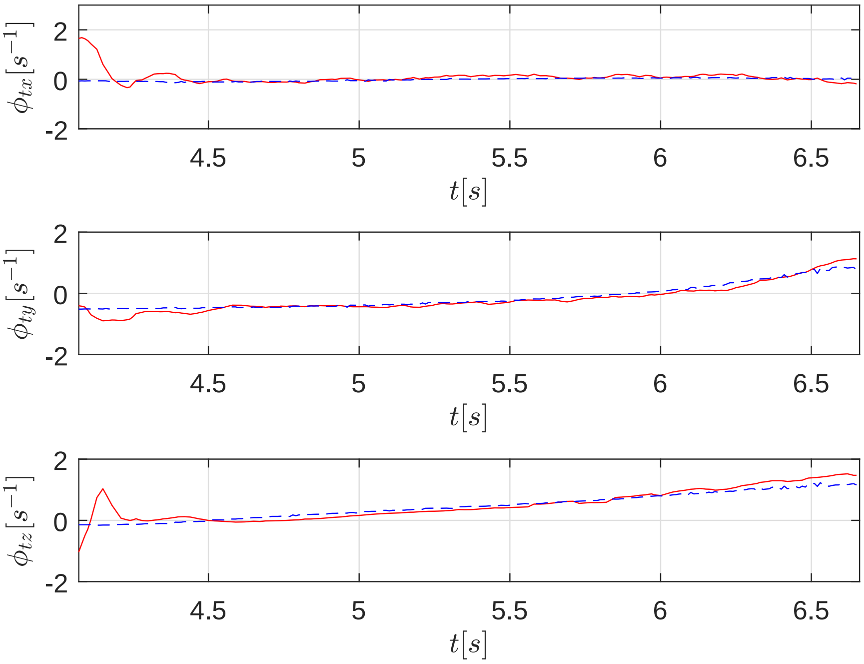

Figure 3.27: Translational optical flow using for landing during mode 3. Solid line represents the translational optical flow computed from the image sequence. Dashed line represents the translational optical flow provided by the VICON system.

4

BEARING LEADER-FOLLOWER FORMATION CONTROL UNDER PERSISTENCE OF EXCITATION

4.1 Introduction

In this chapter, we consider the problem of controlling a leader-follower formation (i.e. a formation under a directed acyclic graph that has a spanning tree, see Fig. 4.1) using only bearing and relative velocity measurements. We particularly focus on the problem of stabilizing the formation's geometric pattern to a desired one by exploiting persistence of excitation (PE) of the bearings of the desired formation. Note that this PE condition can be enforced a priori and has no dependence on the initial conditions of system.

The concept of persistence of excitation (PE) is a well-known concept in adaptive control and identification of linear systems. It has been recently exploited for position estimation from bearing and biased velocity measures in [HS17], [LBHMS17]. The work in [HS17] exploit the Continuous Riccati Equation (CRE) to calculate observer gains yielding global exponential stability of zero estimation errors under PE conditions. In particular, the observation of a single point source may be sufficient, provided that the body motion is PE. Based on these results, a SLAM problem using the PE bearing measurement is also introduced in [LBHMS17].

Inspired by the work in [LBHMS17] and exploring the duality between the control and estimation problems, we propose bearing formation control laws for leader-follower formation with both single- and double-integrator dynamics and introduce of a generalised rigidity concept : *relaxed bearing rigidity*, which makes the connection between bearing PE and bearing rigidity theory specifically for leader-follower formation. The key contribution is to show that the required classical conditions on the graph topology (bearing rigidity and constraint consistence) used to guarantee stabilization of the formation to a desired shape up to a scale are relaxed here in a natural manner by exploiting PE of the bearing information generated by the desired formation. The proposed control approach draws inspiration from the work in [TZS+19], which

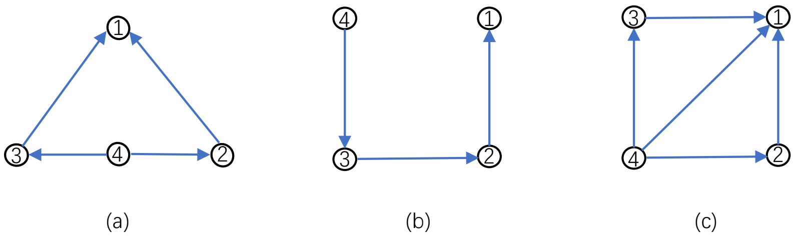

Figure 4.1: Examples of leader-follower formations. The formations in (a) and (b) are not bearing rigid and in (c) is bearing rigid but not constraint consistent. The asymptotic stability of these three formations can not be guaranteed using bearing controllers relying only on bearing rigidity theory and constraint consistence ([ZZ15a]). It is however guaranteed in this chapter under the proposed PE condition.

presents a first-order bearing formation control law, considering a LFF graph topology. A distinctive feature of the present work is the shift of focus from static formations to time-varying formations. The approach relies on the simplicity of controllers that guarantee (local) exponential stability of the formation towards the desired one in terms of shape and scale when the bearing PE conditions are fulfilled.

This chapter is organized as follows. Section 4.2 introduces the preliminaries about graph theory on directed graphs and the concept of persistently exciting on bearings. Section 4.3 describes the concepts of bearing PE leader-follower formation and relaxed bearing rigidity. Section 4.5 proposes bearing-based controllers and shows that exponential stabilization of the formation is achieved under the bearing PE conditions. Section 4.6 illustrates the performance of the proposed control strategy on a relaxed rigid formation. The chapter concludes with some final comments in Section 4.7.

4.2 Preliminaries

4.2.1 Directed graph topologies

Consider a system of n ($n \geq 2$) connected agents. The underlying interaction topology can be modelled as a digraph (directed graph) $\mathcal{G} := (\mathcal{V}, \mathcal{E})$, where $\mathcal{V} = \{1, 2, \ldots, n\}$ is the set of vertices and $\mathcal{E} \subseteq \mathcal{V} \times \mathcal{V}$ is the set of directed edges. In this work, the graph is interpreted as sensing graph, meaning that if the ordered pair $(i, j) \in \mathcal{E}$ then agent i can access or sense information about agent j, which is called a neighbor of agent i. Note that in a communication graph the information flow would be in the opposite direction. The set of neighbors of agent i is denoted by $\mathcal{N}_i := \{j \in \mathcal{V} | (i, j) \in \mathcal{E}\}$. Define $m_i = |\mathcal{N}_i|$, where $|.|$ denotes the cardinality of a set. A directed path is a finite sequence of distinct vertices $v_1, v_2, \ldots, v_{k-1}, v_k$, such that (v_{i-1}, v_i), $2 \leq i \leq k$ belongs to $\mathcal{E}$. A directed cycle is a directed path with the same start and end vertices, i.e. $v_1 = v_k$. A digraph $\mathcal{G}$ is called an acyclic digraph if it has no directed cycle. The digraph $\mathcal{G}$ is called a directed tree with a root vertex $i,\ i \in \mathcal{V}$, if for any vertex $j \neq i,\ j \in \mathcal{V}$, there exists only one directed path connecting j to i. Note that a directed tree is acyclic. We say that $\mathcal{G}$ has a directed spanning tree, if there exists a subgraph of $\mathcal{G}$ that is a directed tree and contains all the vertices of $\mathcal{G}$.

4.2.2 Persistence of Excitation on bearings

Definition 4.1. *A positive semi-definite matrix* $\Sigma(t) \in \mathbb{R}^{n\times n}$, *is called persistently exciting (PE) if there exists* $T > 0$ *and* $\mu > 0$ *such that for all* $t > 0$

$$\tfrac{1}{T}\int_t^{t+T} \Sigma(\tau)d\tau \geq \mu I_n. \tag{4.1}$$

Definition 4.2. *A direction* $y(t) \in \mathbb{S}^{d-1}$ $(d \geq 2)$ *is called persistently exciting (PE) if the matrix* $\pi_{y(t)}$ *satisfies the PE condition according to Definition 4.1 with* $0 < \mu < 1$.

Lemma 4.1. *Let* $Q_\pi := \sum_{i=1}^{l} \pi_{y_i}$. *The matrix* Q_π *is persistently exciting, if one of the following conditions is satisfied:*

1. *there is at least one PE direction* y_i,
2. *there are at least two uniformly non-collinear directions* y_i *and* y_j, $i,j \in \{1,...,l\}$, $i \neq j$. *That is:* $\exists \epsilon_1 > 0$, $\forall t \geq 0$ *such that* $|y_i(t)^\top y_j(t)| \leq 1 - \epsilon_1$.

Proof. The proof is given in [LBHMS17, Lemma 3]. □

4.3 Bearing PE leader-follower formation and relaxed bearing rigidity

Definition 4.3. *A digraph* $\mathcal{G} = (\mathcal{V}, \mathcal{E})$ *has a leader-follower structure if it is acyclic and has a directed spanning tree. It has a minimal leader-follower structure if each follower* i $(i \in \mathcal{V},\ i \neq 1)$ *has only one neighbor.*

The leader-follower structure defined above is more general than the leader-first follower structure (LFF) considered in [TZS⁺19], for which each follower has two neighbors except the first follower which is only connected to the leader. In our setting, the leader is the root vertex which has no neighbors and each of the other followers has at least one neighbor. Without loss of generality, the agents are numbered (or can be renumbered) such that agent 1 is the leader, i.e. $\mathcal{N}_1 = \emptyset$, agent 2 is the first follower with $\mathcal{N}_2 = \{1\}$, and for each agent $i \geq 3$ the set of neighbors satisfies $\mathcal{N}_i \subseteq \{1,\ldots,i-1\}$. An example of a possible 5-agent leader-follower graph is shown in the Figure 4.2.

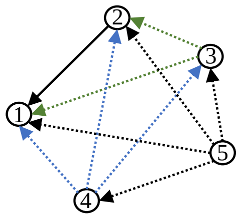

Figure 4.2: Possible connections of a leader-follower structure when $n = 5$. The solid line represents the unique neighbor of the first follower (agent 2) which is the leader (agent 1). The dashed lines represent all possible connections of the followers 2, 3, and 4.

Given a digraph $\mathcal{G}$, let $\xi_i \in \mathbb{R}^d (d \geq 2)$ denote the position and $v_i \in \mathbb{R}^d$ the velocity of each agent $i \in \mathcal{V}$, both expressed in an inertial frame common to all agents, such that $\dot{\xi}_i = v_i$. The stacked vector $\boldsymbol{\xi} = [\xi_1^\top, ..., \xi_n^\top]^\top \in \mathbb{R}^{dn}$ is called a configuration of $\mathcal{G}$ and the digraph $\mathcal{G}$ together with the configuration $\boldsymbol{\xi}$ define a formation $\mathcal{G}(\boldsymbol{\xi})$ in the d-dimensional space. Defining the relative position vectors

$$\xi_{ij} := \xi_j - \xi_i,\ i,\ j \in \mathcal{V},\ i \neq j \tag{4.2}$$

and as long as $\|\xi_{ij}\| \neq 0$, the bearing of agent j relative to agent i is given by the unit vector

$$g_{ij} := \xi_{ij}/\|\xi_{ij}\| \in \mathbb{S}^2. \tag{4.3}$$

Similarly to ξ_{ij}, define $v_{ij} := v_j - v_i$ as the relative velocity between agent i and j.

Definition 4.4. *A formation $\mathcal{G}(\boldsymbol{\xi}(t))$ is called bearing persistently exciting, if $\forall i \in V$, the matrices $\sum_{j \in \mathcal{N}_i} \pi_{g_{ij}(t)}$ satisfy the PE condition.*

The following Theorem shows that a leader-follower formation can be uniquely determined if it is bearing PE.

Theorem 4.1. *Consider a leader-follower formation. Assume that the leader's position $\xi_1(t)$, its velocity $v_1(t)$, the bearing vectors $\{g_{ij}(t)\}_{(i,j)\in\mathcal{E}}$, and the corresponding relative velocity vectors $\{v_{ij}(t)\}_{(i,j)\in\mathcal{E}}$ (equivalently $v_i(t)$) are well-defined, known, and bounded. Let $\hat{\xi}_1 \triangleq \xi_1$ and $\hat{\xi}_i$ denote the estimate of ξ_i, for $i = 2, \ldots, n$ with the following dynamics:*

$$\dot{\hat{\xi}}_i = v_i - K \sum_{j \in \mathcal{N}_i} \pi_{g_{ij}} (\hat{\xi}_i - \hat{\xi}_j),\ \forall i \geq 2, \tag{4.4}$$

with arbitrary initial conditions and K a positive definite matrix. Assume that the leader-follower formation is bearing persistently exciting. Then $\hat{\xi}_i$ converges uniformly globally exponentially (UGE) to the unique ξ_i.

Proof. Consider the error variables $\tilde{\xi}_i := \hat{\xi}_i - \xi_i$ defined for $i = 2, \ldots, n$ and the corresponding dynamics obtained from (4.4). For $i = 2$, we have $\mathcal{N}_2 = \{1\}$ and it is straightforward to verify that the dynamics of $\tilde{\xi}_2$ is given by

$$\dot{\tilde{\xi}}_2 = -K \pi_{g_{21}} \tilde{\xi}_2 \tag{4.5}$$

and that $\tilde{\xi}_2 = 0$ is UGE stable under the PE condition (by direct application of [LBHMS17, Lemma 4]). For $i = 3$ and $\mathcal{N}_3 = \{1\}$, the proof is exactly the same as for agent 2. For $\mathcal{N}_3 = \{2\}$ or $\{1,2\}$, the dynamics of $\tilde{\xi}_3$ can be written as

$$\dot{\tilde{\xi}}_3 = -K \sum_{j\in\mathcal{N}_3} \pi_{g_{3j}} \tilde{\xi}_3 + K\pi_{g_{32}} \tilde{\xi}_2 \tag{4.6}$$

which together with (4.5) forms a cascaded system with $\tilde{\xi}_2$ as input to (4.6). Using the fact that $\tilde{\xi}_2 = 0$ is UGE stable and system (4.6) is continuously differentiable and globally Lipschitz in $(\tilde{\xi}_3, \tilde{\xi}_2)$, it follows (by direct application of [LBHMS17, Proposition 1]) that $\tilde{\xi}_3 = 0$ is also UGE stable. In the general case, we can write

$$\dot{\tilde{\xi}}_i = -K \sum_{j\in\mathcal{N}_i} \pi_{g_{ij}} \tilde{\xi}_i + K \sum_{j\in\mathcal{N}_i\setminus\{1\}} \pi_{g_{ij}} \tilde{\xi}_j,$$

for $i = 2,\dots,n$ and the proof of that $\tilde{\xi}_i = 0$ is UGE stable can be obtained in a similar way. □

Remark 4.1. For the static case where $v_{ij} = 0$, $\forall (i,j) \in \mathcal{E}$, we obviously conclude that g_{21} is not PE. In that case, if each agent i ($i \geq 3$) has two neighbors $1 \leq j \neq k < i$ with $g_{ij} \neq \pm g_{ik}$, the leader-follower formation becomes exactly the same as the bearing rigid desired LFF formation described in [TZS⁺19] and uniqueness of the formation can still be guaranteed if, for instance, the distance $d_{21} = \|\xi_1 - \xi_2\|$ is provided. Under the proposed controller, which will be defined in the next section, the formation will converge to the desired shape up to a scaling factor as discussed in [TZS⁺19].

Note that under the condition of Theorem 4.1, the shape and the size of the bearing PE leader-follower formation may be time-varying. This includes similarity transformations (a combination of rigid transformation and scaling) involving a time-varying rotation. In this case, it is straightforward to show that for any bearing formation the bearing measurements are invariant to translation and scaling but change with rotation such that $g_{ij}(t) = R(t)^\top g_{ij}(0), \forall (i,j) \in \mathcal{E}$ (with $R(t) \in SO(d)$ the rotation part of the similarity transformation). This implies that there exists similarity transformations in which $R(t)$ is time-varying such that the leader-follower formation $\mathcal{G}(\boldsymbol{\xi}(t))$ is bearing PE.

Definition 4.5. *A leader-follower formation $\mathcal{G}(\boldsymbol{\xi}(t))$ is called relaxed bearing rigid if it is bearing PE and subjected to a similarity transformation.*

Corollary 4.1. *If the formation is relaxed bearing rigid, then the result of Theorem 4.1 applies.*

Proof. The proof is analogous to the proof of Theorem 4.1. It is omitted here for the sake of brevity. □

4.4 Bearing-only formation control for single-integrator dynamics

4.4.1 Problem formulation

Consider the formation $\mathcal{G}(\xi)$, where each agent $i \in \mathcal{V}$ is modelled as a single integrator with the following dynamics:

$$\dot{\xi}_i = v_i \tag{4.7}$$

recalling that $\xi_i \in \mathbb{R}^d$ is the position and $v_i \in \mathbb{R}^d$ the velocity input, all expressed in a common inertial frame. Let $\xi_i^*(t) \in \mathbb{R}^d$ and $v_i^*(t) \in \mathbb{R}^d$ denote the desired position and desired velocity of agent i, respectively. For any agent i ($i \geq 2$) and any agent j in its neighbor ($j \in \mathcal{N}_i$), define the desired relative position vector and desired bearing vector as ξ_{ij}^* and g_{ij}^* according to (4.2) and (4.3). We assume that the n-agent system satisfies the following assumptions.

Assumption 4.1. *The desired velocity $v_i^*(t)$ are bounded for all t. The desired positions $\xi_i^*(t)$ are such that the resulting desired bearings $g_{ij}^*(t)$ are well-defined for all t and the resulting desired formation satisfies the bearing PE condition.*

Assumption 4.2. *The sensing topology of the group is described by a digraph $\mathcal{G}(\mathcal{V}, \mathcal{E})$ that satisfies the leader-follower structure defined in Definition 4.3. Each agent $i \geq 2$ can measure the relative bearing vectors g_{ij} to its neighbors $j \in \mathcal{N}_i$.*

Assumption 4.3. *As the formation evolves in time, no inter-agent collisions and occlusions occur. In particular, we assume that the bearing information $g_{ij}(t)$, $(i, j) \in \mathcal{E}$ is all the time well-defined.*

With all these ingredients, we can define the bearing formation control problem as follows.

Problem 1. *Consider the system (4.7) and the underlying formation $\mathcal{G}(\xi)$. Under Assumptions 4.1-4.3, design stabilizing distributed control laws based on only bearing measurements that guarantee convergence to the desired formation.*

4.4.2 Exponential stabilization of the formations

For any agent i ($i \geq 2$) and any agent j in its neighbor ($j \in \mathcal{N}_i$), define the relative position error $\tilde{\xi}_{ij} := \xi_{ij} - \xi_{ij}^*$. Then the error dynamics is:

$$\dot{\tilde{\xi}}_{ij} = v_j - v_j^* - (v_i - v_i^*). \tag{4.8}$$

The following control law is proposed for each agent $i \in \mathcal{V}$

$$v_i = -\sum_{j \in \mathcal{N}_i} k_i \pi_{g_{ij}} \xi_{ij}^* + v_i^*, \tag{4.9}$$

where k_i is positive gains.

4.4.2.1 Stability and convergence of the first follower

Lemma 4.2. *Consider a n-agent ($n \geq 2$) system with a leader-follower interaction topology as specified in Definition 4.3. For the first follower ($i = 2$), consider the dynamics of the error* (4.8) *along with the control law* (4.9)*. If the Assumptions 4.1 - 4.3 are satisfied, then the equilibrium point $\tilde{\xi}_{21} = 0$ is exponentially stable (ES).*

Proof. The control law (4.9) for agent 1 is $v_1 = v_1^*$ and for agent 2 is $v_2 = -\pi_{g_{21}}\tilde{\xi}_{21} + v_2^*$. Recalling (4.8), the closed-loop system for the state $\tilde{\xi}_{21}$ is expressed as

$$\dot{\tilde{\xi}}_{21} = -k_2\pi_{g_{21}}\tilde{\xi}_{21}.$$

Consider the following Lyapunov function candidate:

$$\mathcal{L}_{21} = \frac{1}{2}\|\tilde{\xi}_{21}\|^2$$

Taking its time-derivative, it yields

$$\dot{\mathcal{L}}_{21} = -k_2\tilde{\xi}_{21}^\top\pi_{g_{21}}\tilde{\xi}_{21},$$

which is negative-semidefinite, one concludes that the state $\tilde{\xi}_{21}$ is bounded. Since $g_{21}^{*\top}\pi_{g_{21}}g_{21}^* = g_{21}^\top\pi_{g_{21}^*}g_{21}$, it is straightforward to verify that

$$\begin{aligned}\dot{\mathcal{L}}_{21} &= -k_2\xi_{21}^{*\top}\pi_{g_{21}}\xi_{21}^* \\ &= -k_2\frac{\|\xi_{21}^*\|^2}{\|\xi_{21}\|^2}\xi_{21}^\top\pi_{g_{21}^*}\xi_{21} \leq -k_2\gamma_2\tilde{\xi}_{21}^\top\pi_{g_{21}^*}\tilde{\xi}_{21}\end{aligned}$$

with $\gamma_2 = \frac{\min\|\xi_{21}^*(t)\|^2}{(\|\tilde{\xi}_{21}(0)\|+\max\|\xi_{21}^*(t)\|)^2}$. Using the PE condition of g_{21}^* along with a direct application of [LP02, Lemma 5] one can conclude that $\tilde{\xi}_{21} = 0$ is ES. □

Remark 4.2. Note that in the above lemma, assumption 4.3 relies on the evolution of state variables. This assumption serves here to show that if there is no collision or occlusion, the bearings are well-defined and the proposed control design yields the desired convergence properties (Lemma 4.2 and even in the following results: Lemma 4.3, 4.5 and Theorem 4.2, 4.3). Trying to more specifically characterize the set of initial conditions for which the system's solutions avoid collision and occlusion is out of the scope of the chapter.

4.4.2.2 Stability and convergence of the second follower

Lemma 4.3. *Consider a n-agent ($n \geq 3$) system with a leader-follower interaction topology as specified in Definition 4.3. For the second follower ($i = 3$), consider the dynamics of the error* (4.8) *along with the control law* (4.9)*. If the Assumptions 4.1-4.3 are satisfied and Lemma 4.2 is valid, then the equilibrium point $\tilde{\xi}_{3j} = 0$, $\forall j \in \mathcal{N}_3$ is ES.*

Proof. According to the leader-follower structure described in subsection 4.3, the second follower (agent 3) can have three possible sets of neighbors: $\mathcal{N}_3 = \{1\}$, $\mathcal{N}_3 = \{2\}$ and $\mathcal{N}_3 = \{1,2\}$.

Case i): $\mathcal{N}_3 = \{1\}$, the proof is identical to the proof of Lemma 4.2.

Case ii): $\mathcal{N}_3 = \{2\}$ or $\mathcal{N}_3 = \{1,2\}$. The closed-loop system for the state $\tilde{\xi}_{3j},\ j \in \mathcal{N}_3$ is expressed as

$$\dot{\tilde{\xi}}_{3j} = -\sum_{l \in \mathcal{N}_3} k_3 \pi_{g_{3l}} \tilde{\xi}_{3l} + v_j - v_j^*. \tag{4.10}$$

Since $v_1 = v_1^*$, v_2 is a function of variables $\tilde{\xi}_{21}$ and $\tilde{\xi}_{31} = \tilde{\xi}_{32} + \tilde{\xi}_{21}$, we can interpret (4.10) as a cascaded system that has $\tilde{\xi}_{21}$ as input to the unforced system

$$\dot{\tilde{\xi}}_{3j} = -k_3 \sum_{l \in \mathcal{N}_3} \pi_{g_{3l}} \tilde{\xi}_{3j}. \tag{4.11}$$

Now the proof becomes analogue to the proof of Lemma 4.2. Consider the following Lyapunov function candidate:

$$\mathcal{L}_{3j} = \frac{1}{2} \|\tilde{\xi}_{3j}\|^2,$$

and its time-derivative is given by

$$\dot{\mathcal{L}}_{3j} = -k_3 \tilde{\xi}_{3j}^\top \sum_{l \in \mathcal{N}_3} \pi_{g_{3l}} \tilde{\xi}_{3j}$$

which is negative-semidefinite. Thus state $\tilde{\xi}_{3j}$ is bounded. Due to the fact that $\tilde{\xi}_{3j} = \tilde{\xi}_{3k} + \tilde{\xi}_{kj},\ k \neq j,\ k,j \in \{1,2\}$ and $\tilde{\xi}_{21} = 0$ in the unforced system (4.11), one has $\tilde{\xi}_{3j} = \tilde{\xi}_{3k}$. It is straightforward to verify that

$$\begin{aligned} \dot{\mathcal{L}}_{3j} &= -k_3 \sum_{l \in \mathcal{N}_3} \frac{\|\xi_{3l}^*\|^2}{\|\xi_{3l}\|^2} \tilde{\xi}_{3l}^\top \pi_{g_{3l}^*} \tilde{\xi}_{3l} \\ &\leq -k_3 \gamma_3 \tilde{\xi}_{3j}^\top \sum_{l \in \mathcal{N}_3} \pi_{g_{3l}^*} \tilde{\xi}_{3j} \leq 0, \end{aligned}$$

with $\gamma_3 = \frac{\min_{l \in \mathcal{N}_j} \|\xi_{3l}^*\|^2}{(\|\tilde{\xi}_{3j}(0) + \max_{l \in \mathcal{N}_j} \|\xi_{3l}^*\|)^2}$. Using the PE condition along with direct application of [LP02, Lemma 5], we can conclude that the equilibrium point $\tilde{\xi}_{3j} = 0$, $j \in \mathcal{N}_3$ of the unforced system (4.11) is ES. This in turn implies that the equilibrium point $\tilde{\xi}_{3j} = 0,\ j \in \mathcal{N}_3$ is ES for the system (4.10). ☐

4.4.2.3 The *n*-agents system

Theorem 4.2. *Consider a n-agent ($n \geq 2$) system with a leader-follower interaction topology as specified in Definition 4.3. For all agents $i \in \mathcal{V} \backslash \{1\}$, consider the system (4.8) in closed-loop with the proposed control law (4.9). If the Assumptions 4.1-4.3 are satisfied, then the equilibrium point $\tilde{\xi}_{ij} = 0,\ i = 2, \ldots, n,\ \forall j \in \mathcal{N}_i$ is ES.*

Proof. We will prove the convergence of $\tilde{\xi}_{ij} = 0$ by mathematical induction. Firstly, for $i = 2$ we have $\tilde{\xi}_{21} = 0$ is ES based on Lemma 4.2. Thus Theorem 4.2 is true for $i = 2$. It is also true for $i = 3$ from the conclusion of Lemma 4.3.

Secondly, we suppose Theorem 4.2 is true for $4 \leq k \leq i-1$, that is $\tilde{\xi}_{kj} = 0$, $\forall j \in \mathcal{N}_k$ is ES for all $4 \leq k \leq i-1$ and we will prove that it is also true for $k = i$. Recall (4.8), the closed-loop system for the states $\tilde{\xi}_{ij}$, $j \in \mathcal{N}_i$ is represented as

$$\dot{\tilde{\xi}}_{ij} = -k_i \pi_{g_{ij}} \tilde{\xi}_{ij} - \sum_{q \in \mathcal{N}_i \backslash \{j\}} k_i \pi_{g_{iq}} \tilde{\xi}_{iq} + v_j - v_j^*, \tag{4.12}$$

where v_j is a function of variables $\tilde{\xi}_{jm}$, $m \in \mathcal{N}_j$ and $\tilde{\xi}_{iq} = \tilde{\xi}_{ij} + \tilde{\xi}_{jq}$. Note that since the graph is connected, $\tilde{\xi}_{jq}$ can be represented by the error variables $\tilde{\xi}_{km}$, $2 \leq k \leq i-1$, $m \in \mathcal{N}_k$. System (4.12) can then be considered as a cascaded system with $\tilde{\xi}_{km}$, $2 \leq k \leq i-1$, $m \in \mathcal{N}_k$, being inputs of the unforced system analogously to system (4.11). Using a similar argument as shown in Lemma 4.3, one can conclude that the equilibrium point $\tilde{\xi}_{ij} = 0$, $\forall j \in \mathcal{N}_i$ of the unforced system is ES. Because Theorem 4.2 is true for $2 < k \leq i-1$, we can conclude that the equilibrium point $\tilde{\xi}_{ij} = 0$, $\forall j \in \mathcal{N}_i$ for system (4.12) is also ES. This in turn implies that Theorem 4.2 is true for $k = i$. Then, by mathematical induction, if follows that the claim is true for all $k \in \mathcal{V} \backslash \{1\}$.

□

It is worth to notice that the exponential stabilization of the equilibrium $\tilde{\xi}_{ij}^\top = 0$, $\forall (i,j) \in \mathcal{E}$ implies the exponential stabilization of the formation to the desired one in terms of shape and scale only. This is inherent to the problem at hand since only relative measurements are involved in the control design. However, by exploiting the cascade structure of the formation dynamics, it is straightforward to verify that the exponential stabilization of the formation in the configuration space (that is $\xi_i \rightarrow \xi_i^*$) can be directly deduced if the leader has access to its own position.

4.5 Bearing formation control for double-integrator dynamics

In this section we will extend the bearing formation control law for a multi-agent system with double-integrator dynamics. Consider the formation $\mathcal{G}(\xi)$, where each agent $i \in \mathcal{V}$ is more realistically modeled as double integrator with the following dynamics:

$$\begin{cases} \dot{\xi}_i = v_i \\ \dot{v}_i = u_i \end{cases} \tag{4.13}$$

where $u_i \in \mathbb{R}^d$ is the acceleration control input expressed in the inertial frame. Let $u_i^*(t) \in \mathbb{R}^d$ denote the desired acceleration of agent i. Define the desired relative velocity vector as $v_{ij}^* = v_j^* - v_i^*$, $i, j \in \mathcal{V}$, $i \neq j$.

We assume that the n-agent system satisfies the following assumptions.

Assumption 4.4. *The desired acceleration $u_i^*(t)$ and the desired relative velocity $v_{ij}^*(t)$ are bounded for all $t > 0$, the resulting desired bearings $g_{ij}^*(t)$ are well-defined for all $t > 0$ and the desired formation is bearing PE.*

Assumption 4.5. *The sensing topology of the group is described by a digraph $\mathcal{G}(\mathcal{V},\mathcal{E})$ that satisfies the leader-follower structure defined in Definition 4.3. Each agent $i \geq 2$ can measure the relative velocity v_{ij} and relative bearing vectors g_{ij} to its neighbors $j \in \mathcal{N}_i$.*

With all these ingredients, we can define the bearing formation control problem as follows.

Problem 2. *Consider the system (4.13) and the formation $\mathcal{G}(\xi)$. Under Assumptions 4.3 - 4.5, design stabilizing distributed control laws based on bearing and relative velocity measurements that guarantee exponential stabilization of the formation in terms of shape and scale to the desired one.*

For any agent i ($i \geq 2$) and any agent j in its neighbor ($j \in \mathcal{N}_i$), we define the relative position error $\tilde{\xi}_{ij} := \xi_{ij} - \xi_{ij}^*$ and the relative velocity error $\tilde{v}_{ij} := \dot{\tilde{\xi}}_{ij} = (v_j - v_i) - (v_j^* - v_i^*)$ along with the following dynamics:

$$\begin{cases} \dot{\tilde{\xi}}_{ij} = \tilde{v}_{ij} \\ \dot{\tilde{v}}_{ij} = u_j - u_j^* - (u_i - u_i^*). \end{cases} \tag{4.14}$$

Consider the following control law for each agent $i \in \mathcal{V}$

$$u_i = \sum_{j \in \mathcal{N}_i} [-k_{p_i} \pi_{g_{ij}} \xi_{ij}^* + k_{d_i} \tilde{v}_{ij}] + u_i^*, \tag{4.15}$$

where k_{d_i} and k_{p_i} are positive gains that satisfy $k_{d_i} > \frac{1}{m_i}$ and $k_{p_i} < \frac{4}{m_i} - \frac{4}{k_{d_i}^2 m_i^3}$ (recall that $m_i = |\mathcal{N}_i|$). For $i \in \mathcal{V}\backslash\{1\}$, define new variables $\tilde{x}_{ij} := (\tilde{\xi}_{ij}^\top, \tilde{v}_{ij}^\top)^\top$, $j \in \mathcal{N}_i$ and the following matrices to be used later in the stability analysis:

$$A_i(g_i) = \begin{bmatrix} 0 & -I_d \\ k_{p_i} \sum\limits_{l \in \mathcal{N}_i} \pi_{g_{il}} & k_{d_i} m_i I_d \end{bmatrix},\ P_i := \frac{1}{2} \begin{bmatrix} I_d & \frac{1}{k_{d_i} m_i} I_d \\ \frac{1}{k_{d_i} m_i} I_d & I_d \end{bmatrix} > 0,\ \Sigma_i = \begin{bmatrix} \sum\limits_{j \in \mathcal{N}_i} \pi_{g_{ij}^*} & 0 \\ 0 & I_d \end{bmatrix} \geq 0 \tag{4.16}$$

and

$$Q_i(g_i) = \sum_{j \in \mathcal{N}_i} \begin{bmatrix} \frac{k_{p_i}}{k_{d_i} m_i} \pi_{g_{ij}} & \frac{k_{p_i}}{2} \pi_{g_{ij}} \\ \frac{k_{p_i}}{2} \pi_{g_{ij}} & (k_{d_i} - \frac{1}{k_{d_i} m_i^2}) I_d \end{bmatrix} = \sum_{j \in \mathcal{N}_i} S_{ij} M_{ij} S_{ij} \geq 0, \text{ with } S_{ij} = \begin{bmatrix} \pi_{g_{ij}} & 0 \\ 0 & I_d \end{bmatrix} \text{ and } M_{ij} = \begin{bmatrix} \frac{k_{p_i}}{k_{d_i} m_i} I_d & \frac{k_{p_i}}{2} I_d \\ \frac{k_{p_i}}{2} I_d & (k_{d_i} - \frac{1}{k_{d_i} m_i^2}) I_d \end{bmatrix} \tag{4.17}$$

where the matrices argument g_i stands for the concatenation of all bearing vectors g_{ij}, $\forall j \in \mathcal{N}_i$.

4.5.1 Stability and convergence of the first follower

Lemma 4.4. *Consider a n-agent ($n \geq 2$) system with a leader-follower interaction topology as specified in Definition 4.3. For the first follower ($i = 2$), consider the error dynamics (4.14) along with the control law (4.15). If Assumptions 4.3 - 4.5 are satisfied, then the equilibrium point $\tilde{x}_{21} = (\tilde{\xi}_{21}^\top, \tilde{v}_{21}^\top)^\top = 0$ is exponentially stable (ES).*

Proof. Recalling (4.14) and (4.15), the closed-loop system for the state $\tilde{x}_{21}$ is expressed as

$$\dot{\tilde{x}}_{21} = -A_2(g_2(t))\tilde{x}_{21}.$$

Consider the following Lyapunov function candidate:

$$\mathcal{L}_{21} = \tilde{x}_{21}^{\top} P_2 \tilde{x}_{21}.$$

Taking its time-derivative yields

$$\dot{\mathcal{L}}_{21} = -\tilde{x}_{21}^{\top} Q_2 \tilde{x}_{21}.$$

which is negative-semi definite since $Q_2 \geq 0$. Hence, we conclude that $\tilde{x}_{21}$ is bounded. Recalling (4.17) and using the fact ${g_{21}^*}^{\top} \pi_{g_{21}} g_{21}^* = {g_{21}}^{\top} \pi_{g_{21}^*} g_{21}$, one concludes

$$\dot{\mathcal{L}}_{21} = -\tilde{x}_{21}^{\top} S_{21} M_{21} S_{21} \tilde{x}_{21} \leq -\gamma_2 \tilde{x}_{21}^{\top} \Sigma_2 \tilde{x}_{21} \leq 0,$$

where

$$\gamma_2 = \frac{k_{p_2}(k_{d_2} - k_{p_2} k_{d_2}^2/4 - 1)}{k_{d_2}(k_{p_2} + k_{d_2} - 1)} \min \alpha_2^2(t) > 0$$

with $\min \alpha_2^2(t) = \min \frac{\|\xi_{21}^*(t)\|^2}{\|\xi_{21}(t)\|^2}$. Now, since $\mathcal{L}_{21}$ is decreasing, one can verify that

$$\min \alpha_2^2(t) \geq \left(1 - \frac{\sqrt{\frac{\lambda_{\max}(P_2)}{\lambda_{\min}(P_2)}}\|\tilde{x}_{21}(0)\|}{(\sqrt{\frac{\lambda_{\max}(P_2)}{\lambda_{\min}(P_2)}}\|\tilde{x}_{21}(0)\| + \max\|\xi_{21}^*(t)\|)}\right)^2 > 0.$$

From (4.17) along with the PE condition of g_{21}^*, one ensures that condition (1) of Theorem B.1 in the appendix is satisfied. By a direct application of Lemma B.3 (see appendix) one can conclude that condition (2) of Theorem B.1 is also satisfied. This in turn implies that $\tilde{x}_{21} = 0$ is ES. ☐

4.5.2 Stability and convergence of the second follower

Lemma 4.5. *Consider a n-agent ($n \geq 3$) system with a leader-follower interaction topology as specified in Definition 4.3. For the second follower ($i = 3$), consider the error dynamics (4.14) along with the control law (4.15). If the Assumptions 4.3 - 4.5 are satisfied and Lemma 4.4 is valid, then the equilibrium point $\tilde{x}_{3j} = (\tilde{\xi}_{3j}^{\top}, \tilde{v}_{3j}^{\top})^{\top} = 0$, $\forall j \in \mathcal{N}_3$ is ES.*

Proof. According to the leader-follower structure described in Definition 4.3, the second follower (agent 3) can have three possible sets of neighbors: $\mathcal{N}_3 = \{1\}$, $\mathcal{N}_3 = \{2\}$ and $\mathcal{N}_3 = \{1, 2\}$.

Case i): $\mathcal{N}_3 = \{1\}$, the proof is identical to the proof of Lemma 4.4.

Case ii): $\mathcal{N}_3 = \{2\}$ or $\mathcal{N}_3 = \{1, 2\}$. Since $\tilde{x}_{31} = \tilde{x}_{32} + \tilde{x}_{21}$, the closed-loop system for the states $\tilde{x}_{3j}$, $j \in \mathcal{N}_3$ is expressed as

$$\dot{\tilde{x}}_{3j} = -A_3(g_3(t))\tilde{x}_{3j} + B_{21}(g_3(t), g_2(t))\tilde{x}_{21} \tag{4.18}$$

where A_3 is defined in (4.16) and B_{21} is a bounded function. We can interpret (4.18) as a cascaded system that has $\tilde{x}_{21}$ as input to the unforced system

$$\dot{\tilde{x}}_{3j} = -A_3(g_3(t))\tilde{x}_{3j}. \tag{4.19}$$

Now the proof becomes analogous to the proof of Lemma 4.4. By direct application of Theorem B.1, one concludes that the equilibrium $\tilde{x}_{3j} = 0,\ j \in \mathcal{N}_3$ of the unforced system (4.19) is ES. Since the matrix valued function B_{21} is bounded and $\tilde{x}_{21} = 0$ is ES, this implies that the equilibrium point $\tilde{x}_{3j} = 0,\ j \in \mathcal{N}_3$ is ES for the system (4.18). $\square$

4.5.3 The n-agent system

Theorem 4.3. *Consider a n-agent ($n \geq 2$) system with a leader-follower interaction topology as specified in Definition 4.3. For all agents $i \in \mathcal{V}\backslash\{1\}$, consider the system (4.14) along with the proposed control law (4.15). If Assumptions 4.3 - 4.5 are satisfied, then the equilibrium point $\tilde{x}_{ij} = (\tilde{\xi}_{ij}^\top, \tilde{v}_{ij}^\top)^\top = 0$ is ES, $\forall i \in \mathcal{V}\backslash\{1\}$ and $\forall j \in \mathcal{N}_i$.*

Proof. We will prove the convergence of $\tilde{x}_{ij} = 0$ by mathematical induction. Firstly, for $i = 2$ and $i = 3$ the conclusion that $\tilde{x}_{ij} = 0$ is ES $\forall j \in \mathcal{N}_i$ follows directly from Lemma 4.4 and Lemma 4.5, respectively. Secondly, we suppose that $\tilde{x}_{kj} = 0$ is ES, $\forall j \in \mathcal{N}_k$ and $\forall 4 \leq k \leq i-1$ then, we show that it is also true for $k = i$. Using the fact that $\forall q \in \mathcal{N}_i$, one has $\tilde{x}_{iq} = \tilde{x}_{ij} + \tilde{x}_{jq}$ with $j \in \mathcal{N}_i, j \neq q$ and $\tilde{x}_{jq}$ can be expressed in terms of the error variables $\tilde{x}_{km},\ 2 \leq k \leq i-1,\ m \in \mathcal{N}_k$ because the graph is connected, the closed-loop system for the states $\tilde{x}_{ij},\ j \in \mathcal{N}_i$ can be represented as

$$\dot{\tilde{x}}_{ij} = -A_i(g_i(t))\tilde{x}_{ij} + \sum_{2 \leq k \leq i-1,\ m \in \mathcal{N}_k} B_{km}(g_i(t), g_k(t))\tilde{x}_{km} \tag{4.20}$$

where A_i is defined in (4.16) and B_{km} is a bounded matrix valued function. Thus system (4.20) can be considered as a cascaded system with $\tilde{x}_{km},\ 2 \leq k \leq i-1,\ m \in \mathcal{N}_k$ perturbing the unforced system $\dot{\tilde{x}}_{ij} = -A_i(g_i(t))\tilde{x}_{ij}$. From there and analogously to Lemma 4.4 and 4.5, one concludes that $\tilde{x}_{ij} = 0$ is ES for the unforced system and because the error variables $\tilde{x}_{km} = 0$ are ES and B_{km} is bounded, $\tilde{x}_{ij} = 0$ is also ES for system (22). Then, by mathematical induction, it follows that the claim is true for all $i \in \mathcal{V}\backslash\{1\}$, which concludes the proof. $\square$

Proposition 4.1. *Consider the cascaded system defined in Theorem 4.3. If Assumptions 4.3 - 4.5 are satisfied and the convergence rate of the unforced system $\dot{\tilde{x}}_{ij} = -A(g_i(t))\tilde{x}_{ij}$ is greater than b_i, for each agent $i \in \mathcal{V}\backslash\{1\}$ and $j \in \mathcal{N}_i$. Then the convergence rate for each agent $i \in \mathcal{V}\backslash\{1,2\}$ of the cascaded system is greater than $c_i = \frac{1}{2}\min\{c_{i-1}, b_i\}$, with $c_2 = b_2$, which is a lower bound obtained when the leader-follower structure is minimal and has a single directed path. Additionally, if $b_i = b$, the convergence rate for each agent $i \in \mathcal{V}\backslash\{1,2\}$ in the cascaded system is greater than $\frac{b}{2^{i-2}}$.*

Proof. Using the same argument used in the proof of [Kha92, Theorem 4.9] and by mathematical induction, the convergence rate for each agent $i \in \mathcal{V}\backslash\{1,2\}$ in the cascaded form is greater than

$c_i = \frac{1}{2}\min\{c_{i-1}, b_i\}$. When $b_i = b$, the conclusion follows by iterative substitution of c_{i-1} in the expression for c_i. $\square$

4.6 Simulation Results

In this section, we consider a four-agent system with double-integrator dynamics defined in $\mathbb{R}^3$. The underlying graph topology is a minimal leader-follower graph formed by a single directed path, that is, each follower has only one neighbor such that $\mathcal{N}_i = \{i-1\}$, $i \in \mathcal{V}\backslash\{1\}$, $\mathcal{V} = \{1,2,3,4\}$. For the sake of simplicity, the leader (agent 1) is static at position $\xi_1 = [0\ 0\ 0]^\top$. According to Assumption 4.4, the desired trajectories for the followers are chosen such that $\xi_i^*(t) = R(t)^\top \xi_i^*(0)$, with $R(t) = \begin{bmatrix} \cos(\frac{t}{2.5}) & -\sin(\frac{t}{2.5}) & 0 \\ \sin(\frac{t}{2.5}) & \cos(\frac{t}{2.5}) & 0 \\ 0 & 0 & 1 \end{bmatrix}$, $\xi_2^*(0) = [0\ 1\ 0]^\top, p_3^*(0) = [\frac{\sqrt{3}}{2}\ \frac{1}{2}\ 0]^\top$ and $\xi_4^*(0) = [\frac{1}{2}\ \frac{\sqrt{3}}{2}\ 1]^\top$, which form a pyramid in $\mathbb{R}^d$ that rotates about z-axis (see Fig. 4.3). Note that the desired formation is not bearing rigid but relaxed bearing rigid. The initial conditions are $\xi_2(0) = [-1\ 2\ 1]^\top$, $v_2(0) = [0\ 1\ 0]^\top$, $\xi_3(0) = [-2\ -1\ -1]^\top$, $v_3(0) = [1\ 0\ 0]^\top, \xi_4(0) = [-0.5\ -0.5\ 1]^\top$ and $v_4(0) = [1\ 0\ -1]^\top$. The controller gains are chosen as follows $k_{p_i} = 3$ and $k_{d_i} = 10, \forall i \in \mathcal{V}\backslash\{1\}$, to ensure a fast convergence rate according to Theorem B.1 while ensuring that inequalities $k_{d_i} > 1$ and $k_{p_i} < 4 - \frac{4}{k_{d_i}^2}$ are satisfied. The left hand side of Fig. 4.3 shows the time evolution of the error states $\|\tilde{x}_{21}\|$, $\|\tilde{x}_{32}\|$ and $\|\tilde{x}_{43}\|$, respectively. It also confirms the result of Proposition 4.1 that due to the cascade structure of the system the convergence of $\tilde{x}_{21}(t)$ is the fastest and of $\tilde{x}_{43}(t)$ is the slowest one. The right hand side of Fig. 4.3 shows the 3-D time evolution of the formation converging to the desired one. It also validates the fact that the proposed control law stabilizes the formation without requiring bearing rigidity (additional simulation results with animations can be found in `https://youtu.be/fwv4Q_3xCWw`).

4.7 Conclusion

This chapter studies bearing formation control problem of a leader-follower structure under time-varying desired formation and introduces the new concept of relaxed bearing rigidity. The proposed controller ensures, a (local) exponential stability of the formation as long as the bearing PE conditions are met on the desired formation. Simulation results are provided to validate the control strategy.

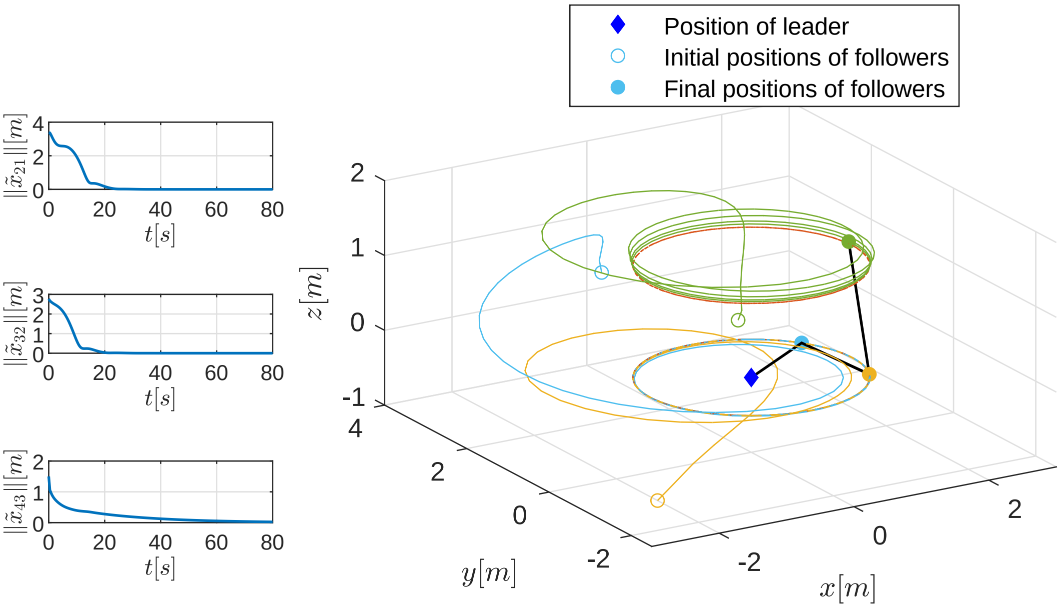

Figure 4.3: Evolutions of error states (left hand side) and 3-D trajectories (right hand side) for a pyramid formation under a minimal leader-follower structure: the colored solid lines represent the agents' trajectories, the dashed red lines represent the desired trajectories and the black solid lines represent the connections between agents.

5

RELAXED BEARING RIGIDITY AND BEARING FORMATION CONTROL UNDER PERSISTENCE OF EXCITATION

5.1 Introduction

In this chapter, we provide a coherent generalization of our previous solution presented in Chapter 4 to formations under general undirected graph topologies. A general concept of bearing persistently exciting (BPE) formation defined in d ($d \geq 2$)-dimensional space, is fully developed for the first time in this chapter. We extend the results by providing conditions on BPE formation leading to the definition of the relaxed bearing rigidity theory which connects bearing persistence of excitation (BPE) with bearing rigidity and guarantees the uniqueness of a fixed geometric pattern without imposing bearing rigid conditions on the graph topology. Based on the proposed BPE theory, we design control laws for a multi-agent system (with both single- or double-integrator dynamics) to track a BPE desired formation using only bearing measurements (also velocity measurements for double-integrator dynamics). In particular, we show that under the BPE condition exponential stabilization of the formation up to a translation is achieved for any undirected graph that has a spanning tree (not necessarily bearing rigid, as shown in Fig. 5.1-($a1$), ($b1$) and ($b2$) and Fig. 5.2-($a1$), ($b1$), ($b2$), ($c1$) and (c_2)). This implies the scale ambiguity, which is a characteristic of bearing rigidity, can be removed and convergence of the desired formation in terms of scale can be guaranteed, without the need to measure the distance between any two agents. Finally we provide a safe set for the initial conditions that guarantees collision avoidance for the multi-agent system under both single- and double-integrator dynamics.

This chapter is organized as follows. Section 5.2 introduces the preliminaries about formation control under undirected graphs. Section 5.3 introduces the bearing persistent excitation theory. Section 5.4 presents the bearing formation control law along with stability analysis. Section 5.6 shows the performance of the proposed control strategy in two different scenarios.

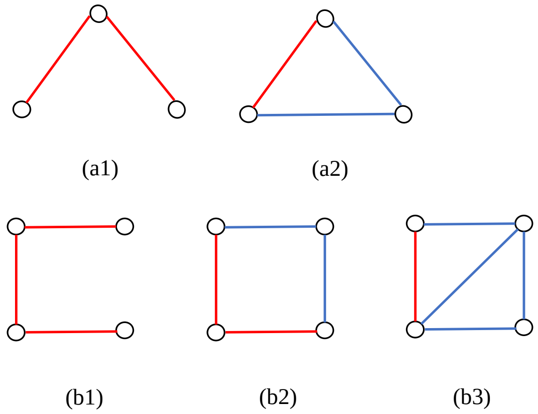

Figure 5.1: Examples of bearing persistently exciting formations in two-dimensional space. Red lines represent edges for which the corresponding bearing vector are persistently exciting and blue lines represent edges for which the corresponding bearing vectors are not necessarily persistently exciting.

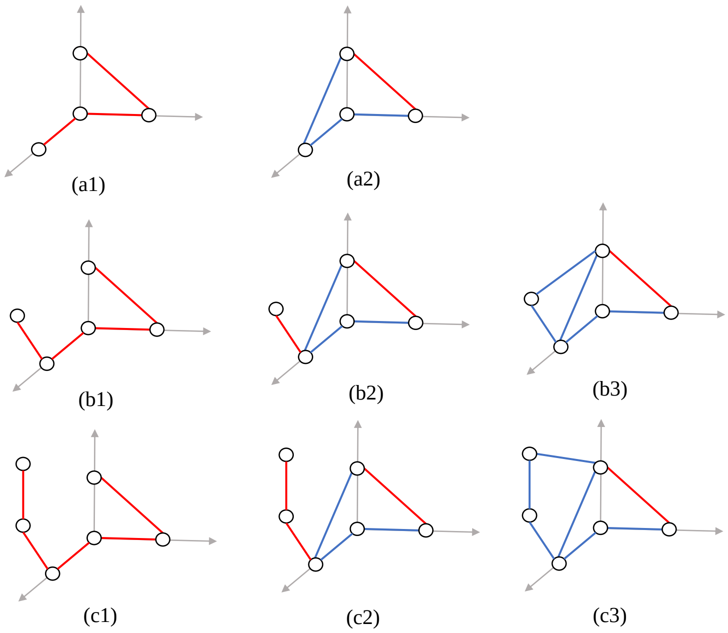

Figure 5.2: Examples of bearing persistently exciting formations in three-dimensional space. Red lines represent edges for which the corresponding bearing vector are persistently exciting and blue lines represent edges for which the corresponding bearing vectors are not necessarily persistently exciting.

The chapter concludes with some final comments in Section 5.7.

5.2 Preliminaries

5.2.1 Undirected graph topologies

Consider a system of n connected agents. The underlying interaction topology can be modeled as an undirected graph $\mathcal{G} := (\mathcal{V}, \mathcal{E})$, where $\mathcal{V} = \{1, \ldots, n\}$ $(n \geq 2)$ is the set of vertices and $\mathcal{E} \subseteq \mathcal{V} \times \mathcal{V}$ is the set of undirected edges. Two vertices i and j are called adjacent (or neighbors) when $\{i, j\} \in \mathcal{E}$. The set of neighbors of agent i is denoted by $\mathcal{N}_i := \{j \in \mathcal{V} | \{i, j\} \in \mathcal{E}\}$. If $j \in \mathcal{N}_i$, it follows that $i \in \mathcal{N}_j$, since the edge set in an undirected graph consists of unordered vertex pairs. Define $\mathring{m} = |\mathcal{E}|$, where $|.|$ denotes the cardinality of a set. A graph $\mathcal{G}$ is connected if there exists a path between every pair of vertices in $\mathcal{G}$ and in that case $\mathring{m} \geq n - 1$. A graph $\mathcal{G}$ is said to be acyclic if it has no circuits. A tree is a connected acyclic graph. A spanning tree of a graph $\mathcal{G}$ is a tree of $\mathcal{G}$ involving all the vertices of $\mathcal{G}$. An orientation of an undirected graph is the assignment of a direction to each edge. An oriented graph is an undirected graph together with an orientation. The incidence matrix $H \in \mathbb{R}^{\mathring{m} \times n}$ of an oriented graph is the $\{0, \pm 1\}$-matrix with rows indexed by edges and columns by vertices: $[H]_{ki} = 1$ if vertex i is the head of the edge k, $[H]_{ki} = -1$ if it is the tail, and $[H]_{ki} = 0$ otherwise. For a connected graph, one always has $H\mathbf{1}_n = 0$ and $\operatorname{rank}(H) = n - 1$.

5.2.2 Formation control

Consider a undirected graph $\mathcal{G} = (\mathcal{V}, \mathcal{E})$, let $\xi_i \in \mathbb{R}^d$ and $v_i \in \mathbb{R}^d$, $(d \geq 2)$ denote the position and velocity, respectively, of each agent $i \in \mathcal{V}$ both expressed in a common inertial frame. Recall that the stacked vector $\boldsymbol{\xi} = [\xi_1^\top, ..., \xi_n^\top]^\top \in \mathbb{R}^{dn}$ $(n \geq 2)$ is a configuration of $\mathcal{G}$. Let $\boldsymbol{v} := \dot{\boldsymbol{\xi}} = [v_1^\top, \ldots, v_n^\top]^\top \in \mathbb{R}^{dn}$. For a formation, define the relative position

$$\xi_{ij} := \xi_j - \xi_i, \ \{i, j\} \in \mathcal{E}, \tag{5.1}$$

as long as $\|\xi_{ij}\| \neq 0$, the bearing of agent j relative to agent i is given by the unit vector

$$g_{ij} := \xi_{ij} / \|\xi_{ij}\| \in \mathbb{S}^{d-1}. \tag{5.2}$$

Consider an arbitrary orientation of the graph and denote

$$\bar{\xi}_k := \xi_{ij}, \ k \in \{1, \ldots, \mathring{m}\},$$

as the edge vector with assigned direction such that i and j are, respectively, the initial and the terminal nodes of $\bar{\xi}_k$. Denote the corresponding bearing vector by

$$\bar{g}_k := \frac{\bar{\xi}_k}{\|\bar{\xi}_k\|} \in \mathbb{S}^{d-1}, \ k \in \{1, \ldots, \mathring{m}\}.$$

Define the stacked vector of edge vectors $\bar{\boldsymbol{\xi}} = [\bar{\xi}_1^\top, ..., \bar{\xi}_{\mathring{m}}^\top]^\top = \bar{H}\boldsymbol{\xi}$, where $\bar{H} = H \otimes I_d$.

5.2.2.1 Formation control using relative position measurements

In this problem setup, the agents sense relative positions of their neighbors. The formation control objective is to drive the configuration ξ to the desired one up to translation, i.e. [ME10, OPA15]. The graph Laplacian matrix is introduced as

$$L = \bar{H}^\top \bar{H} \tag{5.3}$$

Note that if the graph is connected, or equivalently has a spanning tree, $\text{rank}(L) = dn - d$, $\text{Null}(L) = \text{span}\{U\}$, where $U = \mathbf{1}_n \otimes I_d$. Let λ_i denote the ith eigenvalue of L under a non-increasing order and note that λ_{dn-d} is the smallest positive eigenvalue of L.

5.2.2.2 Formation control using bearing measurements

In this setting, the agents measure the relative directions to their neighbors (bearings) and the objective of the formation control is to drive the configuration ξ to the desired configuration up to a translational and a scaling factor, i.e. [ZZ16, ZLD19]. The bearing Laplacian matrix is introduced as

$$L_B(\xi(t)) = \bar{H}^\top \Pi \bar{H} \tag{5.4}$$

where $\Pi = \text{diag}\left(\pi_{\bar{g}_k}\right)$. Since $\text{span}\{U, \xi\} \subset \text{Null}(L_B)$ it follows that $\text{rank}(L_B) \leq dn - d - 1$. According to [ZZ16] (in which only constant bearing are considered), if the formation is infinitesimally bearing rigid then $\text{rank}(L_B) = dn - d - 1$ and $\text{Null}(L_B) = \text{span}\{U, \xi\}$.

5.3 Bearing persistence of excitation in $\mathbb{R}^d$

In this section, we derive conditions under which a formation $\mathcal{G}(\xi)$ (defined in Section 5.2.2) can be uniquely determined up to a translational factor using only bearing and velocity measurements. The main contributions with respect to the literature is to lift the scale ambiguity introduced by bearings and also relax the constraints on graph topology required by bearing rigidity theory [ZZ16]. Figures 5.1 and 5.2 illustrate this relaxation with formations $(a1)$, $(b1)$ and $(b2)$ in Fig. 5.1 and $(a1)$, $(b1)$, $(b2)$, $(c1)$ and $(c2)$ in Fig. 5.2 that are not bearing rigid, but can be uniquely determined up to a translation vector provided that specific bearing vectors are persistently exciting. We will illustrate the results in the following subsections.

5.3.1 BPE formation and relaxed bearing rigidity

In this subsection, we define the BPE formation and introduce the new concept of *relaxed bearing rigidity*. We first introduce a relaxed persistence of excitation condition specifically developed for the bearing Laplacian matrix.

Definition 5.1. *Consider the Laplacian* L *and the bearing Laplacian* L_B *defined in* (5.3) *and* (5.4)*, respectively. The bearing Laplacian matrix is called persistently exciting (PE) if for all* t *there exists* $T > 0$ *and* $0 < \mu < 1$ *such that*

$$\frac{1}{T}\int_t^{t+T} L_B(\xi(\tau))d\tau \geq \mu L. \tag{5.5}$$

Remark 5.1. One can verify that the PE condition for the bearing Laplacian introduced in Definition 5.1 is less restrictive than the PE condition on the bearing matrix Π in (5.4) from Definition 4.1. In particular, having a matrix Π that is PE is a sufficient but not necessary condition to ensure that $L_B = \bar{H}^\top \Pi \bar{H}$ is also PE.

Definition 5.2. *A formation* $\mathcal{G}(\xi(t))$ *is bearing persistently exciting (BPE) if* $\mathcal{G}$ *has a spanning tree and its bearing Laplacian matrix is PE.*

The following Theorem will show that a BPE formation can be uniquely determined up to a translation using only bearing and velocity measurements.

Theorem 5.1. *Consider a formation* $\mathcal{G}(\xi(t))$ *defined in* $\mathbb{R}^d$ *along with bearing measurements* $\{\bar{g}_k\}_{k\in\{1\ldots\mathring{m}\}}$ *of an arbitrary orientation of the graph. Assume that the velocity measurements* $\{v_i\}_{i\in\{1\ldots n\}}$ *are bounded and known. If* $\mathcal{G}(\xi(t))$ *is BPE then the configuration* $\xi(t)$ *can be recovered up to a translational vector in* $\mathbb{R}^d$*.*

Proof. Consider the stacked velocity vector $\boldsymbol{v}(t) = [v_1^\top(t),\ldots,v_n^\top(t)]^\top \in \mathbb{R}^{dn}$ and let $\hat{\xi}$ denote the estimate of ξ with dynamics:

$$\dot{\hat{\xi}} = \boldsymbol{v} - L_B(\xi(t))\hat{\xi}, \tag{5.6}$$

with arbitrary initial conditions. Define the relative centroid $c_0(t) := \frac{1}{n}U^\top(\hat{\xi}(t) - \xi(t)) \in \mathbb{R}^d$ and recall that $U = \mathbf{1}_n \otimes I_d$, $U^\top L_B = 0$, and $L_B U = 0$. Since $\dot{c}_0 \equiv 0$, c_0 is constant, that is, $c_0(t) = \frac{1}{n}U^\top(\hat{\xi}(0) - \xi(0))$. Consider the error variable $\zeta(t)$ defined such that $\hat{\xi}(t) - \xi(t) = \zeta(t) + Uc_0$ and $\zeta(t)$ and Uc_0 are orthogonal. Then, the corresponding dynamics can be obtained from (5.6):

$$\dot{\zeta} = -L_B(\xi(t))\zeta. \tag{5.7}$$

Since the formation is BPE, $\forall x \in \mathbb{R}^{dn-d}$ satisfying $U^\top x \equiv 0$, there exists a $T > 0$ and $0 < \mu < 1$ such that, $\forall t$, $\frac{1}{T}x^\top \int_t^{t+T} L_B(\xi(\tau))d\tau x \geq \mu x^\top \bar{H}^\top \bar{H} x \geq \mu\lambda_{dn-d}\,\|x\|^2$, where $\lambda_{dn-d} > 0$ is the smallest positive eigenvalue of $\bar{H}^\top\bar{H}$ (see Sect. 5.2.2.1). Using similar arguments as in the proof of [LP02, Lemma 5], one can ensure that the equilibrium $\zeta = 0$ is uniformly globally exponentially (UGE) stable. Therefore, one concludes that $\hat{\xi}$ converges UGE to the unique ξ up to a translational vector Uc_0. ☐

Remark 5.2. The concept of BPE formation implying time-varying dynamics is general. It also includes similarity transformations (a combination of rigid transformation and scaling) involving a time-varying rotation. That is, $\forall t > 0, \forall i \in \mathcal{V},\ \xi_i(t) = s(t)R(t)^\top \xi_i(0) + c(t)$, with $s(t) \in \mathbb{R}^+, c(t) \in \mathbb{R}^d$ and $R(t) \in SO(d)$ a rotation matrix. In this case, it is straightforward to show that for any bearing formation the bearing measurement g_{ij} is such that $g_{ij}(t) = R(t)^\top g_{ij}(0),\ \forall (i,j) \in \mathcal{E}$ is invariant to translation and scaling and consequently provides naturally a relaxed bearing rigid property for BPE formations.

Definition 5.3. *A formation $\mathcal{G}(\boldsymbol{\xi}(t))$ is called relaxed bearing rigid, if it is BPE and subjected to a similarity transformation.*

Corollary 5.1. *If the formation is relaxed bearing rigid, then the result of Theorem 5.1 applies.*

Proof. The proof is analogous to the proof of Theorem 5.1. It is omitted here for the sake of brevity. □

5.3.2 Properties of BPE formations

To explore the properties of BPE formations, we describe relationship between a BPE formation and the specific PE bearings and then we derive a methodology to construct a BPE formation.

Lemma 5.1. *Consider a formation $\mathcal{G}(\boldsymbol{\xi}(t))$ defined in $\mathbb{R}^d$. Assume $\mathcal{G}$ is acyclic and has a spanning tree, then the formation is BPE if and only if all bearings are PE, i.e., $\bar{g}_k(t)$ satisfies the PE condition for all $k \in \{1, \dots, \mathring{m}\}$.*

Proof. Since $\mathcal{G} := (\mathcal{V}, \mathcal{E})$ is acyclic and has a spanning tree, $\mathring{m} = n - 1$, where $\mathring{m} = |\mathcal{E}|$ and $n = |\mathcal{V}|$. According to Definition 5.2, the proof of the lemma is equivalent to showing that $L_B(\boldsymbol{\xi}(t))$ is PE if and only if the corresponding bearing vectors $\bar{g}_k(t),\ \forall k = \{1, \dots, n-1\}$ satisfy the PE condition.

If $\bar{g}_k(t)$ satisfies the PE condition $\forall k = \{1, \dots, \mathring{m}\}$, this implies that the matrix $\Pi(t)$ is PE and hence it is obvious to conclude that $L_B(\boldsymbol{\xi}(t))$ is PE. Conversely, if $L_B(\boldsymbol{\xi}(t))$ is PE then there exist $T > 0$ and $0 < \mu < 1$ such that, $\forall t$, $\frac{1}{T}\int_t^{t+T} L_B(\boldsymbol{\xi}(\tau))d\tau \geq \mu L$. Now, since the $\bar{H}$ is a constant matrix with $\operatorname{rank}(\bar{H}) = d(n-1)$ and $\Pi(t) \in \mathbb{R}^{d(n-1)\times d(n-1)}$ it follows that $\Pi(t) \in \mathbb{R}^{d(n-1)\times d(n-1)}$ should satisfy the PE condition in equation (4.1). This in turn implies that each $\bar{g}_k(t)$ satisfies the PE condition in Definition 4.2, $\forall k \in \{1, \dots, n-1\}$. □

Lemma 5.2. *For a formation $\mathcal{G}(\boldsymbol{\xi}(t))$ defined in $\mathbb{R}^d$, assume* $\operatorname{rank}(L_B(\boldsymbol{\xi}(t))) = dn - d - 1$, $\forall t$. *Then $\mathcal{G}(\boldsymbol{\xi}(t))$ is BPE if and only if at least one bearing $\bar{g}_k$, $k \in \{1, \dots, \mathring{m}\}$ is PE.*

Proof. Since $\operatorname{rank}(L_B(\boldsymbol{\xi}(t))) = dn - d - 1$, $\forall t$, $\mathcal{G}$ has a spanning tree and $\operatorname{Null}(\Pi(t)) = \operatorname{span}\{\bar{H}, \boldsymbol{\xi}(t)\}$ (from Lemma B.1 in the Appendix). In order to prove that the formation is BPE, it remains to prove that its bearing Laplacian matrix is PE. Let $S = \{\mathring{\boldsymbol{\xi}} \in S | \mathring{\boldsymbol{\xi}} = [\mathring{\xi}_1^\top, \dots, \mathring{\xi}_n^\top] \in \mathbb{R}^{dn}\}$ be the set of all possible fixed configurations under the formation $\mathcal{G}(\mathring{\boldsymbol{\xi}})$ leading to $\operatorname{rank}(L_B(\mathring{\boldsymbol{\xi}})) = dn - d - 1$.

This in turn implies that for any $\boldsymbol{w} = [w_1^\top, \ldots, w_k^\top, \ldots, w_{\mathring{m}}^\top]^\top = \bar{H}\mathring{\boldsymbol{\xi}}$, there exists a positive constant ϵ such that $\|w_k\| = \|\mathring{\xi}_i - \mathring{\xi}_j\| \geq \epsilon$, $\forall k \in \{1, \ldots, \mathring{m}\}$. That is, the bearing information $\mathring{g}_k = \frac{w_k}{\|w_k\|}$ is well defined $\forall k \in \{1, \ldots, \mathring{m}\}$.

Now to prove the 'if' part of the lemma we use the fact that there exists at least one bearing vector $\bar{g}_q$, $q \in \{1, \ldots, \mathring{m}\}$ which is PE. This implies that there exist two constant $T > 0$, $0 < \mu_q < 1$ such that $\forall t$ and for all fixed $\mathring{\boldsymbol{\xi}} \in S$ leading to $\boldsymbol{w} = \bar{H}\mathring{\boldsymbol{\xi}}$, we have

$$\begin{aligned}\frac{1}{T}\boldsymbol{w}^\top \int_t^{t+T} \Pi(\tau) d\tau \boldsymbol{w} =& \frac{1}{T}\sum_{k=1}^{\mathring{m}} w_k^\top \int_t^{t+T} \pi_{\bar{g}_k(\tau)} d\tau w_k \\ \geq& \mu_q \|w_q\|^2.\end{aligned}$$

Choose $0 < \mu < \mu_q \frac{\|w_q\|^2}{\|\boldsymbol{w}\|^2}$, we can get

$$\frac{1}{T}\mathring{\boldsymbol{\xi}}^\top \bar{H}^\top \int_t^{t+T} \Pi(\tau) d\tau \bar{H}\mathring{\boldsymbol{\xi}} \geq \mu \mathring{\boldsymbol{\xi}}^\top \bar{H}^\top \bar{H}\mathring{\boldsymbol{\xi}}$$

which implies that $L_B(\boldsymbol{\xi}(t))$ is PE.

To prove the 'only if' part, we proceed hereafter by contradiction. Assume that none of the bearing vector is PE which implies that for all $0 < \mu_k < 1$, $\forall T > 0$, $\exists t$ and $\exists \boldsymbol{w} = \bar{H}\mathring{\boldsymbol{\xi}}$, such that $\frac{1}{T} w_k^\top \int_t^{t+T} \pi_{\bar{g}_k(\tau)} d\tau w_k < \mu_k \|w_k\|^2$, $\forall k \in \{1, \ldots, \mathring{m}\}$. Since $L_B(\boldsymbol{\xi}(t))$ is PE, there exists $T > 0$ and $0 < \mu < 1$ such that, $\forall t$ and $\forall \boldsymbol{w} = \bar{H}\mathring{\boldsymbol{\xi}}$, $\frac{1}{T}\boldsymbol{w}^\top \int_t^{t+T} \Pi(\tau) d\tau \boldsymbol{w} \geq \mu \|\boldsymbol{w}\|^2$. Choose $\mu_k \leq \frac{\mu \|\boldsymbol{w}\|^2}{m\|w_k\|^2}$, one concludes that, $\exists t$ and $\exists \boldsymbol{w} = \bar{H}\mathring{\boldsymbol{\xi}}$

$$\tfrac{1}{T}\boldsymbol{w}^\top \int_t^{t+T} \Pi(\tau) d\tau \boldsymbol{w} = \tfrac{1}{T}\textstyle\sum_{k=1}^{\mathring{m}} w_k^\top \int_t^{t+T} \pi_{\bar{g}_k(\tau)} d\tau w_k < \mu \|\boldsymbol{w}\|^2$$

which yields a contradiction. □

The following Lemma is a generalisation of Theorem 4.1 of reference [TZS+19] for the case of formations $\mathcal{G}(\boldsymbol{\xi}(t)) \in \mathbb{R}^d$ that are BPE. It explores the relationship between a BPE formation and the number of PE bearings inside the formation.

Lemma 5.3. *Consider a formation $\mathcal{G}(\boldsymbol{\xi}(t))$ defined in $\mathbb{R}^d$ along with bearing measurements $\{\bar{g}_k\}_{k \in \{1 \ldots \mathring{m}\}}$ associated to an arbitrary orientation of the graph. If the formation is BPE, then the number of PE bearing vectors, $\bar{m}$, satisfies the condition:*

1. *$\bar{m} \geq 1$, when $\mathring{m} \geq f(n,d)$,*

2. *$\bar{m} \geq (d-1)j - (d-1)f(n,d) + dn - d$, when $\mathring{m} = f(n,d) - j$ ($j \in \{1, \ldots, f(n,d) - n + 1\}$),*

with

$$f(n,d) = \begin{cases} n, \ n \leq d+1 \\ 1 + \llcorner \dfrac{n-2}{d-1} \lrcorner \times d + \operatorname{mod}(n-2, d-1) \\ + \operatorname{sgn}(\operatorname{mod}(n-2, d-1)), \ n \geq d+1, \end{cases}$$

which is the minimal number of edges that guarantees $\operatorname{rank}(L_B(\boldsymbol{\xi}(t))) = dn - d - 1$ *derived in [TVTA19].*

Proof. The proof of item 1) is similar to the proof of the 'only if' part in Lemma 5.2. It has been omitted here for the sake of brevity. Now, in order to show that item 2) is valid, we have to verify that if inequality (5.5) is satisfied, then $\bar{m} \geq (d-1)j - (d-1)f(n,d) + dn - d$ in the case of $\mathring{m} = f(n,d) - j$, $(j \in \{1, \ldots, f(n,d) - n + 1\})$. Inequality (5.5) implies that there exists $0 < \mu < 1$ and $T > 0$, $\forall t$ and $\forall \boldsymbol{x} \in R^{dn}$ such that $\bar{H}\boldsymbol{x} \neq 0$, we have $\frac{1}{T}\boldsymbol{x}^\top \int_t^{t+T} L_B(\boldsymbol{\xi}(\tau))d\tau \boldsymbol{x} \geq \mu \boldsymbol{x}^\top L \boldsymbol{x}$ or equivalently $\frac{1}{T}\boldsymbol{w}^\top \int_t^{t+T} \Pi(\tau)d\tau \boldsymbol{w} \geq \mu \|\boldsymbol{w}\|^2$, with $\boldsymbol{w} = \bar{H}\boldsymbol{x} \in \mathbb{R}^{d\mathring{m}}$.

We proceed by contradiction. Assume that $\bar{m} \leq (d-1)j - (d-1)f(n,d) + dn - d - 1$. Since we have $\mathring{m} - \bar{m}$ non-PE bearings and for each non-PE bearing $\bar{g}_k$ there is a $\lambda_{\min}(\frac{1}{T}\int_t^{t+T} \pi_{\bar{g}_k(\tau)} d\tau) < \mu$, it is straightforward to verify that $\lambda_{d\mathring{m}-(\mathring{m}-\bar{m})+1}(\frac{1}{T}\int_t^{t+T} \Pi(\tau)d\tau) = \lambda_{dn-d}(\frac{1}{T}\int_t^{t+T} \Pi(\tau)d\tau) < \mu$ ($\lambda_i(.)$ represents the ith eigenvalue of a symmetric matrix under a non-increasing order).

Now, using the fact that $\operatorname{rank}(\bar{H}) = dn - d$, we can ensure that if $\boldsymbol{x} = (x_1^\top, \ldots, x_n^\top)$ has dn independent entries (each $x_i \in \mathbb{R}^d$), then there exists a $\boldsymbol{w} = \bar{H}\boldsymbol{x}$ with $dn - d$ independent entries such that $\frac{1}{T}\boldsymbol{w}^\top \int_t^{t+T} \Pi(\tau)d\tau \boldsymbol{w} < \mu \|\boldsymbol{w}\|^2$, which yields a contradiction. □

Fig. 5.1 and 5.2 illustrate in the case of two- and three-dimensional space that when $\mathring{m} \leq f(n,d)$, in order to guarantee a BPE formation, the minimal number of PE bearing vectors decreases as the edges number $\mathring{m}$ increase.

In order to construct a new BPE formation from the existing BPE formation, we propose the following lemma that generalises the vertex addition method defined in the bearing-based Henneberg construction, [Ere07], provided that the resulting formation is BPE.

Lemma 5.4. *Given a BPE formation* $\mathcal{G}(\boldsymbol{\xi}(t)) \in \mathbb{R}^d$*, consider a new formation* $\mathcal{G}'(\boldsymbol{\xi}'(t)) \in \mathbb{R}^d$ *by adding a new agent* l *to* $\mathcal{G}(\boldsymbol{\xi}(t))$ *such that the new vertex set, edge set and bearing Laplacian are* $\mathcal{V}' = \mathcal{V} \cup \{l\}$*,* $\mathcal{E}'$ $(\mathcal{E} \subset \mathcal{E}'$ *and* $|\mathcal{E}'| = m')$ *and* $L_B'(\boldsymbol{\xi}'(t)) = \bar{H}'^\top \operatorname{diag}\left(\pi_{\bar{g}_k(t)}\right)\bar{H}', k \in \{1, \ldots, \mathring{m}, \ldots m'\}$*, respectively. Then* $\mathcal{G}'(\boldsymbol{\xi}'(t))$ *is also BPE if* $\sum_{k=\mathring{m}+1}^{m'} \pi_{\bar{g}_k}$ *is PE.*

Proof. Since $\mathcal{G}(\boldsymbol{\xi}(t))$ is BPE, there exist $0 < \mu < 1$ and $T > 0, \forall t \geq 0$, $\operatorname{tr}\left(\frac{1}{T}\int_t^{t+T} L_B(\boldsymbol{\xi}(\tau))d\tau\right) \geq (dn-d)\mu$ and $\operatorname{rank}(\int_t^{t+T} \operatorname{diag}\left(\pi_{\bar{g}_k(\tau)}\right)d\tau \bar{H}) = dn - d$. Due to the fact that the new formation is obtained by adding a vertex l to $\mathcal{V}$ and $(m' - \mathring{m})$ edge(s) (l, j) to $\mathcal{E}$ such that $\sum_{k=\mathring{m}+1}^{m'} \pi_{\bar{g}_k}$ is PE, it is straightforward to show that $\forall t \geq 0$,

$$\begin{aligned}
&\operatorname{tr}\left(\frac{1}{T}\int_t^{t+T} L_B^{'}(\boldsymbol{\xi}^{'}(\tau))d\tau\right) \\
&\geq \operatorname{tr}\left(\frac{1}{T}\int_t^{t+T} L_B(\boldsymbol{\xi}(\tau))d\tau\right) + \operatorname{tr}\left(\frac{1}{T}\int_t^{t+T} \sum_{k=\mathring{m}+1}^{m'} \pi_{\bar{g}_k(\tau)}d\tau\right) \geq dn\mu
\end{aligned}$$

and

$$\operatorname{rank}(\textstyle\int_t^{t+T} \operatorname{diag}(\pi)_{\bar{g}_k(\tau)}\, d\tau \bar{H}^{'}) = \operatorname{rank}(\textstyle\int_t^{t+T} L_B^{'}(\boldsymbol{\xi}^{'}(\tau))d\tau) = dn,$$

which indicates that $\mathcal{G}^{'}(\boldsymbol{\xi}^{'}(t))$ is also BPE. □

5.4 Bearing-only formation control for single-integrator dynamics

In this section we propose a bearing-only formation control law for a multi-agent system with single-integrator dynamics provided the desired formation is BPE.

Consider the formation $\mathcal{G}(\boldsymbol{\xi})$ defined in Section 5.2.2, where each agent $i \in \mathcal{V}$ is modeled as a single integrator with the following dynamics:

$$\dot{\xi}_i = v_i \tag{5.8}$$

where $\xi_i \in \mathbb{R}^d$ is the position of the ith agent and $v_i \in \mathbb{R}^d$ is its velocity input, as previously defined, both expressed in a common fixed frame. Similarly, let $\xi_i^*(t)$ and $v_i^*(t) \in \mathbb{R}^d$ denote the desired position and velocity of the ith agent, respectively, and define the desired relative position vectors ξ_{ij}^* and bearings g_{ij}^*, according to (5.1) and (5.2), respectively. Let $\boldsymbol{\xi}^*(t) = [\xi_1^{*\top}(t), \dots, \xi_n^{*\top}(t)]^\top \in \mathbb{R}^{dn}$ be the desired configuration. Let $\{\bar{\xi}_k^*(t)\}_{k\in\{1,\dots,\mathring{m}\}}$ and $\{\bar{g}_k^*(t)\}_{k\in\{1,\dots,\mathring{m}\}}$ be the set of all desired edge vectors and desired bearing vectors, respectively, under an arbitrary orientation of the graph.

We assume that the n-agent system satisfies the following assumptions.

Assumption 5.1. *The sensing topology of the group is described by a undirected graph $\mathcal{G}(\mathcal{V}, \mathcal{E})$ which has a spanning tree. Each agent $i \in \mathcal{V}$ can measure the relative bearing vectors g_{ij} to its neighbors $j \in \mathcal{N}_i$.*

Assumption 5.2. *The desired velocities $v_i^*(t)$ and desired positions $\xi_i^*(t)$ $(i \in \mathcal{V})$ are chosen such that, for all $t \geq 0$, $v_i^*(t)$ are bounded, the resulting desired bearings $g_{ij}^*(t)$ are well-defined and the desired formation $\mathcal{G}(\boldsymbol{\xi}^*(t))$ is BPE.*

With all these ingredients, we can define the bearing-only formation control problem as follows.

Problem 3. *Consider the system dynamics* (5.8) *and the underlying formation $\mathcal{G}(\boldsymbol{\xi})$. Under Assumptions 5.1-5.2, design distributed control laws based on bearing measurements that guarantee exponential stabilization of the actual formation to the desired one up to a translational vector.*

5.4.1 A bearing-only control law

For each agent $i \in \mathcal{V}$, define the position error $\tilde{\xi}_i := \xi_i - \xi_i^*$ along with the following kinematics:

$$\dot{\tilde{\xi}}_i = v_i - v_i^*, \tag{5.9}$$

and consider the following control law

$$v_i = -k_p \sum_{j \in \mathcal{N}_i} \pi_{g_{ij}} \xi_{ij}^* + v_i^*, \tag{5.10}$$

where k_p is a positive gain. Let $\tilde{\boldsymbol{\xi}} := \boldsymbol{\xi} - \boldsymbol{\xi}^*$ be the configuration error. Using the control law (5.10) for $i \in \mathcal{V}$, one gets:

$$\dot{\tilde{\boldsymbol{\xi}}} = -k_p L_B(\boldsymbol{\xi}(t))\tilde{\boldsymbol{\xi}}. \tag{5.11}$$

5.4.2 Exponential stabilization of the formations

Theorem 5.2. *Consider the error dynamics* (5.9) *along with the control law* (5.10)*. If Assumptions 5.1-5.2 are satisfied, then, under any initial condition satisfying* $\|\tilde{\boldsymbol{\xi}}(0)\| < \frac{1}{2}\min_{(i,j)\in\mathcal{E}} \|\xi_i^*(t) - \xi_j^*(t)\|$*, the feedback control* (5.10) *is well defined for all* $t \geq 0$ *and the following assertions hold*

1. *the relative centroid vector* $q_0 := \frac{1}{n}U^\top \tilde{\boldsymbol{\xi}}(t) \in \mathbb{R}^d$ *is invariant, that is* $q_0(t) = \frac{1}{n}U^\top\tilde{\boldsymbol{\xi}}(0)$*;*

2. *the equilibrium* $\tilde{\boldsymbol{\xi}}(t) - Uq_0 = 0$ *is exponentially stable (ES) .*

Proof. We begin by assuming that the controller (5.10) is well defined and then (in proof of Item 2) we show that it is well defined for all the time.
Proof of Item 1): Since $\operatorname{span}\{U\} \subset \operatorname{Null}(L_B(\boldsymbol{\xi}(t)))$, it is straightforward to verify that:

$$\frac{d}{dt}q_0 = U^\top\dot{\tilde{\boldsymbol{\xi}}}/n = -\frac{k_p}{n}U^\top L_B(\boldsymbol{\xi}(t))\tilde{\boldsymbol{\xi}} \equiv 0,$$

and hence one concludes that the relative centroid q_0 is constant ($q_0 = \frac{1}{n}U^\top\tilde{\boldsymbol{\xi}}(0) = \frac{1}{n}\sum_{i\in\mathcal{V}}\tilde{\xi}_i(0)$).

Proof of Item 2): Define a new variable $\delta := \tilde{\boldsymbol{\xi}} - Uq_0$ and note that $\tilde{\boldsymbol{\xi}}$ can be decomposed into the following two orthogonal components

$$\tilde{\boldsymbol{\xi}} = (I - \frac{1}{n}UU^T)\tilde{\boldsymbol{\xi}} + \frac{1}{n}UU^T\tilde{\boldsymbol{\xi}} = \delta + Uq_0.$$

Since $U^T L_B = 0$ and $L_B U = 0$, $\dot{\delta}(t) = -L_B(\boldsymbol{\xi}(t))\delta$. Considering the storage function

$$\mathcal{L}_1 = \frac{1}{2}\|\delta\|^2,$$

one can conclude that the time derivative of $\mathcal{L}_1$

$$\dot{\mathcal{L}}_1 = -k_p \boldsymbol{\delta}^\top L_B(\boldsymbol{\xi}(t))\boldsymbol{\delta} \leq 0 \tag{5.12}$$

is negative semi-definite and $\boldsymbol{\delta}(t)$ is bounded and non-increasing for all $t \geq 0$, due to the fact that $L_B(\boldsymbol{\xi}(t)) \geq 0$. Since $\boldsymbol{\delta}(t)$ and Uq_0 are orthogonal, it follows that $\|\tilde{\boldsymbol{\xi}}(t)\|^2 = \|\boldsymbol{\delta}(t)\|^2 + \|U(\frac{1}{n}U^\top \tilde{\boldsymbol{\xi}}(0))\|^2 \leq \|\tilde{\boldsymbol{\xi}}(0)\|^2$ for all $t \geq 0$.

In order to show that $g_{ij}(t), \forall (i,j) \in \mathcal{E}$ are well defined $\forall t \geq 0$ (and hence the feedback control (5.10) is well defined) under the proposed initial condition we use the triangle inequality to show that $\forall t \geq 0, (i,j) \in \mathcal{E}$

$$\begin{aligned}
\|\xi_i(t) - \xi_j(t)\| &\geq \|\xi_i^*(t) - \xi_j^*(t)\| - \|\xi_i(t) - \xi_i^*(t)\| - \|\xi_j(t) - \xi_j^*(t)\| \\
&\geq \|\xi_i^*(t) - \xi_j^*(t)\| - 2\|\tilde{\boldsymbol{\xi}}(t)\| \\
&\geq \|\xi_i^*(t) - \xi_j^*(t)\| - 2\|\tilde{\boldsymbol{\xi}}(0)\|
\end{aligned}$$

which remains positive as long as

$$\|\tilde{\boldsymbol{\xi}}(0)\| < \frac{1}{2} \min_{(i,j)\in\mathcal{E}} \|\xi_i^*(t) - \xi_j^*(t)\|.$$

As for the proof of the ES of the equilibrium point $\boldsymbol{\delta} = 0$ we recall that (5.12) can be rewritten as

$$\begin{aligned}
\dot{\mathcal{L}}_1 = -k_p \tilde{\boldsymbol{\xi}}^\top L_B(\boldsymbol{\xi}(t))\tilde{\boldsymbol{\xi}} &= -k_p \sum_{k=1}^{\mathring{m}} \bar{\xi}_k^{*\top} \pi_{\bar{g}_k} \bar{\xi}_k^* \\
&= -k_p \sum_{k=1}^{\mathring{m}} \frac{\|\bar{\xi}_k^*\|^2}{\|\bar{\xi}_k\|^2} (\bar{\xi}_k - \bar{\xi}_k^*)^\top \pi_{\bar{g}_k^*} (\bar{\xi}_k - \bar{\xi}_k^*)
\end{aligned}$$

and note that $\|\bar{\xi}_k(t)\| \leq \|\bar{\xi}_k^*(t)\| + 2\|\tilde{\boldsymbol{\xi}}(0)\|$ to obtain

$$\dot{\mathcal{L}}_1 \leq -\gamma \boldsymbol{\delta}^\top L_B(\boldsymbol{\xi}^*(t))\boldsymbol{\delta},$$

with $\gamma = k_p \left(1 - \frac{2\|\tilde{\boldsymbol{\xi}}(0)\|}{2\|\tilde{\boldsymbol{\xi}}(0)\| + \min_{k=1,\ldots,\mathring{m}} \|\bar{\xi}_k^*(t)\|}\right)^2 > 0$. Using the fact that $U^\top \boldsymbol{\delta}(t) \equiv 0$ and since the desired formation is BPE, one can ensure that

$$\begin{aligned}
\frac{1}{T}\boldsymbol{\delta}(t)^\top \int_t^{t+T} L_B(\boldsymbol{\xi}^*(\tau)) d\tau \boldsymbol{\delta}(t) &\geq \mu \boldsymbol{\delta}(t)^\top \bar{H}^\top \bar{H} \boldsymbol{\delta}(t) \\
&\geq \mu \lambda_{dn-d} \|\boldsymbol{\delta}(t)\|^2,
\end{aligned}$$

recall that λ_{dn-d} is the smallest positive eigenvalue of $\bar{H}^\top \bar{H}$. Hence, condition (1) of Theorem B.1 in the appendix is satisfied. Since $L_B(\boldsymbol{\xi}(t))$ is bounded and condition (2) of Theorem B.1 is also satisfied, one concludes that $\boldsymbol{\delta} = 0$ is exponentially stable.

Remark 5.3. Note that although the closed-loop dynamics (5.11) is similar to the observer error dynamics (5.7), only local exponential stability can be ensured here while global exponential stability of the origin of the observer error is guaranteed. For both cases the bearing Laplacian is the same but the persistence of excitation conditions are not. For the observer design it is assumed that the actual formation is BPE while for controller design the BPE is assumed for the desired formation. The latter condition does not guarantee that the actual bearings, the bearing Laplacian, and hence the control law are well-defined for all time, since collisions may occur during the time evolution of the formation. This in turn implies that the actual state of the formation will always admit an exception set of critical points that cannot be part of the basin of attraction of the desired equilibrium. Theorem 5.2 provides a conservative estimate for the basin of attraction, corroborating the idea that if the initial conditions are sufficiently close to a desired formation that is well-defined for all time then no collisions will occur and exponential convergence is guaranteed.

□

5.5 Bearing formation control for double-integrator dynamics in $\mathbb{R}^d$

In this section we will extend the bearing formation control law for a multi-agent system with double-integrator dynamics in $\mathbb{R}^d$. Consider the formation $\mathcal{G}(\xi)$ defined in Section 5.2.2, where each agent $i \in \mathcal{V}$ is modeled as a double integrator with the following dynamics:

$$\begin{cases} \dot{\xi}_i = v_i \\ \dot{v}_i = u_i, \end{cases} \tag{5.13}$$

and acceleration input $u_i \in \mathbb{R}^d$, all expressed in a common inertial frame. Let $u_i^*(t) \in \mathbb{R}^d$ denote the desired acceleration of the ith agent and $\boldsymbol{v}^*(t) = [v_1^{*\top}(t), ..., v_n^{*\top}(t)]^\top \in \mathbb{R}^{dn}$ stacked velocity vector of the desired configuration $\boldsymbol{\xi}^*(t)$.

We assume that the n-agent system satisfies the following assumptions.

Assumption 5.3. *The sensing topology of the group is described by an undirected graph $\mathcal{G}(\mathcal{V}, \mathcal{E})$ which has a spanning tree. Each agent $i \in \mathcal{V}$ can measure its velocity v_i and the relative bearing vectors g_{ij} to its neighbors $j \in \mathcal{N}_i$.*

Assumption 5.4. *The desired acceleration $u_i^*(t)$, desired velocity $v_i^*(t)$, and desired position $\xi_i^*(t)$ ($i \in \mathcal{V}$) are chosen such that $u_i^*(t)$ and $v_i^*(t)$ are bounded, the resulting desired bearings $g_{ij}^*(t)$ are well-defined and the desired formation $G(\boldsymbol{\xi}^*(t))$ is BPE, for all $t \geq 0$.*

With all these ingredients, we can define the bearing formation control problem as follows.

Problem 4. *Consider the system (5.13) and the underlying formation $\mathcal{G}(\xi)$. Under Assumptions 5.3 - 5.4, design distributed control laws based on bearing and velocity measurements that guarantee exponential stabilization of the actual formation to the desired one up to a translational vector.*

5.5.1 A bearing control law

For each agents $i \in \mathcal{V}$, define the velocity error $\tilde{v}_i := v_i - v_i^*$. Then the error dynamics of error states $(\tilde{\xi}_i, \tilde{v}_i)$ can be represented as:

$$\begin{cases} \dot{\tilde{\xi}}_i = \tilde{v}_i \\ \dot{\tilde{v}}_i = u_i - u_i^*. \end{cases} \tag{5.14}$$

The following control law is proposed for each agent $i \in \mathcal{V}$

$$u_i = -k_p \sum_{j \in \mathcal{N}_i} \pi_{g_{ij}} \xi_{ij}^* - k_d \tilde{v}_i + u_i^* \tag{5.15}$$

where k_p and k_d are positive constant gains. Defining the new variable $\tilde{\boldsymbol{v}} := \boldsymbol{v} - \boldsymbol{v}^*$ and under the control law (5.15), the dynamics of $(\tilde{\boldsymbol{\xi}}, \tilde{\boldsymbol{v}})$ can be presented as

$$\begin{cases} \dot{\tilde{\boldsymbol{\xi}}} = \tilde{\boldsymbol{v}} \\ \dot{\tilde{\boldsymbol{v}}} = -k_p L_B(\boldsymbol{\xi}(t)) \tilde{\boldsymbol{\xi}} - k_d \tilde{\boldsymbol{v}} \end{cases} \tag{5.16}$$

5.5.2 Exponential stabilization of the formations

Theorem 5.3. *Consider the error dynamics* (5.14) *along with the control law* (5.15)*. If the Assumptions 5.3-5.4 are satisfied and the positive gains* k_d *and* k_p *are chosen such that* $k_d > \frac{k_p}{4}\|\bar{H}\|^2 + 1$*, then for any initial condition such that*

$$\|[\tilde{\boldsymbol{\xi}}(0)^\top \tilde{\boldsymbol{v}}(0)^\top]\| < \frac{1}{2b} \min_{(i,j)\in\mathcal{E}} \|\xi_i^*(t) - \xi_j^*(t)\|, \tag{5.17}$$

with $b = \max\{\sqrt{\frac{\lambda_{\max}(P)}{\lambda_{\min}(P)}}, \sqrt{2}\}$ *and* $P = \frac{1}{2}\begin{bmatrix} k_d I_{dn} & I_{dn} \\ I_{dn} & I_{dn} \end{bmatrix} > 0$*, the feedback control* (5.15) *is well defined and the following two assertions hold* $\forall t \geq 0$*:*

1. *the relative centroid and its velocity* $(q_0(t), \dot{q}_0(t)) = (\frac{U^\top \tilde{\boldsymbol{\xi}}(t)}{n}, \frac{U^\top \tilde{\boldsymbol{v}}(t)}{n}) \in \mathbb{R}^{2d}$ *converges exponentially to* $(\mathring{q}_0 = q_0(0) + \frac{1}{k_d}\dot{q}_0(0), 0)$*,*

2. *the equilibrium* $(\tilde{\boldsymbol{\xi}} - U\mathring{q}_0, \tilde{\boldsymbol{v}}) = (0, 0)$ *is ES.*

Proof. Analogously to the proof of Theorem 5.2, we assume first that the controller (5.15) is well defined and then we show that is it so in the proof of Item 2.

Proof of Item 1): From (5.16) and due to the fact that $\text{span}\{U\} \subset \text{Null}(L_B(\boldsymbol{\xi}(t)))$, one has:

$$\ddot{q}_0(t) = -k_d \dot{q}_0(t)$$

which implies that $\dot{q}_0(t) = \dot{q}_0(0)\exp(-k_d t)$ and $q_0(t) = \frac{1}{k_d}(1 - \exp(-k_d t))\dot{q}_0(0) + q_0(0)$ and hence $(q_0(t), \dot{q}_0(t))$ converges exponentially to $(\mathring{q}_0, 0)$.

Proof of Item 2): Similarly to the proof of Theorem B.1, we define $\tilde{\boldsymbol{x}} := [(\tilde{\boldsymbol{\xi}} - Uq_0)^\top, (\tilde{\boldsymbol{v}} - U\dot{q}_0)^\top]^\top$ and note that $[(Uq_0)^\top \ (U\dot{q}_0)^\top]\tilde{\boldsymbol{x}} = 0$, meaning that $[\tilde{\boldsymbol{\xi}}(t)^\top, \tilde{\boldsymbol{v}}(t)^\top] = \tilde{\boldsymbol{x}}(t)^\top + [(Uq_0(t))^\top \ (U\dot{q}_0(t))^\top]$ and the two components are orthogonal. We will first show $\tilde{\boldsymbol{x}}$ is bounded. Using (5.16), it is straightforward to verify that:

$$\dot{\tilde{\boldsymbol{x}}}(t) = -A(t)\tilde{\boldsymbol{x}}(t) \tag{5.18}$$

with $A = \begin{bmatrix} 0_{dn} & -I_{dn} \\ k_p L_B & k_d I_{dn} \end{bmatrix}$. Considering the following positive definite storage function

$$\mathcal{L}_2 = \tilde{\boldsymbol{x}}^\top P \tilde{\boldsymbol{x}},$$

one can verify that

$$\dot{\mathcal{L}}_2 = -\tilde{\boldsymbol{x}}^\top Q(t)\tilde{\boldsymbol{x}}, \tag{5.19}$$

with $Q(t) = \begin{bmatrix} k_p L_B(\boldsymbol{\xi}(t)) & \frac{k_p}{2} L_B(\boldsymbol{\xi}(t)) \\ \frac{k_p}{2} L_B(\boldsymbol{\xi}(t)) & (k_d - 1)I_{dn} \end{bmatrix}$. The matrix Q can be decomposed as $Q = S^\top M_Q S$ with $S = \begin{bmatrix} \Pi \bar{H} & 0_{d\mathring{m} \times dn} \\ 0_{dn} & I_{dn} \end{bmatrix}$ and $M_Q = \begin{bmatrix} k_p I_{d\mathring{m}} & \frac{k_p}{2}\bar{H} \\ \frac{k_p}{2}\bar{H}^\top & (k_d - 1)I_{dn} \end{bmatrix}$, which shows that if $k_d > \frac{k_p}{4}\|\bar{H}\|^2$ then $Q \geq 0$ and $\dot{\mathcal{L}}_2$ is negative definite. Therefore, one concludes that $\tilde{\boldsymbol{x}}(t)$ is bounded which in turn implies that $\tilde{\boldsymbol{\xi}}$ is bounded. Since $\tilde{\boldsymbol{x}}$ and $[(Uq_0)^\top \ (U\dot{q}_0)^\top]^\top$ are orthogonal, $q_0(t) = \frac{1}{k_d}(1 - \exp(-k_d t))\dot{q}_0(0) + q_0(0)$ and $k_d > 1$, $\tilde{\boldsymbol{\xi}}(t)$ can be bounded by

$$\begin{aligned}
\|\tilde{\boldsymbol{\xi}}(t)\|^2 &= \|\tilde{\boldsymbol{\xi}}(t) - Uq_0(t)\|^2 + \|Uq_0(t)\|^2 \\
&\leq \|\tilde{\boldsymbol{x}}(t)\| + 2(\frac{1}{k_d^2}\|Uq_0(0)\|^2 + \|U\dot{q}_0(0)\|^2) \\
&\leq \frac{\lambda_{\max}(P)}{\lambda_{\min}(P)}\|\tilde{\boldsymbol{x}}(0)\|^2 + 2(\|Uq_0(0)\|^2 + \|U\dot{q}_0(0)\|^2) \\
&\leq b^2\|[\tilde{\boldsymbol{\xi}}(0)^\top \tilde{\boldsymbol{v}}(0)^\top]\|^2
\end{aligned}$$

recalling that $b = \max\{\sqrt{\frac{\lambda_{\max}(P)}{\lambda_{\min}(P)}}, \sqrt{2}\}$.

Analogously to the proof of Theorem 5.2, item 2, we use the triangle inequality to show that $\forall t \geq 0, (i,j) \in \mathcal{E}$

$$\begin{aligned}
\|\xi_i(t) - \xi_j(t)\| &\geq \|\xi_i^*(t) - \xi_j^*(t)\| - 2\|\tilde{\boldsymbol{\xi}}(t)\| \\
&\geq \|\xi_i^*(t) - \xi_j^*(t)\| - 2b\|[\tilde{\boldsymbol{\xi}}(0)^\top \tilde{\boldsymbol{v}}(0)^\top]\|
\end{aligned}$$

which remains positive as long as $\|[\tilde{\boldsymbol{\xi}}(0)^\top \tilde{\boldsymbol{v}}(0)^\top]\| < \frac{1}{2b}\min_{(i,j)\in\mathcal{E}} \|\xi_i^*(t) - \xi_j^*(t)\|$. Thus $g_{ij}(t), \forall (i,j) \in \mathcal{E}$ are well defined $\forall t \geq 0$ (and hence the feedback control (5.15) is well defined) as long as the initial conditions satisfy (5.17). Similarly, one can define an upper bound for $\|\xi_i(t) - \xi_j(t)\|$ and conclude that $\|\bar{\xi}_k(t)\|$ is lower and upper bounded according to $0 < \|\bar{\xi}_k^*(t)\| - 2b\|[\tilde{\boldsymbol{\xi}}(0)^\top \tilde{\boldsymbol{v}}(0)^\top]\| \leq \|\bar{\xi}_k(t)\| \leq \|\bar{\xi}_k^*(t)\| + 2b\|[\tilde{\boldsymbol{\xi}}(0)^\top \tilde{\boldsymbol{v}}(0)^\top]\|$.

Now, to prove that $(\tilde{\boldsymbol{\xi}} - U\mathring{q}_0, \tilde{\boldsymbol{v}}(t)) = (0,0)$ is also ES, it suffices to prove that $\tilde{\boldsymbol{x}} = 0$ is ES. Since $Q = S^T M_Q S$, $k_d > \frac{k_p}{4}\|\bar{H}\|^2 + 1$, and $\bar{\xi}_k^{*\top} \pi_{\bar{g}_k} \bar{\xi}_k^* = \frac{\|\bar{\xi}_k^*\|^2}{\|\bar{\xi}_k\|^2} \bar{\xi}_k^\top \pi_{\bar{g}_k^*} \bar{\xi}_k$, one has

$$\dot{\mathcal{L}}_2 = -\tilde{\boldsymbol{x}}^\top S^\top M_Q S \tilde{\boldsymbol{x}} \leq -\lambda_M \tilde{\boldsymbol{x}}^\top S^\top S \tilde{\boldsymbol{x}} \leq -\gamma \tilde{\boldsymbol{x}}^\top \Sigma \tilde{\boldsymbol{x}} \leq 0$$

with $\lambda_M = \frac{k_p(k_d-1)-\frac{k_p^2}{4}\|\bar{H}\|^2}{k_d-1+k_p} > 0$, $\Sigma(t) = \begin{bmatrix} L_B(\boldsymbol{\xi}^*(t)) & 0_{dn} \\ 0_{dn} & I_{dn} \end{bmatrix}$ and $\gamma = \lambda_M \min\limits_{k=\{1,..,\mathring{m}\}} (\frac{\|\bar{\xi}_k^*(t)\|}{\|\bar{\xi}_k(t)\|})^2 > 0$. Since $\mathcal{L}_2$ is nonincreasing and $\|\bar{\xi}_k(t)\|$ is upper bounded, one guarantees that:

$$\gamma \geq \lambda_M \left(1 - \frac{2b\|[\tilde{\boldsymbol{\xi}}(0)^T \;\; \tilde{\boldsymbol{v}}(0)^T]\|}{2b\|[\tilde{\boldsymbol{\xi}}(0)^T \;\; \tilde{\boldsymbol{v}}(0)^T]\| + \min\limits_{k=\{1,..,\mathring{m}\}} \|\bar{\xi}_k^*(t)\|} \right)^2 .$$

Using the BPE condition of the desired formation and the fact that span$\{U\}$ = Null(L_B), one concludes that condition (1) in Theorem B.1 is satisfied. By a direct application of Lemma B.2, condition (2) in Theorem B.1 is also satisfied, and therefore $\tilde{\boldsymbol{x}} = 0$ is exponentially stable. This in turn implies that $(\tilde{\boldsymbol{\xi}} - U\mathring{q}_0, \tilde{\boldsymbol{v}}) = (0, 0)$ is ES.

□

5.6 Simulation Results

In this section, simulation results are provided to validate the controllers for multi-agent system under both single- and double- integrator dynamics.

For the single integrator dynamics system, we consider a 8-agent system in 3-D space. The desired formation is chosen such that $\xi_i^*(t) = r(t)R(t)^\top \xi_i^*(0) + [0 \; t/5 \; 0]^\top$, with $r(t) = 0.5\sin(\frac{\pi}{6}t) + 1.5$, $R(t) = \begin{bmatrix} 1 & 0 & 0 \\ 0 & \cos(\frac{\pi}{3}t) & -\sin(\frac{\pi}{3}t) \\ 0 & \sin(\frac{\pi}{3}t) & \cos(\frac{\pi}{3}t) \end{bmatrix}$, $\xi_1^*(0) = [\sqrt{2} \; 0 \; -1]^\top, \xi_2^*(0) = [0 \; \sqrt{2} \; -1]^\top, \xi_3^*(0) = [-\sqrt{2} \; 0 \; -1]^\top, \xi_4^*(0) = [0 \; -\sqrt{2} \; -1]^\top, \xi_5^*(0) = [\sqrt{2} \; 0 \; 1]^\top, \xi_6^*(0) = [0 \; \sqrt{2} \; 1]^\top, \xi_7^*(0) = [-\sqrt{2} \; 0 \; 1]^\top$, and $\xi_8^*(0) = [0 \; -\sqrt{2} \; 1]^\top$, which form a cube in $\mathbb{R}^3$ with time-varying scale that rotates about the x-axis and translates along y-axis as show in Fig. 5.3. Note that the desired formation is not bearing rigid but relaxed bearing rigid. The initial conditions are chosen such that $q_0 = 0$ (the initial centroid coincides with the initial centroid of the desired formation) : $\xi_1(0) = [1 \; 0 \; 0]^\top, \xi_2(0) = [-1 \; 2.5 \; 1]^\top, \xi_3(0) = [-2 \; -1 \; -1]^\top, \xi_4(0) = [-0.5 \; 0.5 \; 1]^\top, \xi_5(0) = [1.5 \; 0 \; 1]^\top, \xi_6(0) = [-1 \; 0 \; 1]^\top, \xi_7(0) = [0 \; -1 \; -1]^\top$, and $\xi_8(0) = [2 \; 0 \; -2]^\top$. The chosen gain is $k_p = 1$. Fig. 5.3 shows the evolution of the formation in three dimensional space and Fig. 5.4 depicts the evolution of the error variable $\tilde{\boldsymbol{\xi}}(t)$. As we can see from the figures, the formation converges to the desired one after $t = 20s$ and starts to move along the desired trajectories. We can conclude that, under the proposed bearing-only control laws, the formation achieves the desired geometric pattern in terms of shape and scale without the need for bearing rigidity. What's more, since the desired scale can be time-varying, if one of the agents is assigned to be the leader, the formation is able to achieve the task of collision avoidance such as passing through a narrow passage as depicted in [ZZ15b], in which the position information is still needed in the controller design and at least two leaders are required.

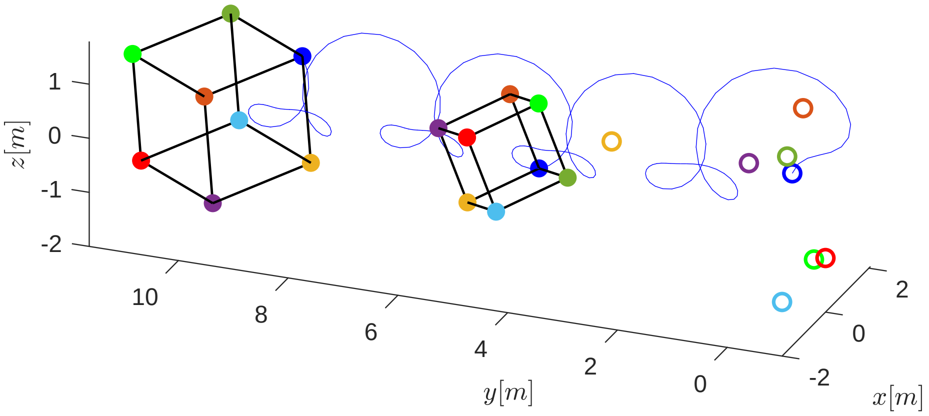

Figure 5.3: The figure shows three snapshots of the 3-D evolution of a cubic formation: the initial conditions (void circles) when $t = 0$; $t = 24.5$s, when agents have converged to the desired formation; $t = 50$s, when agents move along the desired trajectories. The blue line represents the trajectory of the dark blue agent and the black lines represent the connections between agents.

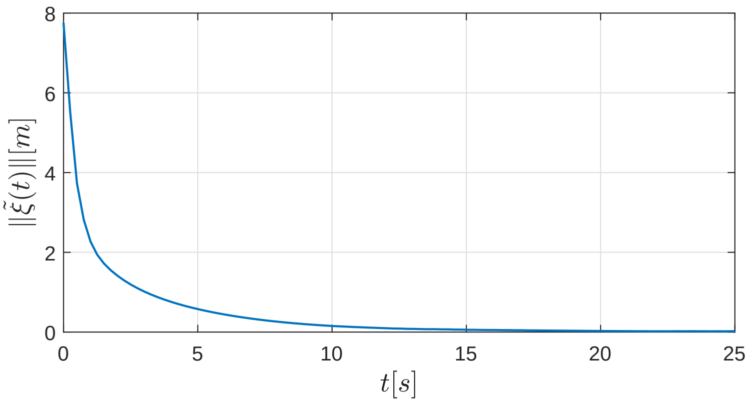

Figure 5.4: Time evolution of the norm of the error ($\|\tilde{\xi}\|$).

For the multi-agent system under double-integrator dynamics, we consider a four-agent system in both 2-D and 3-D space.

In the 2-D case, the desired formation is chosen to be relaxed bearing rigid such that $\xi_i^*(t) = R(t)^\top \xi_i^*(0)$, with $R(t) = \begin{bmatrix} \cos(\frac{\pi}{3}t) & -\sin(\frac{\pi}{3}t) \\ \sin(\frac{\pi}{3}t) & \cos(\frac{\pi}{3}t) \end{bmatrix}$, $\xi_1^*(0) = [0.5\ 0.5]^\top, \xi_2^*(0) = [0.5\ -0.5]^\top, \xi_3^*(0) = [-0.5\ -0.5]^\top$ and $\xi_4^*(0) = [-0.5\ 0.5]^\top$, which form a squared shape in $\mathbb{R}^2$ that rotates about its center. The graph topology is such that there is only one spanning tree. The initial conditions are chosen such that $\xi_1(0) = [-1\ 1.5]^\top$, $\xi_2(0) = [-1\ 2]^\top$, $\xi_3(0) = [-2\ -1]^\top, \xi_4(0) = [1\ -1]^\top, v_1(0) = [0\ 0]^\top$, $v_2(0) = [0\ 1]^\top$, $v_3(0) = [1\ 0]^\top$ and $v_4(0) = [0\ -1]^\top$. The chosen gains are $k_p = 8$ and $k_d = 11$. Fig. 5.5 depicts 2-D evolution of the formation and we can see that the four agents converge to the desired formation. Fig. 5.6 shows the time evolution and the convergence of $\|\tilde{\boldsymbol{\xi}}(t) - Uq_0(t)\|$ and $\|\tilde{\boldsymbol{v}}(t)\|$ to 0. We can conclude that the convergence of the formation to the desired one can be guarantee even if there is only one spanning tree in the graph topology.

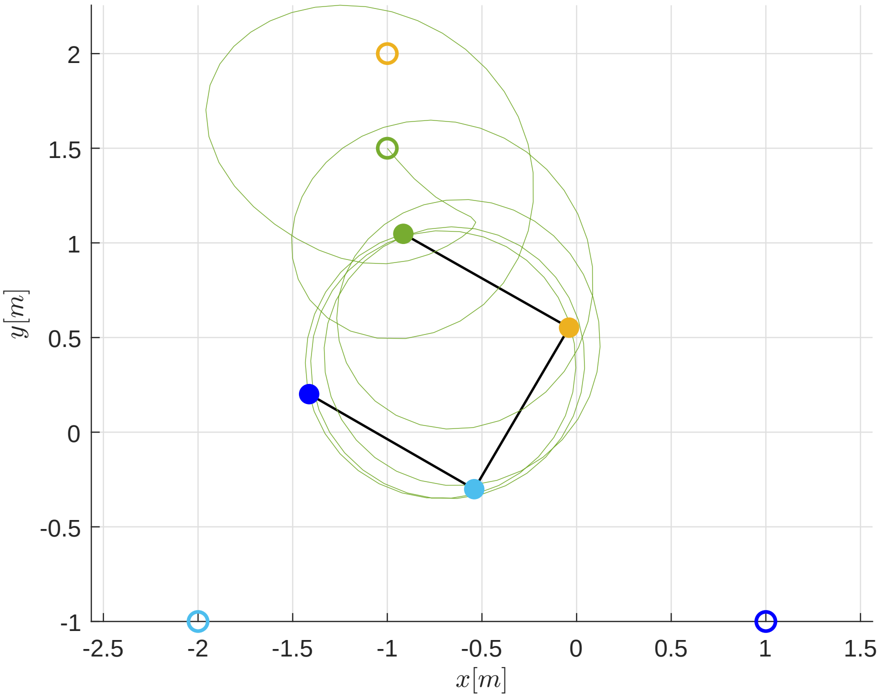

Figure 5.5: 2-D evolution of a square formation. The void and solid circles represents the initial and final positions of the agents, respectively. The green line is the trajectory of one of the agents and the black lines denote the connections between and the agents.

In the 3-D case, we consider a relaxed bearing rigid desired formation with the graph topology that has only one spanning tree, in which the four agents form a pyramid shape in $\mathbb{R}^3$ that rotates about one of the agents (Fig. 5.7). The desired positions of the agents are such that $\xi_i^*(t) = R(t)^\top \xi_i^*(0)$, with $R(t) = \begin{bmatrix} \cos(\frac{\pi}{4}t) & -\sin(\frac{\pi}{4}t) & 0 \\ \sin(\frac{\pi}{4}t) & \cos(\frac{\pi}{4}t) & 0 \\ 0 & 0 & 1 \end{bmatrix}$, $\xi_1^*(0) = [0\ 0\ 0]^\top, \xi_2^*(0) = [1\ 0\ 0]^\top, \xi_3^*(0) = [0.5\ -\sqrt{3}/2\ 0]^\top$ and $\xi_4^*(0) = [\sqrt{3}/2\ -0.5\ 1]^\top$. The initial conditions are chosen such that $\xi_1(0) = [-2\ -1\ -1]^\top$, $\xi_2(0) = [-1\ 2\ 1]^\top$, $\xi_3(0) = [-2\ -1\ -1]^\top$, $\xi_4(0) = [-0.5\ -0.5\ 1]^\top, v_1(0) = [0\ 0\ -1]^\top$, $v_2(0) = [0\ 1\ 0]^\top$, $v_3(0) = [1\ 0\ 0]^\top$ and $v_4(0) = [1\ 0\ -1]^\top$. The chosen gains are $k_p = 7$ and $k_d = 10$. Fig. 5.7 shows the time evolution of the 3-D formation converging to the desired one and Fig. 5.8 shows the time evolution of error states $\tilde{\boldsymbol{\xi}}(t) - Uq_0(t)$ and $\tilde{\boldsymbol{v}}(t)$, respectively. It validates the fact

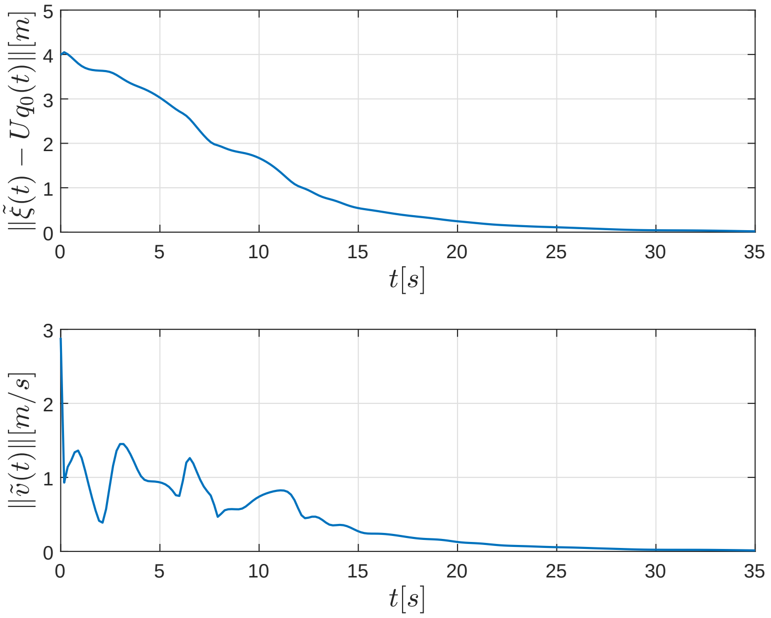

Figure 5.6: Time evolution of the norm of the error ($\|\tilde{\xi}(t) - Uq_0(t)\|$) and relative velocity error ($\|\tilde{v}\|$).

that the proposed control laws stabilize the formation without requiring bearing rigidity.

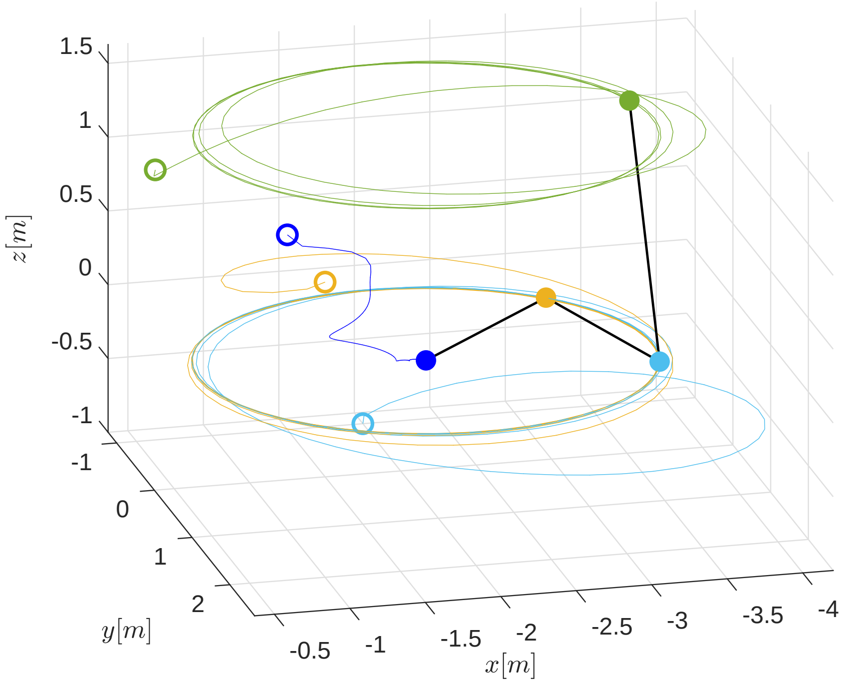

Figure 5.7: 3-D evolution of a pyramid formation. The void and solid circles represents the initial and final positions of the agents, respectively. The colorful line are the trajectories of the agents and the black lines denote the connections between and the agents.

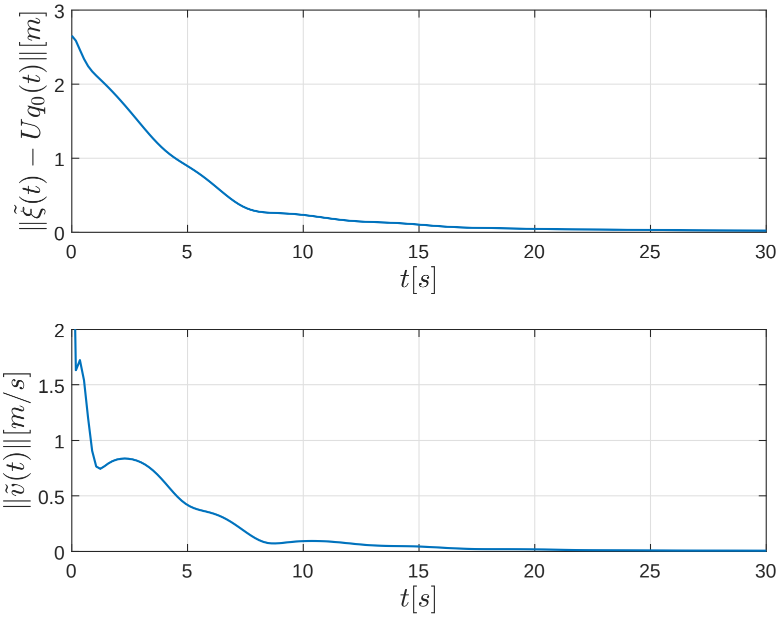

Figure 5.8: Time evolution of the norm of the error ($\|\tilde{\xi}(t) - Uq_0(t)\|$) and relative velocity error ($\|\tilde{v}\|$).

5.7 Conclusion

This chapter presents new results on formation control of both kinematic and dynamic systems based on time-varying bearing measurements. The key contribution is to show that if the desired formation is bearing persistently exciting, relaxed conditions on the interaction topology (which do not require bearing rigidity) can be used to derive distributed control laws that guarantee exponential stabilization of the desired formation only up to a translation vector. Simulations results are provided to illustrate the performance of the proposed control method.

6

CONCLUSIONS AND FUTURE DIRECTIONS

This dissertation addressed problems of vision-based control for Unmanned aerial vehicles. Both single and multiple vehicles configurations are considered, targeting applications in urban or congested environments.

For the single vehicle case, different types of vehicles (fixed-wing and VTOL UAVs) are taken into consideration. Spherical image centroid and optical flow are explored to develop novel IBVS control methods that, despite being simple, overcome the disadvantages of classical IBVS techniques and eliminate the need to measure or estimate image depth and state variables.

For fixed-wing UAV, a novel 2D image-based controller is proposed, which automatically steers the vehicle during the first three stages of landing: alignment, glide-slope, and flare. Geometric image features of the runway (used as a relative position cue), and optical flow obtained from its textured ground (used as a velocity cue), are exploited to derive a feedback controller for the automatic maneuver. Although the proposed solution exploits directly visual features in the controller, it differs from the classical IBVS schemes by supporting the derivation of the control law on the system dynamics instead of on the image features dynamics. The proposed controller ensures the horizontal position alignment and a smooth touchdown of the aircraft without estimating the height above the runway. In addition, the 2D image-based control structure adopted also enforces wind disturbance rejection, without the need for an explicit wind estimator. Simulation results are presented to illustrate the performance of the controller.

For VTOL UAV, we solve the problem of controlling the aircraft to go through a window and land on a planar target, using a novel Image-Based Visual Servo (IBVS) controller that relies on optical flow measurements and spherical centroid of both window and landing pad. Under the proposed control laws, the vehicle is able to go through the center of the window with non-zero velocity along the direction orthogonal to the window, keeping at all times a safety distance with respect to the window edges, and then, to execute a smooth touchdown onto the landing pad, keeping at all time a positive height above the target plane. To achieve the proposed objective, no direct measurements nor explicit estimate of position or velocity are required. Experimental results are presented where the controllers run on an on-board computer together with the image processing algorithm for the targets detection and the translational optical flow computation.

For multiple vehicles, vision-based formation control are considered. More specifically bearing formation control methods are proposed for formations under both directed and undirected graph topologies by exploring the persistently exciting bearing references. We propose a general concept, *relaxed bearing rigidity*, which guarantees the uniqueness of a fixed geometric pattern without imposing bearing rigid conditions on the graph topology. By defining a desired formation that is bearing PE, the proposed distributed control laws guarantee exponential stabilization of the desired formation in terms of shape and scale without the measurement or estimation of any distance between two agents. The key contribution is that the (local) exponential stabilization of the actual formation to the desired one is guaranteed as long as the desired formation satisfies PE conditions that are adequately defined for the specific bearings. The approach generalizes stability results provided in prior work which are based on bearing rigidity and constraint consistence of the graph topology to ensure the exponential stabilization of the actual formation to a desired geometric pattern up to a scale factor. Simulations results are provided to illustrate the performance of the proposed control method.

6.1 Future directions

In theoretical terms, bearing formation control under PE should be extended to deal with more general directed graphs. In addition, taking advantage once again of the properties of PE, the generalization of the proposed bearing controllers from fixed to time-varying graph topologies is also envisioned as promising improvement. Moreover, we believe that the bearing controllers can also be applied to the problem of multi-agent attitude synchronization. Another relevant venue of research is to explore optical flow in order to incorporate collision avoidance capabilities in the bearing control laws and thereby ensure collision avoidance between different agents in the initial formation transient and guarantee stability in a large domain. In a more challenging scenario, the collision avoidance capabilities provided by the optical flow could also be explored to drive the formation to avoid obstacles presented in the environment.

From the practical point of view, the next natural step is the implementation and experimental demonstration of the proposed bearing formation control laws on UAVs equipped with cameras and IMUs. To this end, several practical issues need to be considered including the limited field of view of the cameras, non-persistent image feature occlusions, the computational burden and delays of image processing algorithms, and vehicle instrumentation and payload restrictions, to name a few.

A

IMAGE FEATURES AND TRANSLATIONAL OPTICAL FLOW

In this section, we introduce the image features and the translational optical flow, which are explored as position and velocity cues, respectively, in Chapter 2 and 3. Consider a vehicle equipped with a camera and an IMU, with position vector $\xi \in \mathbb{R}^3$ and velocity vector $v \in \mathbb{R}^3$ both expressed in $\{\mathcal{I}\}$, such that $\dot{\xi} = v$. Let $R \in SO(3)$ denote the rotation matrix from $\{\mathcal{B}\}$ to $\{\mathcal{I}\}$ and $\dot{R} = R[\Omega]_\times$, where $\Omega \in \mathbb{R}^3$ is the angular velocity of the vehicle expressed in $\{\mathcal{B}\}$. Now we will introduce the following assumptions about the environment and the setup.

Assumption A.1. *The camera is attached to the center of mass of the vehicle so that the camera reference frame coincides with the body-fixed frame* $\{\mathcal{B}\}$.

Assumption A.2. *The angular velocity* Ω *is measured and the orientation matrix* R *of* $\{B\}$ *with respect to* $\{I\}$ *is obtained by external observer-based IMU measurements. This allows to represent all image information and the system dynamics in the inertial frame.*

Assumption A.3. *There is a flat and textured surface, which defines the target plane. The direction* $\eta \in S^2$ *expressed in* $\{\mathcal{I}\}$ *is the vector normal to the target plane and is assumed to be known.*

Assumption A.4. *There are* n $(n \geq 2)$ *visible target points lying in the target plane with position vector* $s_i \in \mathbb{R}^3, i \in \{1, \ldots, n\}$ *expressed in* $\{\mathcal{I}\}$ *such that the center* $\frac{1}{n}\sum_{i=1}^{n} s_i = 0$ *coincides with origin of the inertial frame* $\{\mathcal{I}\}$ *and* $\eta^\top s_i = 0$.

Assumption A.5. *There are at least two visible lines lying on the target plane which are parallel and along the unknown direction* $u \in S^2$ *expressed in* $\{\mathcal{I}\}$.

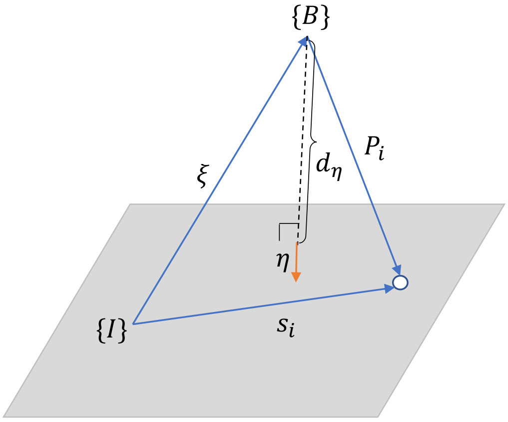

Figure A.1: Geometry of feature of point

A.1 Spherical image points

The 3D coordinates of the point i with respect to the vehicle expressed in $\{\mathcal{I}\}$ is denoted as

$$P_i = s_i - \xi. \tag{A.1}$$

The spherical image point of P_i is denoted as

$$p_i = \frac{P_i}{||P_i||} \tag{A.2}$$

which can be obtained using the sequence of 2D pixel locations (X_i, Y_i) from the camera, such that

$$p_i = R\frac{\bar{p}_i}{||\bar{p}_i||}, \qquad \bar{p}_i = \bar{A}^{-1}\begin{bmatrix} X_i \\ Y_i \\ 1 \end{bmatrix}$$

with $\bar{A}^{-1}$ the matrix of the camera's intrinsic parameters that transforms image pixel to perspective coordinates $\bar{p}_i$. The height of the vehicle above the target plane (see Fig. A.1) is denoted by $d_\eta := \eta^\top P_i = -\eta^\top \xi$.

A.2 Visual centroid vectors

In this subsection, we will define two different kinds of visual centroid vector using spherical image points, which provide relative position cue of the vehicle with respect to the target.

The first visual centroid is simply the spherical image centroid:

$$q = -\frac{1}{n}\sum_{i=1}^{n} p_i, \tag{A.3}$$

which is the simplest image feature that encodes all information about the position of the vehicle with respect to the target. Its calculation is highly robust to pixel noise, since it considers several image points. The following lemmas will clarify the relationship between the image centroid q and the position vector of the vehicle ξ.

Lemma A.1. *For $d_\eta > 0$, image feature q is a bijective function of ξ.*

Proof of Lemma A.1. From (A.1) and (A.3), it is clear that q is a function of ξ. We compute the partial derivative of q with respect to ξ and denote it by Q

$$Q := \frac{\partial q(\xi)}{\partial \xi} = \frac{1}{n}\sum_{i=1}^{n} \frac{1}{\|P_i\|}\pi_{p_i}, \tag{A.4}$$

to conclude Q is positive definite provided that at least two target points p_i and p_j, $1 \leq i \neq j \leq n$ on the target plane are non-collinear, and the distance to the ground d_η is positive. Then, for any pair of desired position and desired image centroid (ξ^*, q^*) such that $\eta^\top \xi^* < 0$ and using the generalization of the mean value theorem for vector valued functions [McL65], q can be written as

$$q = q^* + \bar{Q}(\xi - \xi^*), \tag{A.5}$$

where $\bar{Q} = \sum_{k=1}^{3} \alpha_k Q(c_k)$, for $\alpha_k \geq 0$, $\sum_{k=1}^{3} \alpha_k = 1$, and c_k belongs to the line segment between the desired position ξ^* and ξ. Since $\bar{Q} > 0$, the inverse function of A.5 can be readily obtained, showing that q is a bijective function of ξ as long as $d_\eta > 0$. ☐

Lemma A.2. *The function*

$$\mathcal{L}_1(\tilde{\xi}) = \int_{\xi^*}^{\xi} (q(x) - q^*)^\top dx = \frac{1}{n}\sum_{i=1}^{n} (\|P_i\| - \|P_i^*\|)$$

is a positive definite function of $\tilde{\xi} := \xi - \xi^*$.

Proof. We compute the first and second order partial derivatives of $\mathcal{L}_1$ with respect to $\tilde{\xi}$, obtaining

$$\frac{\partial \mathcal{L}_1}{\partial \tilde{\xi}} = (q - q^*)^\top$$
$$\frac{\partial^2 \mathcal{L}_1}{\partial \tilde{\xi}^2} = Q,$$

where Q is given in (A.4). Since Q is positive definite, provided that the distance to the ground is positive, $\mathcal{L}_1$ is a convex function of $\tilde{\xi}$, with a global minimum at $q - q^* = 0$ or equivalently at $\tilde{\xi} = 0$. To obtain an explicit expression for $\mathcal{L}_1$ in terms of $\tilde{\xi}$, we apply the mean value theorem to obtain

$$\mathcal{L}_1(\tilde{\xi}) = (q(z) - q^*)^\top \tilde{\xi},$$

where z belongs to the line segment between ξ and ξ^*. As in (A.5) and applying once again the mean value theorem, $q(z)$ can be written as

$$q(z) = q^* + \bar{Q}(z - \xi^*),$$

recalling that

$$\bar{Q} = \sum_{k=1}^{3} \alpha_k Q(c_k)$$

with $\alpha_k \geq 0$, $\sum_{k=1}^{3} \alpha_k = 1$, and c_k belongs to the line segment between ξ^* and z, for $k \in \{1,2,3\}$. Since $z = (1-a)\xi + a\xi^*$, $0 < a < 1$, we obtain

$$\mathcal{L}_1(\tilde{\xi}) = (1-a)\tilde{\xi}^\top \bar{Q}\tilde{\xi}.$$

□

The alternative visual centroid vector is defined as

$$q_\eta = -\frac{1}{n}\sum_{i}^{n} \frac{p_i}{\eta^\top p_i} \tag{A.6}$$

substituting (A.2) and (A.1) into (A.6), we have

$$q_\eta = \frac{\xi}{d_\eta}.$$

We can conclude that q_η can be represented directly as a position vector, scaled by the inverse of the distance to the target plane, which provides a simple structure for controller design and stability analysis.

Remark A.1. For both centroid vectors q and q_η, it is not necessary to match observed image points with desired features as required in classical image based visual servo control. Besides, they are easily computed in real-time in the camera frame and then derotated, which ensures that they are invariant to any orientation motion [HM02].

A.3 Image of lines

Each line (represented in Figure A.2 by a dashed line) together with the origin of the camera/body frame $\{\mathcal{B}\}$ defines a plane (the dark gray triangles) and the image of the line also belongs to that plane. The unit vector $h_i \in \mathbb{S}^2$ normal to this plane can be directly obtained from the image of the line[MH05][LBHM+14]. The image of the line can be identified using a convenient line detection technique, such as the Hough transform. In addition, if at least two lines are observed, then the direction u can be readily obtained from

$$u = \frac{h_2 \times h_1}{\|h_2 \times h_1\|}.$$

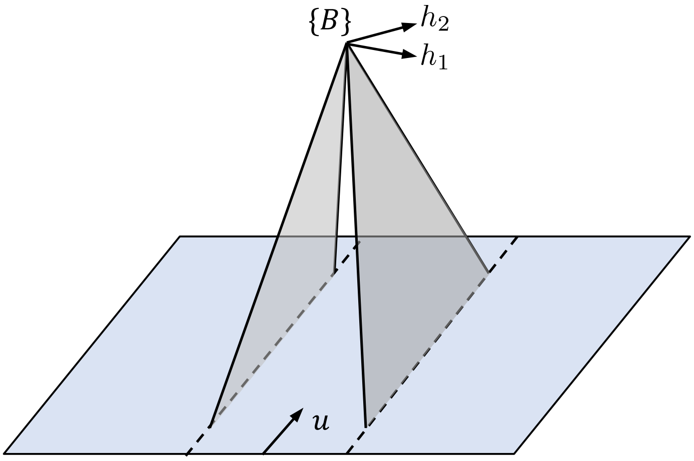

Figure A.2: Geometry of image of lines

Remark A.2. The pair (H_i, u) forms the so-called normalized Plücker coordinates, where the vector H_i is given by $H_i = \mathring{P}_i \times u$ and $\mathring{P}_i$ is any vector going from the origin of $\{\mathcal{B}\}$ to the line i. As opposed to (H_i, u), which uniquely represents a straight line with respect to a reference frame (in this case $\{\mathcal{B}\}$), the pair (h_i, u) forms the binormalized Plücker coordinates that can represent any line parallel to u and belonging to the plane normal to h_i [MH05]. Note that H_i and h_i are collinear and h_i is simply given by $h_i = \frac{H_i}{\|H_i\|}$. Although with just one pair (h_i, u), the position of the camera is not uniquely defined. If we combine visual information from the two lines (this procedure can be extended to accommodate for more than two lines), then the projection of the camera position in the plane orthogonal to u becomes uniquely defined.

A.4 Image kinematics and translational optical Flow

The kinematics of any observed points on the target plane (including the target points) can be written as:

$$\dot{P} = v$$

where P expressed in $\{\mathcal{I}\}$ denotes any point on the textured target plane. So the kinematics of the corresponding image point $p = \frac{P}{\|P\|}$, which defines optical-flow equations on the spherical surface, can be written as

$$\dot{p} = -\cos\theta_\eta \pi_p \frac{v}{d_\eta},$$

where $\cos\theta_\eta = \eta^\top p = \frac{d_\eta}{\|P\|}$.

The visual measurement including translational velocity cue is the *translational optical flow*

$$W(t) = \frac{v(t)}{d_\eta(t)},$$

which can be obtained by integrating $\dot{p}$ over a solid angle $\mathcal{S}^2$ of the sphere around the normal direction η to the target plane. It can be shown that the average of the optical flow [HHMR12]:

$$W(t) = -(R_t \Lambda^{-1} R_t^\top) \int\int_{\mathcal{S}^2} \dot{p} dp,$$

where the parameter θ_0 and the constant diagonal matrix Λ depend on the geometry of the solid angle $\mathcal{S}^2$ and R_t represents the orientation matrix of the target plane with respect to the inertial frame. Since $\{I\}$ is chosen coincident with the target frame one has $R_t = I_3$.

In practice, the optical flow is first measured in the camera frame from the 2-D optical flow obtained from a sequence of images using the Lucas-Kanade algorithm and then derotated (see [HHMR12] for more detail).

B

TECHNICAL LEMMAS AND THEOREM

Lemma B.1. *Consider a formation* $G(\boldsymbol{p}(t))$ *defined in* $\mathbb{R}^d$*, If* $\forall t$, $\operatorname{rank}(L_B(\boldsymbol{p}(t))) = dn - d - 1$*, then* $\operatorname{Null}(L_B(\boldsymbol{p}(t))) = \operatorname{span}\{U,\ p(t)\}$.

Proof. The proof of the statement $\operatorname{Null}(L_B(\boldsymbol{p}(t))) = \operatorname{span}\{U,\ \boldsymbol{p}(t)\}$ is same as stated in [ZZ16, Theorem 4] since [ZZ16, Theorem 4] is still valid for time-varying cases. ☐

Lemma B.2. *Let* $y_i \in \mathbb{S}^2$, $i = 1, \ldots, m$ *and define the matrix-valued functions*

$$A = \begin{bmatrix} 0 & -I \\ c_4 \sum\limits_{i=1}^{m} \pi_{y_i} & c_5 I \end{bmatrix} \text{ and } Q = \begin{bmatrix} c_3 \sum\limits_{i=1}^{m} \pi_{y_i} & c_2 \sum\limits_{i=1}^{m} \pi_{y_i} \\ c_2 \sum\limits_{i=1}^{m} \pi_{y_i} & m c_1 I \end{bmatrix}$$

where c_1, c_2, c_3, c_4 *and* c_5 *are positive constants, such that* $c_3 c_5 > c_4^2$*. There exists* $c > 0$ *such that* $cQ - A^\top A \geq 0$.

Proof. Define $H_i = \begin{bmatrix} \pi_{y_i} & 0 \\ 0 & I \end{bmatrix}$, $H = \sum\limits_{i=1}^{m} H_i = \begin{bmatrix} \sum\limits_{i=1}^{m} \pi_{y_i} & 0 \\ 0 & mI \end{bmatrix}$, $l_Q = \lambda_{\min}(\begin{bmatrix} c_3 & c_2 \\ c_2 & c_1 \end{bmatrix})$, and $l_A = \lambda_{\max}(\begin{bmatrix} c_4^2 & c_5 c_4 \\ c_5 c_4 & c_5^2 + 1 \end{bmatrix})$. Since $Q = \sum\limits_{i=1}^{m} H_i \begin{bmatrix} c_3 & c_2 \\ c_2 & c_1 \end{bmatrix} H_i \geq l_Q \sum\limits_{i=1}^{m} H_i^2 = l_Q \sum\limits_{i=1}^{m} H_i = l_Q H$ and $A^\top A = H \begin{bmatrix} c_4^2 & c_5 c_4 \\ c_5 c_4 & c_5^2 + 1 \end{bmatrix} H \leq l_A H^2$, we can conclude that $cQ - A^\top A \geq 0$ if $c l_Q - l_A \lambda_{\max}(H) \geq 0$, which holds if $c \geq \frac{l_A}{l_Q} m$. ☐

Lemma B.3. *Consider the matrix* A *and* Q *defined in equation* (5.18) *and equation* (5.19) *respectively. Assume* $k_d > \frac{k_p}{4} \|\bar{H}\|^2 + 1$*. There exists* $c > 0$ *such that* $cQ - A^\top A \geq 0$.

Proof. Define $S = \begin{bmatrix} \operatorname{diag}\left(\pi_{g_k}\right) \bar{H} & 0_{dm \times dn} \\ 0_{dn} & I_{dn} \end{bmatrix}$, $\Lambda_Q = \begin{bmatrix} I_{dm} & \frac{1}{2} \bar{H} \\ \frac{1}{2} \bar{H}^\top & (k_d - 1) I_{dn} \end{bmatrix}$ and $\Lambda_A = \begin{bmatrix} \bar{H} \bar{H}^\top & k_d \bar{H} \\ k_d \bar{H}^\top & (I_{dn} - \frac{U U^\top}{n})^2 + k_d^2 I_{dnd} \end{bmatrix}$, then $Q = S^\top \Lambda_Q S$ and $A^\top A = S^\top \Lambda_A S$. We can conclude that $cQ - A^\top A \geq 0$, if $c \Lambda_Q - \Lambda_A \geq 0$ which holds if c is chosen such that $(k_p k_d - k_p - \frac{k_p^2}{4} \|\bar{H}\|^2) c^2 - (k_p k_d^2 + k_p - k_p^2 \|\bar{H}\|^2) c + k_p^2 \|\bar{H}\|^2 \geq 0$ and $c \geq \max\{k_p \|\bar{H}\|^2, \frac{k_d^2 + 1}{k_d - 1}\}$.

$\square$

Theorem B.1. *Consider the following system*

$$\dot{x}(t) = f(x(t), t), \; x \in \mathbb{R}^n \tag{B.1}$$

with $f(x(t),t)$ *a piecewise continuous and locally Lipschitz function such that* $f(0,t) = 0$*. Assume there exists a function* $\mathcal{L}_x(t) = \mathcal{L}(t, x(t)) \in \mathbb{R}^+$*, such that* $\lambda_1 \|x(t)\|^2 \leq \mathcal{L}_x(t) \leq \lambda_2 \|x(t)\|^2$ *and* $\dot{\mathcal{L}}_x(t) \leq -\gamma x(t)^\top \Sigma(t) x(t)$*, where* $\Sigma(t) \in \mathbb{R}^{n \times n}$ *is an upper bounded positive semi-definite function* ($\|\Sigma(t)\| \leq \lambda_\Sigma$)*, with* λ_1*,* λ_2*,* λ_Σ *positive constants and* $\gamma(x(0))$ *a positive function of the initial state* $x(0)$*. If*
1) $\exists T > 0$*,* $\exists \mu > 0$ *such that* $\forall t > 0$*,* $\frac{1}{T} x(t)^\top \int_t^{t+T} \Sigma(\tau) d\tau x(t) \geq \mu \|x(t)\|^2$ *and,*
2) $\dot{\mathcal{L}}_x(t) \leq -\frac{1}{c} \|f(x,t)\|^2 \leq 0$*,* $c > 0$*,*
then the origin of (B.1) *is exponentially stable (ES), and verifies:* $x(t) \leq \sqrt{\frac{\lambda_2}{\lambda_1(1-\sigma)}} x(0) \exp(-\frac{\sigma}{2T} t)$ *with* $\sigma = \frac{1}{1+\rho} \frac{1}{1+\rho c T^2 \gamma \lambda_\Sigma}$ *and* $\rho = \frac{\lambda_2}{\mu T \gamma}$*.*

Proof. The proof follows the arguments used in [LP02, Lemma 5]. Taking integral of $\dot{\mathcal{L}}_x(t) \leq -\gamma x(t)^\top \Sigma(t) x(t)$, we get

$$\mathcal{L}_x(t+T) - \mathcal{L}_x(t) \leq -\gamma \int_t^{t+T} \|\Sigma^{\frac{1}{2}}(\tau) x(\tau)\|^2 d\tau \tag{B.2}$$

where, according to (B.1), $x(\tau)$ can be rewritten as

$$x(\tau) = x(t) + \int_t^\tau f(x(s), s) ds. \tag{B.3}$$

To obtain a bound for the integral term in (B.2), we substitute (B.3) in $\|\Sigma^{\frac{1}{2}}(\tau) x(\tau)\|^2$ and use $\|a+b\|^2 \geq [\rho/(1+\rho)] \|a\|^2 - \rho \|b\|^2$ and Schwartz inequality to obtain

$$\|\Sigma^{\frac{1}{2}}(\tau) x(\tau)\|^2 \geq \frac{\rho}{1+\rho} \|\Sigma^{\frac{1}{2}}(\tau) x(t)\|^2 - \rho \lambda_\Sigma T \int_t^\tau \|f(x(s), s)\|^2 ds. \tag{B.4}$$

Substituting (B.4) into (B.2), we obtain

$$\begin{aligned} \mathcal{L}_x(t+T) - \mathcal{L}_x(t) &\leq -\frac{\gamma \rho}{1+\rho} \int_t^{t+T} \|\Sigma^{\frac{1}{2}}(\tau) x(t)\|^2 d\tau \\ &+ \rho \gamma \lambda_\Sigma T \int_t^{t+T} \int_t^\tau \|f(x(s), s)\|^2 ds d\tau. \end{aligned}$$

Using the condition (1) and (2), we have

$$\mathcal{L}_x(t+T) - \mathcal{L}_x(t) \leq -\frac{\mu T \gamma \rho}{1+\rho} \|x(t)\|^2 - c \rho \gamma \lambda_\Sigma T \int_t^{t+T} \int_t^\tau \dot{\mathcal{L}}(s) ds d\tau. \tag{B.5}$$

Changing the order of integration in equation (B.5), one can get

$$-\int_t^{t+T} \int_t^\tau \dot{\mathcal{L}}_x(s) ds d\tau \leq -T \int_t^{t+T} \dot{\mathcal{L}}_x(s) ds = T(\mathcal{L}_x(t) - \mathcal{L}_x(t+T)) \tag{B.6}$$

Substituting inequality (B.6) into (B.5) we have

$$\mathcal{L}_x(t+T) \leq (1-\sigma) \mathcal{L}_x(t), \; \sigma := \frac{\rho \mu T \gamma}{(1+\rho)(1+\rho c T^2 \gamma \lambda_\Sigma) \lambda_2}.$$

By choosing $\rho = \frac{\lambda_2}{\mu T \gamma}$, one has $\sigma = \frac{1}{1+\rho}\frac{1}{1+\rho c T^2 \gamma \lambda_\Sigma} < 1$. For any $t \geq 0$, let N be the smallest positive integer such that $t \leq NT$. Since $\mathcal{L}_x(t) \leq \mathcal{L}_x((N-1)T) \leq (1-\sigma)\mathcal{L}_x((N-2)T)$, $\mathcal{L}_x(t)$ can be bounded by a staircase geometric series such that $\mathcal{L}_x(t) \leq (1-\sigma)^{N-1} L_x(0)$ and hence the exponential convergence follows from $\mathcal{L}_x(t) \leq (1-\sigma)^{N-1}\mathcal{L}_x(0) = \frac{\exp(-bNT)}{1-\sigma}\mathcal{L}_x(0) \leq \frac{\exp(-bt)}{1-\sigma}\mathcal{L}_x(0)$ with $b = \frac{1}{T}\ln(\frac{1}{1-\sigma}) > \frac{\sigma}{T}$. $\square$

BIBLIOGRAPHY

[ADY07] B. Anderson, S. Dasgupta, and C. Yu. Control of directed formations with a leader-first follower structure. In *2007 46th IEEE Conference on Decision and Control*, pages 2882–2887, 2007.

[AYFH08] B. Anderson, C. Yu, B. Fidan, and J. M Hendrickx. Rigid graph control architectures for autonomous formations. *IEEE Control Systems Magazine*, 28(6):48–63, 2008.

[BBJ10] M. Basiri, A. Bishop, and P. Jensfelt. Distributed control of triangular formations with angle-only constraints. *Systems & Control Letters*, 59(2):147–154, 2010.

[BFOO08] Francisco Bonin-Font, Alberto Ortiz, and Gabriel Oliver. Visual navigation for mobile robots: A survey. *Journal of intelligent and robotic systems*, 53(3):263, 2008.

[BGC16] Suman Raj Bista, Paolo Robuffo Giordano, and François Chaumette. Appearance-based indoor navigation by ibvs using line segments. *IEEE Robotics and Automation Letters*, 1(1):423–430, 2016.

[BGH$^+$11] Sylvain Bertrand, Nicolas Guénard, Tarek Hamel, Hélene Piet-Lahanier, and Laurent Eck. A hierarchical controller for miniature {VTOL} uavs: Design and stability analysis using singular perturbation theory. *Control Engineering Practice*, 19(10):1099 – 1108, 2011.

[BGMB07] D. Blake Barber, Stephen R. Griffiths, Timothy W. McLain, and Randal W. Beard. Autonomous landing of miniature aerial vehicles. *Journal of Aerospace Computing, Information, and Communication*, 4(5):770–784, 2017/03/07 2007.

[Bis11] A. Bishop. A very relaxed control law for bearing-only triangular formation control. *IFAC Proceedings Volumes*, 44(1):5991–5998, 2011.

[Boi98] JL Boiffier. The flight dynamics: The equations, 1998.

[BR78] Andrew Burton and John Radford. *Thinking in perspective: critical essays in the study of thought processes*, volume 646. Routledge, 1978.

[Car03] James V. Carroll. Vulnerability assessment of the u.s. transportation infrastructure that relies on the global positioning system. *Journal of Navigation*, 56(2):185–193, 005 2003.

[CHC16] François Chaumette, Seth Hutchinson, and Peter Corke. Visual servoing. In *Springer Handbook of Robotics*, pages 841–866. Springer, 2016.

[DK02] Guilherme N DeSouza and Avinash C Kak. Vision for mobile robot navigation: A survey. *IEEE transactions on pattern analysis and machine intelligence*, 24(2):237–267, 2002.

[Ere07] T. Eren. Using angle of arrival (bearing) information for localization in robot networks. *Turkish Journal of Electrical Engineering & Computer Sciences*, 15(2):169–186, 2007.

[Ere12] T. Eren. Formation shape control based on bearing rigidity. *International Journal of Control*, 85(9):1361–1379, 2012.

[EWM+03] T. Eren, W. Whiteley, S. Morse, P. Belhumeur, and B. Anderson. Sensor and network topologies of formations with direction, bearing, and angle information between agents. In *42nd IEEE International Conference on Decision and Control*, volume 3, pages 3064–3069, 2003.

[FGH03] DC Foyle, A Goodman, and BL Hooey. Nasa aviation safety program conference on human performance modeling of approach and landing with augmented displays. *National Aeronautics and Space Administration*, 2003.

[FMFS17] Davide Falanga, Elias Mueggler, Matthias Faessler, and Davide Scaramuzza. Aggressive quadrotor flight through narrow gaps with onboard sensing and computing using active vision. In *2017 IEEE international conference on robotics and automation (ICRA)*, pages 5774–5781. IEEE, 2017.

[FW15] Dario Floreano and Robert J Wood. Science, technology and the future of small autonomous drones. *Nature*, 521(7553):460, 2015.

[GAR10] Tiago Gonçalves, José Azinheira, and Patrick Rives. Homography-based visual servoing of an aircraft for automatic approach and landing. In *Robotics and Automation (ICRA), 2010 IEEE International Conference on*, pages 9–14. IEEE, 2010.

[GBC+15] Victor Gibert, Laurent Burlion, Abdelhamid Chriette, Josep Boada, and Franck Plestan. New pose estimation scheme in perspective vision system during civil aircraft landing. *IFAC-PapersOnLine*, 48(19):238–243, 2015.

[GL20] Dejun Guo and Kam K Leang. Image-based estimation, planning, and control for high-speed flying through multiple openings. *The International Journal of Robotics Research*, page 0278364920921943, 2020.

[HDWRDC18] HW Ho, C De Wagter, BDW Remes, and GCHE De Croon. Optical-flow based self-supervised learning of obstacle appearance applied to mav landing. *Robotics and Autonomous Systems*, 100:78–94, 2018.

[HHC96] S. Hutchinson, G.D. Hager, and P.I. Corke. A tutorial on visual servo control. *Robotics and Automation, IEEE Transactions on*, 12(5):651–670, Oct 1996.

[HHMR12] B. Hérissé, T. Hamel, R. Mahony, and F.-X. Russotto. Landing a vtol unmanned aerial vehicle on a moving platform using optical flow. *IEEE Transactions on Robotics*, 28(1):77–89, feb. 2012.

[HM02] T. Hamel and R. Mahony. Visual servoing of an under-actuated dynamic rigid-body system: an image-based approach. *IEEE Transactions on Robotics and Automation*, 18(2):187–198, Apr 2002.

[HMLO02] Tarek Hamel, Robert Mahony, Rogelio Lozano, and James Ostrowski. Dynamic modelling and configuration stabilization for an x4-flyer. *IFAC Proceedings Volumes*, 35(1):217–222, 2002.

[HS17] T. Hamel and C. Samson. Position estimation from direction or range measurements. *Automatica*, 82:137–144, 2017.

[KGD10] M. K. Kaiser, N.R. Gans, and W.E. Dixon. Vision-based estimation for guidance, navigation, and control of an aerial vehicle. *IEEE Transactions on Aerospace and Electronic Systems*, 46(3):1064–1077, 2010.

[Kha92] Hassan K. Khalil. *Nonlinear Systems*. MacMillan Publishing Company, New York, USA, 1992.

[KKL+13] H. J. Kim, M. Kim, H. Lim, C. Park, S. Yoon, D. Lee, H. Choi, G. Oh, J. Park, and Y. Kim. Fully autonomous vision-based net-recovery landing system for a fixed-wing uav. *IEEE/ASME Transactions on Mechatronics*, 18(4):1320–1333, Aug 2013.

[LBHM+14] Florent Le Bras, Tarek Hamel, Robert Mahony, Christian Barat, and Julien Thadasack. Approach maneuvers for autonomous landing using visual servo control. *IEEE Transactions on Aerospace and Electronic Systems*, 50(2):1051–1065, 2014.

[LBHMS17] F. Le Bras, T. Hamel, R. Mahony, and C. Samson. Observers for position estimation using bearing and biased velocity information. In *Sensing and Control for Autonomous Vehicles*, pages 3–23. Springer, 2017.

[LBMK17] Giuseppe Loianno, Chris Brunner, Gary McGrath, and Vijay Kumar. Estimation, control, and planning for aggressive flight with a small quadrotor with a single camera and imu. *IEEE Robotics and Automation Letters*, 2(2):404–411, 2017.

[LH02] Greg Loegering and Steve Harris. Landing dispersion results - global hawk auto-land system. In *AIAA 1st Technical Conference and Workshop on Unmanned Aerospace Vehicles*. American Institute of Aeronautics and Astronautics, 2002.

[LKSM13] M. Laiacker, K. Kondak, M. Schwarzbach, and T. Muskardin. Vision aided automatic landing system for fixed wing uav. In *2013 IEEE/RSJ International Conference on Intelligent Robots and Systems*, pages 2971–2976, Nov 2013.

[LP02] A. Lorıa and E. Panteley. Uniform exponential stability of linear time-varying systems: revisited. *Systems & Control Letters*, 47(1):13–24, 2002.

[MCH08] R. Mahony, P. Corke, and T. Hamel. Dynamic image-based visual servo control using centroid and optic flow features. *Journal of Dynamic Systems, Measurement, and Control*, 130(1):011005, 2008.

[McL65] Robert M McLeod. Mean value theorems for vector valued functions. *Proceedings of the Edinburgh Mathematical Society (Series 2)*, 14(03):197–209, 1965.

[ME10] Mehran Mesbahi and Magnus Egerstedt. *Graph theoretic methods in multiagent networks*, volume 33. Princeton University Press, 2010.

[MH05] R. Mahony and T. Hamel. Image-based visual servo control of aerial robotic systems using linear image features. *IEEE Transactions on Robotics*, 21(2):227–239, April 2005.

[MSM+12] Nathan Michael, Shaojie Shen, Kartik Mohta, Yash Mulgaonkar, Vijay Kumar, Keiji Nagatani, Yoshito Okada, Seiga Kiribayashi, Kazuki Otake, Kazuya Yoshida, et al. Collaborative mapping of an earthquake-damaged building via ground and aerial robots. *Journal of Field Robotics*, 29(5):832–841, 2012.

[OPA15] K. Oh, M. Park, and H. Ahn. A survey of multi-agent formation control. *Automatica*, 53:424–440, 2015.

[PH88] David A Peters and Ninh HaQuang. Dynamic inflow for practical applications. 1988.

[RA07] W. Ren and E. Atkins. Distributed multi-vehicle coordinated control via local information exchange. *International Journal of Robust and Nonlinear Control: IFAC-Affiliated Journal*, 17(10-11):1002–1033, 2007.

[RBM05] W. Ren, R. Beard, and T. McLain. Coordination variables and consensus building in multiple vehicle systems. In *Cooperative control*, pages 171–188. Springer, 2005.

[RHMS14] Lorenzo Rosa, Tarek Hamel, Robert Mahony, and Claude Samson. Optical-flow based strategies for landing vtol uavs in cluttered environments. *IFAC Proceedings Volumes*, 47(3):3176–3183, 2014.

[SCH+15] P. Serra, R. Cunha, T. Hamel, C. Silvestre, and F. Le Bras. Nonlinear image-based visual servo controller for the flare maneuver of fixed-wing aircraft using optical flow. *Control Systems Technology, IEEE Transactions on*, 23(2):570–583, March 2015.

[SCH+16] Pedro Serra, Rita Cunha, Tarek Hamel, David Cabecinhas, and Carlos Silvestre. Landing of a quadrotor on a moving target using dynamic image-based visual servo control. *IEEE Transactions on Robotics*, 32(6):1524–1535, 2016.

[SFZG16] F. Schiano, A. Franchi, D. Zelazo, and P. Giordano. A rigidity-based decentralized bearing formation controller for groups of quadrotor uavs. In *2016 IEEE/RSJ International Conference on Intelligent Robots and Systems (IROS)*, pages 5099–5106, 2016.

[SL03] Brian L. Stevens and Frank L. Lewis. *Aircraft Control and Simulation*. John Wiley & Sons, Inc., 2003.

[SW99] B. Servatius and W. Whiteley. Constraining plane configurations in computer-aided design: Combinatorics of directions and lengths. *SIAM Journal on Discrete Mathematics*, 12(1):136–153, 1999.

[TCC+20] Z. Tang, R. Cunha, D. Cabecinhas, T. Hamel, and C. Silvestre. Quadrotor going through a window and landing: An image-based visual servo control approach. *Control Engineering Practice*, Provisionally accepted, 2020.

[TCHS18a] Z. Tang, R. Cunha, T. Hamel, and C. Silvestre. Aircraft landing using dynamic two-dimensional image-based guidance control. *IEEE Transactions on Aerospace and Electronic Systems*, 55(5):2104–2117, 2018.

[TCHS18b] Z. Tang, R. Cunha, T. Hamel, and C. Silvestre. Going through a window and landing a quadrotor using optical flow. In *2018 European Control Conference (ECC)*, pages 2917–2922. IEEE, 2018.

[TCHS20a] Z. Tang, R. Cunha, T. Hamel, and C. Silvestre. Bearing leader-follower formation control under persistence of excitation. In *2020 IFAC World congress*, 2020.

[TCHS20b] Z. Tang, R. Cunha, T. Hamel, and C. Silvestre. Bearing-only formation control under persistence of excitation. In *2020 59th IEEE Conference on Decision and Control (CDC)*, pages 4011–4016. IEEE, 2020.

[TCHS20c] Z. Tang, R. Cunha, T. Hamel, and C. Silvestre. Formation control of a leader-follower structure in three dimensional space using bearing measurements. *Automatica*, Accepted, 2020.

[TCHS21] Z. Tang, R. Cunha, T. Hamel, and C. Silvestre. Relaxed bearing rigidity and bearing formation control under persistence of excitation. *Automatica*, Submitted, 2021.

[TLS+15] Zhiqi Tang, Linqian Li, Pedro Serra, David Cabecinhas, Tarek Hamel, Rita Cunha, and Carlos Silvestre. Homing on a moving dock for a quadrotor vehicle. In *TENCON 2015-2015 IEEE Region 10 Conference*, pages 1–6. IEEE, 2015.

[TMS+14] Saul Thurrowgood, Richard J. D. Moore, Dean Soccol, Michael Knight, and Mandyam V. Srinivasan. A biologically inspired, vision-based guidance system for automatic landing of a fixed-wing aircraft. *Journal of Field Robotics*, 31(4):699–727, 2014.

[TVTA19] Minh Hoang Trinh, Quoc Van Tran, and Hyo-Sung Ahn. Minimal and redundant bearing rigidity: Conditions and applications. *IEEE Transactions on Automatic Control*, 2019.

[TW85] Tiong-Seng Tay and Walter Whiteley. Generating isostatic frameworks. *Structural Topology 1985 Núm 11*, 1985.

[TZS+19] M. Trinh, S. Zhao, Z. Sun, D. Zelazo, B. Anderson, and H. Ahn. Bearing-based formation control of a group of agents with leader-first follower structure. *IEEE Transactions on Automatic Control*, 64(2):598–613, 2019.

[VG13] Gibert Victor and Puyou Guilhem. Landing of an airliner using image based visual servoing. *IFAC Proceedings Volumes*, 46(23):74–79, 2013.

[VIC14] VICON. Motion capture systems from vicon. `http://www.vicon.com`, 2014.

[ZLD19] Shiyu Zhao, Zhenhong Li, and Zhengtao Ding. Bearing-only formation tracking control of multi-agent systems. *IEEE Transactions on Automatic Control*, 2019.

[ZZ15a] S. Zhao and D. Zelazo. Bearing-based formation stabilization with directed interaction topologies. In *54th IEEE Conference on Decision and Control (CDC)*, pages 6115–6120, 2015.

[ZZ15b] Shiyu Zhao and Daniel Zelazo. Translational and scaling formation maneuver control via a bearing-based approach. *IEEE Transactions on Control of Network Systems*, 4(3):429–438, 2015.

[ZZ16] S. Zhao and D. Zelazo. Bearing rigidity and almost global bearing-only formation stabilization. *IEEE Transactions on Automatic Control*, 61(5):1255–1268, 2016.